

ABSTRACT

Title of Dissertation:

THE SEDIMENT AND CRUSTAL
STRUCTURE OF THE SOUTHEASTERN
UNITED STATES

Erin Cunningham, Doctor of Philosophy, 2019

Dissertation Directed By:

Professor Vedran Lekić, Department of Geology

The Southeastern United States (SEUS) preserves a detailed geologic record of the continental collision and rifting that has shaped it over billions of years. Currently the SEUS lies on a passive margin far away from ongoing tectonics, yet retains the ability to produce damaging earthquakes. It has long been suspected that the current seismicity in the SEUS is related to zones of weakness inherited from past structural boundaries; however, the mechanisms that dictate the size and location remain poorly understood and the ground shaking hazard posed by widespread sedimentary basins remains poorly quantified. P-to-S converted waves, analyzed through the receiver function technique, enable detailed imaging of lithospheric structure, but suffer from contamination in sedimented regions. Therefore, I implement a method for constraining average crustal thickness and seismic velocities while correcting for the effects of sediments. I then use high-frequency constraints on sediment structure to construct a reference velocity model for the Atlantic Coastal Plain, discussing its implications for seismic hazard. Finally, using S_p and sediment-corrected P_s receiver functions, I image the structure of the crust and mantle lithosphere across the SEUS, applying identifying dipping crustal structures that appear to be associated with active seismic zones. I discuss these structures in the context of the region's tectonic past and future seismic hazards

THE SEDIMENT AND CRUSTAL STRUCTURE OF THE SOUTHEASTERN
UNITED STATES

by

Erin Cunningham

Dissertation submitted to the Faculty of the Graduate School of the
University of Maryland, College Park, in partial fulfillment
of the requirements for the degree of
Doctor of Philosophy
2019

Advisory Committee:
Professor Vedran Lekić, Chair
Dr. Nicholas Schmerr
Dr. Mong Han Huang
Dr. Lara Wagner
Dr. Brian Phillips

© Copyright by
Erin Cunningham
2019

Table of Contents

Table of Contents	ii
List of Tables	iv
List of Figures	v
Chapter 1: Introduction to the Lithosphere and the Southeastern United States	1
1.1 Overview of Chapter 2	3
1.2 Overview of Chapter 3	4
1.3 Overview of Chapter 4	5
1.4 Technical Background: Receiver Function Methodology	6
1.4.1 Phase picking and P-SV-SH rotation	12
1.4.2 Deconvolution	14
1.4.3 Frequency Domain Deconvolution	16
1.4.4 Time Domain Deconvolution	19
Chapter 2: Constraining Crustal Structure in the presence of Sediment: A Multiple Converted Wave Approach	21
2.1 Introduction and Rationale for New Methodology	21
2.2 SRTC H- κ - V_p Stacking	24
2.2.1 Ps receiver functions in traditional H- κ - V_p stacks	25
2.2.2 SRTC Ps receiver function H- κ - V_p stacks	28
2.2.3 Determining when to correct for sedimentary layers	35
2.2.4 Sp receiver functions in H- κ - V_p stacks	36
2.2.5 SsPmp receiver functions in H- κ - V_p stacks	39
2.2.6 Calculating combined SRTC H- κ - V_p stacks with error	41
2.3 Receiver Function Data for H- κ - V_p Stacks	43
2.4 Results and Observations from the SRTC H- κ - V_p Method	46
2.4.1 SRTC H- κ - V_p stacking with synthetic waveforms	48
2.4.2 TA station B30A: eastern Williston Basin	51
2.4.3 TA station U60A: Atlantic Coastal Plain	55
2.4.4 TA station 448A: Mississippi Embayment	59
2.5 Discussion of H- κ - V_p Methodology	62
2.6 H- κ - V_p Conclusions	67
Chapter 3: Constraining Basin Fundamental Frequency and Velocity Profiles of the Atlantic Coastal Plain using Receiver Functions	70
3.1 Introduction to Hazard in the Atlantic Coastal Plain	70
3.2 Receiver Function Data for the ACP	75
3.3 Basin Fundamental Frequency	76
3.4 Basin Velocity Profiles	81
3.4.1 ACP Basin V_s Profile	81
3.4.2 ACP Basin V_p Profile	86
3.5 Validation	92
3.6 Discussion of ACP results	98
3.7 Conclusions	101

Chapter 4: Crustal and Lithospheric Structure in the Southeastern US using Receiver Function Common Conversion Point (CCP) Stacking	102
4.1 <i>Introduction</i>	102
4.2 <i>A Brief History of SEUS Tectonics</i>	6
4.3 <i>Receiver Function Data for Common Conversion Point (CCP) Stacking</i>	105
4.4 <i>Common Conversion Point (CCP) stacking</i>	107
4.4.1 <i>CCP stacking overview</i>	107
4.4.2 <i>Regional Velocity Model with SRTC H- κ-V_p Stacking</i>	111
4.4.3 <i>Sediment Removed PRF CCP stacks and SRF CCP stacks</i>	115
4.5 <i>Results and Observations</i>	118
4.5.1 <i>Crustal Thickness</i>	119
4.5.2 <i>Relationship between Structure and Seismicity</i>	128
4.6 <i>Discussion</i>	134
4.6.1 <i>The Extent of the Grenville Front in the SEUS</i>	134
4.6.2 <i>Evidence of the Suwanee Suture</i>	136
4.6.3 <i>Westward dipping “double Moho”</i>	137
4.6.4 <i>Correlation of Structure to SEUS Seismicity</i>	139
4.6.5 <i>On the lack of a lithosphere asthenosphere boundary or intra-lithospheric layering</i>	140
4.7 <i>Conclusions</i>	141
Summary	143
Appendices	148
Appendix A: Table A.1	148
Appendix B: CCP Figures for Chapter 4	150
Bibliography	163

List of Tables

<i>Table 2.1</i> -Number of events and slowness range for each seismic station used in this study.	40
--	----

List of Figures

Figure 1.1 - Ideally the displacement recorded at a seismogram ($u(t)$) is the convolution of the source function ($s(t)$) and the earth response ($g(t)$). (Figure modified from Shearer, 2009) 10

Figure 1.2 - Cartoon of converted P-wave energy across a Moho over mantle half space if no tilted axes of anisotropy are present. (Left) converted paths from a direct P wave at the Moho (P phases in red and S phases in dotted blue) and (right) their relative arrival times in a Ps receiver function. 12

Figure 1.3- Cartoon of converted S-wave energy across a MLD over mantle half space if no tilted axes of anisotropy are present Left - converted paths from a direct S wave at the MLD (P phases in red and S phases in dotted blue) and Right - relative arrival times in a Sp receiver function. 1

2

Figure 1.4– Ps RF for station 127A located in Hobbs, New Mexico. The y-axis shows the fraction of the amplitude of direct P arriving phase, the x-axis is in time. 17

Figure 1.5- Fourier transform from time to frequency domain for common functions. Arrows indicate the Fourier transform was taken. Top - delta function in the time domain yields a flat spanning all frequencies in the frequency domain. Bottom - boxcar function in the time domain yields a sinc function with multiple frequencies (spectral leakage) in frequency domain. 19

Figure 1.6– Time (ITDD in red) and Frequency (IFDD in blue) domain RF comparison for station 127A located in Hobbs, New Mexico. IFDD RF was filtered at 0.03-1 Hz and appears overall smoother than the ITDD RF. However, it is difficult to determine if the Ps arrival associated with the Moho occurs at 3.5 or 6 s. The ITDD RF was created with 300 iterations and appears to have more arriving phases, however, the spectral leakage has been reduced and the peaks narrow. The RF amplitudes for both frequency and time domain RFs have been normalized to 1. 20

Figure 2.1- A. Ray-path geometry and **B.** synthetic receiver functions of P-to-s phases converted across the Moho at 30 km depth, from an incident plane wave of horizontal slowness 0.06 s/km. Crustal $V_P = 6.3$ km/s, $V_S = 3.7$ km/s, while mantle $V_P = 8$ km/s and $V_S = 4.6$ km/s. Arrival times of the direct Moho P-to-s conversion and first-order multiples are relative to the arrival time of the direct Pwave. 27

Figure 2.2- A. Ray-path geometry of P-to-s phases converted across the base of a 0.5 km thick sediment layer, along with the largest-amplitude first- and second-order multiples for an incident plane wave of horizontal slowness 0.0789 s/km. **B.** Synthetic receiver functions computed for a model with a 0.5 km thick sediment layer and horizontal slowness 0.06 s/km ($V_P = 2.5$ km/s, $V_S = 1$ km/s), crustal $V_P = 6.2$ km/s, $V_S = 3.5$ km/s, a Moho at 35 km depth, and mantle $V_P = 8$

km/s, $V_S = 4.6$ km/s. Direct conversions are in black, while the oscillatory pattern is attributed to sediment multiples, labeled in red, blue and purple. Orange dots indicate where the expected arrival of phases with more than 2 P-wave legs would arrive. 29

Figure 2.3- Absolute value of the reflection coefficients of PP*PP (left) and SS*SS (right) for a range of different sediment velocity variables using equations from Aki and Richards (1980) Because each reverberation will need to be multiplied by an PPPP or SSSS reflection coefficient, the reverberations will get smaller, but the PPPP reverberation will get smaller faster, and SS*SS reverberations will remain visible in the Ps receiver function (See **Figure 2.2**) 29

Figure 2.4- The SRTC H-k-VP stacking method may not work when the PP_{bs} and P_{ms} phase arrival intersect. (Left) Calculated PP_{bs} arrival time from sediment with varying thickness and V_S . The V_P/V_S ratio changes according to the mud line equation in Brocher (2005). (Right) the $P_{ms} - PP_{bs}$ arrival time for a crust with $V_P = 6$ km/s and $V_P/V_S = 1.76$. Area where the PP_{bs} arrival may interfere with the P_{ms} Moho arrival is shown in light blue to red. SRTC stacking may not work for an extremely thin crust of 20 km, if sediment thickness is greater than 1.5 km with excessively low V_S of 0.5 km/s. 30

Figure 2.5- **A.** The autocorrelation of the mean synthetic receiver function (gray) and the best fit decaying sinusoid (red) used for determining the parameters of the resonance removal filter. The first large amplitude negative peak corresponds to the two-way s travel time in sediment (Δt) on the x-axis and the amplitude of the sediment reverberations (r_0) on the y-axis. **B.** Mean synthetic Ps receiver functions before (gray) and after (red) the resonance removal filter is applied; the filter successfully removes the reverberations and the direct P to s conversion across the Moho becomes clear. 32

Figure 2.6- Dependence of resonance removal filter on ray parameter for an idealized synthetic case. The best-fit reverberation removal filter (red line) calculated from the autocorrelation of the mean synthetic receiver function provides a good fit to the autocorrelations of Ps RFs computed across the range of possible ray parameters (black lines). The synthetic model used has a sediment layer 0.5 km thick with a $V_P = 2.5$ km/s and a $V_S = 1.7$ km/s overlying a 39.5 km crust with $V_P = 6.2$ km/s and $V_S = 3.5$ km/s and mantle with $V_P = 8$ km/s and $V_S = 4.5$ km/s. 32

Figure 2.7- **A.** Ray-path geometry of S to p converted phases across the Moho at 30 km depth calculated for an incident plane wave of 0.14 s/km and the post critical P wave reflection across the 30 km deep Moho (SP_{mp}) with incident plane wave of 0.1486 s/km. The Ps conversions from the Moho are plotted for comparison (gray line). **B.** Synthetic receiver function of the S-to-p phases converted across the Moho. Time is relative to the direct S arrival (positive values indicate earlier arrivals). **C.** Synthetic receiver function of the Hilbert-transformed post-critical P phase at the Moho. Time is relative to the direct S arrival (positive values indicate later arrivals). Crustal $V_P = 6.3$ km/s, $V_S = 3.7$ km/s, while mantle $V_P = 8$ km/s and $V_S = 4.6$ km/s. 37

Figure 2.8– SRTC H- κ -VP stacking of synthetic receiver functions, where negative values in the stack are clipped. Input model has a 0.5 km thick sedimentary layer, VP of 2 km/s, and $\kappa = 2.3$, and a Moho at 37 km depth with crustal VP = 6.3, and $\kappa = 1.76$. **A.** The mean Ps receiver function before (black) and after (red) the sediment removal filter is applied. **B.** Ps H- κ stack at assumed VP = 6.3 shows no clear maxima. **C.** The Ps H-k stack after the sediment removal filter and time correction is applied shows a clear maximum. **D, E, & F.** Three cross-sections through the maximum of the H- κ -VP triple stack; black cross hairs denote 1σ error bars. 42

Figure 2.9– H- κ -VP stacks generated from synthetic waveforms with increasing noise levels. The input model has a sedimentary layer 0.5 km thick, VP of 2.3 km/s and $\kappa = 2.3$, a Moho at 42.5 km depth with crustal VP = 6.3 km/s, and a κ of 1.76. White noise is filtered to have similar frequency content as typically encountered noise, with amplitude up to three-quarters of the maximum of the daughter waveform (s for Ps; p for Sp and SPmp). At increased noise levels, we are still able to constrain crustal H, κ , and VP within error. 51

Figure 2.10– (Top) Mean 4 Hz (blue) and 1Hz (black) Ps RF for station B30A shown with picked arrival time for δt_P and δt shown in the red and magenta circles respectively. The arrival time of the two phases (P_{bs} and PP_{bs}) likely overlap at this station. (Bottom) Autocorrelation from the mean 4Hz (blue) and 1Hz (black) RF with picked arrival time for Δt . Autocorrelation of a random subset of individual RFs are shown as gray lines in the background. 52

Figure 2.11– SRTC H- κ -VP stacking of B30A receiver functions, where negative values in the stack are clipped. Station B30A is located on the eastern edge of the Williston Basin in Montana. **A.** The mean Ps receiver function before (black) and after (red) the sediment removal filter is applied. **B.** Ps H- κ stack at assumed VP = 6.3 km/s shows a maximum of the stack at H = 28.5 km and $\kappa = 1.62$. **C.** The Ps H-k stack after the sediment removal filter and time correction is applied; the stack maximum now corresponds to larger H and κ values **D, E, & F** Three cross-sections through the maximum of the H- κ -VP triple stack; black cross-hairs denote 1σ error bars. 54

Figure 2.12 - 1Hz Ps receiver functions before (black) and after (red) sediment removal filter is applied plotted from 0 to 20 seconds after the direct P arrival. (Top) station B30A (Middle) station U60A (Bottom) station 448A 54

Figure 2.13– (Top) Mean 4 Hz (blue) and 1Hz (black) Ps RF for station U60A shown with picked arrival time for δt_P and δt shown in the red and magenta circles respectively. The arrival time of the two phases (P_{bs} and PP_{bs}) likely overlap at this station. (Bottom) Autocorrelation from the mean 4Hz (blue) and 1Hz (black) RF with picked arrival time for Δt . Autocorrelation of a random subset of individual RFs are shown as gray lines in the background. At station B30A, the arrival time of Δt does not depend on event location and only changes slightly with frequency of autocorrelated RFs. 57

Figure 2.14– SRTC H- κ -VP stacking of U60A receiver functions, where negative values in the stack are clipped. Station U60A is located on the Atlantic Coastal

Plain in North Carolina. **A.** The mean Ps receiver function before (black) and after (red) the sediment removal filter is applied. **B.** Ps H- κ stack at assumed VP = 6.3 km/s shows no clear maxima. **C.** The Ps H-k stack after the sediment removal filter and time correction is applied has a clear maximum. **D, E, & F.** Three cross-sections through the maximum of the H- κ -VP triple stack; black cross-hairs denote 1 σ error bars. 58

Figure 2.15– (Top) Mean 4 Hz (blue) and 1Hz (black) Ps RF for station 448A shown with picked arrival time for δt_P and δt shown in the red and magenta circles respectively. The arrival time of the two phases (P_{bs} and PP_{bs}) likely overlap at this station. (Bottom) Autocorrelation from the mean 4Hz (blue) and 1Hz (black) RF with picked arrival time for Δt . Autocorrelation of a random subset of individual RFs are shown as gray lines in the background. At station 448A, the arrival time of Δt is challenging to pick, likely due to the multiple sediment layers (multiple negative bumps seen in the 4Hz autocorrelation). 60

Figure 2.16– SRTC H- κ -VP stacking of 448A receiver functions. Station 448A is located on the Mississippi Embayment in Mississippi. **A.** The mean Ps receiver function before (gray) and after (red) the sediment removal filter is applied, which do not appear significantly different at this station. **B.** Ps H- κ stack at assumed VP = 6.3, and the maximum of the stack is H = 24 km and κ = 1.5. **C.** The Ps H-k stack after the sediment removal filter and time correction is applied has a maximum at H = 36.25 km and κ = 1.83. **D, E, & F.** Three cross-sections through the H- κ -VP triple stack through the maximum of the stack; black cross-hairs denote 1 σ error bars. 61

Figure 2.17– SP_{mp} RFs for events between 30 and 50 epicentral distances. Each line is a bin of backazimuthal (BAZ) directions from station ANMO, chosen due to its large range in BAZ of SP_{mp} events. The amplitude and location of the SP_{mp} at ~6 s does not change significantly based on BAZ direction which indicates that the SP_{mp} waveforms show evidence of neither crustal anisotropy nor crustal thickness variations with BAZ. We expect this observation to hold true for most other stations, due to the low frequency of SP_{mp} waveforms. 65

Figure 3.1– Basin thickness for stations on the Atlantic Coastal Plain (*Fenneman and Johnson 1946*) inferred from basement depth interpolated from *AAPG Basement Map of North America, 1978* 75

Figure 3.2- **A.** Ray-path geometry of P-to-s phases converted across the base of a 0.5 km thick sediment layer, along with the largest-amplitude first- and second-order multiples for an incident plane wave of horizontal slowness 0.0789 s/km. **B.** Synthetic receiver functions computed for a model with a 0.5 km thick sediment layer and horizontal slowness 0.06 s/km (VP = 2.5 km/s, VS = 1 km/s), crustal VP = 6.2 km/s, VS = 3.5 km/s, a Moho at 35 km depth, and mantle VP = 8 km/s, VS = 4.6 km/s. Direct conversions are in black, while the oscillatory pattern is attributed to sediment multiples, labeled in red, blue and purple. Orange dots indicate where the expected arrival of phase with more than 2 P-wave legs would arrive. 78

Figure 3.3- TSs and r_0 measurements from 4 Hz Ps receiver function autocorrelations. With increasing sediment thickness, TSs increases. **A.** Autocorrelation of Synthetic RF calculated for velocity model described in top right corner. TSs and r_0 are picked as the first negative large amplitude, shown by the red dot. **B.** Autocorrelation of 4 Hz Ps RFs for station U60A located on 0.137 km of basin material. Mean autocorrelation shown in blue and a range of Ps RF autocorrelation events shown in gray. TSs and r_0 pick shown as red dot. **C.** Autocorrelation of 4 Hz Ps RFs for station Q60A located on 1.07 km of basin material. Mean autocorrelation shown in blue and a range of Ps RF autocorrelation events shown in gray. TSs and r_0 pick shown as red dot. 78

Figure 3.4- - Measurements from the 4Hz Auto-correlated RFs across the ACP. **A.** Measurements of TSs at each station across the ACP. As basin thickness increases TSs increases. **B.** Measurements of r_0 across the ACP. As basin thickness increases, the r_0 (related to the impedance contrast) decreases. **C.** Fundamental Frequency which is related to TSs as $F_0 = 12TSs$ across the ACP 79

Figure 3.5- Station measurements plotted vs. basin thickness. **A.** T_{Ss} increases with increasing basin thickness **B.** r_0 decreases with increasing basin thickness **C.** F_0 decreases with increasing basin thickness **D.** T_{PPbs} increases with increasing basin thickness **E.** PP_{bs} decreases with increasing basin thickness. 81

Figure 3.6- V_S velocity profile from inversion. **A.** T_{Ss} measurements from and 4Hz Ps RFs (cyan circles) compared to TSs predicted from the mean V_S profile from our best-fit inversion (black crosses) **B.** V_S velocity inversions using T_{Ss} measurements and assuming V_S increases in a power-law fashion with depth. A range of velocity inversions using all stations is plotted in gray, and the mean of these models is plotted in black 84

Figure 3.7- Station grouping between stations near the Mississippi Embayment (ME), red circles, and Coastal Plain (CP), blue circles **Error! Bookmark not defined.**

Figure 3.8- V_S velocity profile from inversion. **A.** T_{Ss} measurements from and 4Hz Ps RFs (cyan circles) compared to TSs predicted from the mean V_S profile from our best-fit inversion (black crosses) **B.** V_S velocity inversions using T_{Ss} measurements and assuming V_S increases in a power-law fashion with depth. A range of velocity inversions using stations with basin thickness less than 2.5 km are plotted in gray, and the mean of these models is plotted in black. The mean velocity inversion for the stations in the Mississippi Embayment (ME) is plotted in red, and the mean velocity inversion for the stations in the Coastal Plain (CP) is plotted in blue. 85

Figure 3.9- Parameters from VS profile inversion (p , a_1 , and VS_0) for all stations with basement thickness less than 2.5; ACP stations; ME stations 86

Figure 3.10- T_{PPbs} and PP_{bs} measurements from 4 Hz Ps receiver functions. With increasing sediment thickness, TPP_{bs} increases. **A.** Autocorrelation of Synthetic RF calculated for velocity model described in top right corner. T_{PPbs} and PP_{bs}

are picked as the largest positive amplitude, shown by the red dot. B. 4 Hz Ps RFs for station U60A located on 0.137 km of basin material. Mean Ps RF shown in blue and a range of Ps RFs shown in gray. T_{PPbs} and PP_{bs} pick shown as red dot. C. 4 Hz Ps RFs for station Q60A located on 1.07 km of basin material. Mean Ps RF shown in blue and a range of Ps RFs shown in gray. T_{PPbs} and PP_{bs} pick shown as red dot

87

Figure 3.11- Measurements from the 4Hz RFs across the ACP. A. Measurements of T_{PPbs} at each station across the ACP. As basin thickness increases T_{PPbs} increases. B. Measurements of r_0 across the ACP. As basin thickness increases, the amplitude of $PPbs$ (related to the impedance contrast) decreases.

88

Figure 3.12- V_P velocity profile from inversion. A. T_{PPbs} measurements from and 4Hz Ps RFs (magenta circles) compared to T_{PPbs} predicted from the mean V_P profile from our best-fit inversion (black crosses) and T_{PPbs} predicted from the Brocher (2005) relationship of V_P and V_S (green crosses) B. V_P velocity inversions using T_{PPbs} measurements and assuming V_P increases in a power-law fashion with depth. A range of velocity inversions using stations with basin thickness less than 2.5 km are plotted in gray, and the mean of these models is plotted in black. The mean velocity inversion for the stations in the Mississippi Embayment (ME) is plotted in red, and the mean velocity inversion for the stations in the Costal Plain (CP) is plotted in blue, and the V_P profile from the Brocher (2005) relationship is plotted in green. The velocity profile is not well constrained by any of the data.

90

Figure 3.13- Parameters from VP profile inversion (p , a_1 , and VS_0) for all stations with basement thickness less than 2.5; ACP stations; ME stations

91

Figure 3.14- V_P velocity profile from inversion. A. T_{PPbs} measurements from and 4Hz Ps RFs (magenta circles) compared to T_{PPbs} predicted from the mean V_P profile from our best-fit inversion (black crosses) and T_{PPbs} predicted from the Brocher (2005) relationship of V_P and V_S (green crosses) B. V_P velocity inversions using T_{PPbs} measurements and assuming V_P increases in a linearly with depth. A range of velocity inversions using stations with basin thickness less than 2.5 km are plotted in gray, and the mean of these models is plotted in black. The mean velocity inversion for the stations in the Mississippi Embayment (ME) is plotted in red, and the mean velocity inversion for the stations in the Costal Plain (CP) is plotted in blue, and the V_P profile from the Brocher (2005) relationship is plotted in green. The linear relationships for V_P agree with each other, and are consistent with the Brocher (2005) regression relationship.

91

Figure 3.15- Parameters from linear VP profile inversion b_1 and VS_0 for all stations with basement thickness less than 2.5; ACP stations; ME stations

92

Figure 3.16- Comparison of site fundamental frequency (F_0) measurements obtained in this study compared to more traditional spectral ratio techniques of estimating site fundamental frequency from peak amplitude. HVSR techniques applied to Radial (R, dark blue) and Transverse (T, cyan) component data recorded at the seismic station. SSR techniques applied to PRF data for create

"PRF spectral ratios" using 1Hz (pink) and 4Hz (red) PRFs. Method applied to three stations on differing basin thicknesses (U60A, Q59A, Q60A). 95

Figure 4.1- Major regions of interest in the southeastern United States modified from Wagner (2018) Topography is shown in the background. 9

Figure 4.2- The locations of USArray TA stations used in this study colored by the number of P-to-s (A) and S-to-p (B) receiver functions calculated at each station. Dark red circles are stations that have been deployed for a longer time. 107

Figure 4.3- Locations of CCP stacking points (blue) and stations (red triangles). Cross sections shown are calculated along vertical and horizontal lines in the grid. Each cross section number indicates a W-E cross section, while letters indicate a N-S cross-section. 110

Figure 4.4- The velocity assumption in H- stacking is extremely important and can significantly change inferred crustal properties. Results from traditional H-k stacks calculated for station 060Z on Atlantic Coastal Plain sediments. Top. As the assumed average crustal V_p velocity used to calculate the stacks increases, the crustal thickness estimate increases until a new maximum is inferred (at 6.5 km/s). Bottom. As the assumed average crustal V_p increases, the V_p/V_s ratio (or κ) decreases, until again a new maximum is inferred 111

Figure 4.5- Measurements of sediment phase arrival times at each station. The two way S-wave travel time in sediment (left) and the arrival time of the PP_{bs} phase (right) are shown. In regions with thicker sediment, both T_{Ss} (Δt) and $T_{PP_{bs}}$ (δt_P) are large, while in regions with thinner sediment T_{Ss} and $T_{PP_{bs}}$ are small. Stations in black do not demonstrate a sedimentary signal in the receiver functions. 113

Figure 4.6- Values of crustal H, κ , and V_p for each station in our study area obtained from H- κ - V_p stacking method (described in text). These parameters are used to calculate a velocity model for the migration of RFs from time to depth in the CCP stack 115

Figure 4.7- Results of CCP stacking for cross-section H (location shown in top panel of figure). Red indicates positive RF amplitude associated with a velocity increase with depth while blue indicates negative RF amplitude associated with a velocity decrease with depth. A. In traditional PRF CCP stacking we see large amplitude sediment reverberations that create a Moho step at about 327 km along the profile B. Sediment removed (SR) PRF CCP stacks remove much of the sediment reverberation contamination in the regions highlighted and show a flat Moho at 327 km along the profile. C. SRF CCP stacks show a similar Moho profile to SR PRF CCP stacks, but have lower resolution. 116

Figure 4.8- Examples of the resonance filter applied to PRFs. Gray is the mean of the PRFs before the resonance removal filter is applied, red line shows the mean of the PRFs after the sediment is removed. A. Station W61A in New Bern, NC. Before the sediment is removed, no clear Moho phase arrival (P_{ms}) exists in the RF. After the sediment is removed, a small amplitude peak appears at $\sim 5s$ which

is likely the Moho arrival. B. Station S60A in Water view, VA. Again, before the sediment is removed, no clear Moho phase arrival (P_{ms}) exists in the RF. After the sediment is removed, a evidence of a Moho arrival appears between 4-5 s. 117

Figure 4.9 - Figure 9- W-E Cross-section 22 showing a strong positive (red) arrival between 35 and 45 km depth. Right is the sediment removed (SR) PRF CCP stack and left is the SRF CCP stack. Stacks below show the variance of the RF amplitude at each point in the CCP stack. We interpret this positive Labels in black are features from Figure 1 that the cross sections pass through. RT= Rome trough, GF= Grenville front, SGR = South Georgia rift, ETSZ = eastern Tennessee seismic zone, BFZ = Brevard fault zone, CPS= central Piedmont suture, NCSQ = North Carolina seismic quiescence, AB = Appalachian basin, SCSZ = South Carolina seismic zone, SSZ = Suwanee suture zone, CVSZ = central Virginia seismic zone. Colored labels above each cross section denote the physiographic province that the cross sections pass through. CL = Central Lowland; AP = Appalachian Plateau, V&R = Valley and Ridge, BR = Blue Ridge, ACP = Atlantic Coastal Plain, LP = Interior Lower Plateau. 120

Figure 4.10- Crustal thickness/Moho depth from SR PRF CCP stacks. Contour figure of Moho depths shows a deep (~65km) Moho beneath the Blue Ridge and Appalachian Plateaus (~60 km) that shallows towards the coast (~25km). 121

Figure 4.11- W-E Cross-section 10, which passes through the maximum crustal thickness estimate in the Blue Ridge. Evidence of multiple crustal layers dipping sharply westward can be seen beneath the ETSZ and BFZ. The intra-crustal layer is at ~10 km beneath the CPS and deepens to ~40 km beneath the ETSZ, while the Moho phase in the same region begins at ~40km depth beneath the CPS and dips to ~60 km beneath the ETSZ and BFZ. The SRF CCP stacks also show a deep ~60 km Moho beneath the ETSZ and BFZ. A flat intra-crustal layer can also be seen beneath the NCSQ at about 15 km depth. Stacks below show the variance of the RF amplitude at each point in the CCP stack. See caption in Figure 9 for description of labels and abbreviations. 125

Figure 4.12- W-E Cross section 19 that shows an eastward dipping intra-crustal layer beneath the V&R and BR provinces in the SR PRF CCP stack. This intra-crustal layer appears at ~15 km beneath the Appalachian basin and dips eastward to ~20 km beneath the Piedmont. Stacks below show the variance of the RF amplitude at each point in the CCP stack. See caption in Figure 9 for description of labels and abbreviations. 126

Figure 4.13- Dip direction of intra-crustal layering at each CCP stacking latitude and longitude. Points indicate locations in the CCP stacking grid that show intra-crustal layering. Red points indicate locations where a westward dipping intra-crustal layer is seen, blue points indicate the latitude and longitudes where a flat intra crustal layer is seen, and blue indicates the location where an eastward dipping intra-crustal layer is identified. Purple shaded circles note the location of seismic zones in the SEUS, the brown line notes the predicted location of the Grenville Front (GF), and the green dotted lines indicate locations of suture

zones. In the south, the green line is interpreted as the Suwannee suture zone (SSZ) where in the north the green dotted line indicates a suture of unknown origin, but may be the suture between the Laurentian and Amazonian crust. 128

Figure 4.14- N-S cross section D which crosses through the main seismicity in the ETSZ. Here a strong mid-crustal discontinuity is seen dipping northward from ~10 km beneath the CPS/SSZ to ~20 km beneath the ETSZ and BFZ. In the same region, there is a sharp change in the crustal thickness from ~40 km to ~60 km beneath the BFZ/ETSZ. Stacks below show the variance of the RF amplitude at each point in the CCP stack. See caption in Figure 9 for description of labels and abbreviations. 129

Figure 4.15- W-E cross-section 16 through the CVSZ. Beneath the CVSZ we see an intra-crustal layer dipping slightly westward from around 15 km beneath the ACP and only deepens to 22-23 km beneath the BR. Directly below the CVSZ there is a change in crustal thickness from ~25 km to ~45 km over a later distance of about 100 km. Stacks below show the variance of the RF amplitude at each point in the CCP stack. See caption in Figure 9 for description of labels and abbreviations 131

Figure 4.16- N-S cross section H through the SCSZ. In this cross section the Moho appears fairly flat beneath the CL, AB, BR, and V&R. The only large change in the Moho depth occurs almost directly below the SCSZ in the Piedmont. Here the Moho changes from ~42 km to 30 km. Unlike Figures 15 & 16, no westward dipping intra-crustal layering is seen. Stacks below show the variance of the RF amplitude at each point in the CCP stack. See caption in Figure 9 for description of labels and abbreviations 132

Figure 4.17- W-E Cross-section 10 that passes through the NCSQ. Beneath the NCSQ in the ACP we see both a flat Moho at 40km and no strong evidence for intra-crustal layering. Stacks below show the variance of the RF amplitude at each point in the CCP stack. See caption in Figure 9 for description of labels and abbreviations 133

List of Abbreviations

AB: Appalachian basin

ACP: Atlantic Coastal Plain

AP: Appalachian plateau

BFZ: Brevard Fault Zone

BR: Blue Ridge

CCP: common conversion point

CPS: central piedmont suture

CVSZ: Central Virginia seismic zone

E-HVSR: earthquake horizontal to vertical spectral ratio

ETSZ: Eastern Tennessee seismic zone

GF: Grenville Front

F_0 : fundamental frequency

HVSR: horizontal to vertical spectral ratio

LAB: lithosphere-asthenosphere boundary

LP: lower plateau

Moho: Mohorovičić discontinuity

MLD: mid-lithospheric discontinuity

NCSQ: North Carolina seismic quiescence

PRFs/Ps RFs: P-to-s receiver functions

RFs: receiver functions

RT: Rome trough

SCSZ: South Carolina seismic zone

SEUS: Southeastern United States

SGR: South Georgia Rift

SR: sediment removed

SRFs:/Sp RFs S-to-p receiver functions

SRTC: sediment-removed time corrected

SSR: standard spectral ratio

SSZ: Suwanee Suture Zone

TA: transportable array

V_p : P-wave velocity

V_s : S-wave velocity

V&R: valley and ridge

$Z_{1.0}/Z_{2.5}$: depth to $V_s = 1.0$ or 2.5 km/s respectively

Chapter 1: Introduction to the Lithosphere and the Southeastern United States

Tectonic plates glide across the underlying mantle, shaping the history of our continents through collision and subduction. These plates make up the lithosphere, the Earth's topmost layer that includes the crust and rigid upper portion of the mantle. As continents collide and break apart making new continents and creating new tectonic plates, the lithosphere is deformed. Lithospheric structure then contains a history of the continental formation and evolution of a region as well as provides evidence for ongoing mantle dynamics. Observed variations in the lithospheric structure are often used to understand tectonic processes; thinned lithosphere implies extensional or rifting forces are at play, while thickened lithosphere implies compressional or collisional forces.

The southeastern United States (SEUS) has undergone multiple episodes of continental convergence and rifting, so mapping the boundaries of accreted terrains from previous collisional events – or inherited structures – can clarify the tectonic history of this region. Boundaries between inherited structures may also correlate with the ongoing seismicity of the region. Being distant from the nearest tectonic plate boundary, the damaging earthquakes observed in the SEUS cannot be explained by release of energy accumulated between plates moving with respect to one another. The long recurrence time of large intra-plate earthquakes makes them particularly dangerous and the location and magnitude of these events are difficult to predict. Mechanisms controlling the location of intra-plate seismicity are poorly understood,

but are likely related to preexisting zones of weaknesses in the crust or lithosphere inherited from past tectonic history of the SEUS.

A common seismological tool for imaging boundaries beneath the surface is receiver functions. Receiver functions are sensitive to discontinuities from differences in material properties such as the basin-bedrock interface, the crust-mantle boundary (often referred to as the Moho) and the lithosphere-asthenosphere boundary (LAB). The basin-bedrock boundary is important for understanding the long-period (low frequency) effects of shaking during an earthquake, which affects large buildings and structures. The largest ground motions are related to the depth and contrast between the basin-bedrock interface, and so constraining this across the SEUS will have implications for hazard analysis.

Constraining crust and Moho properties across the SEUS using receiver functions may help to understand the history of inherited structures and seismicity. Sharp changes in the Moho boundary may correlate with regions of seismicity or indicate locations of inherited crust; while the thickness and structure of the lithosphere in the SEUS is still debated, and further constraints might clarify the depth extent of the plate boundary. Variations in the LAB and other intra-lithospheric discontinuities may also be weak-zones related to inherited structures that correlate with seismicity. Currently, hazard estimates of intra-plate earthquakes use the ongoing seismicity in the area. These hazard assessments likely overestimate the hazard in regions with small seismicity and simultaneously underestimate the hazard in regions that have

may have the potential to produce large earthquakes but haven't in the historic past (*Stein and Liu, 2009*). By better understanding how lithospheric variations relate to currently active regions of seismicity, we may be able to predict locations of large and damaging intra-plate earthquakes in the future.

Although it is one of the more straightforward methods to studying lithospheric discontinuities, calculating receiver functions in the SEUS has proven difficult. Atlantic Coastal Plain sediments overlie the majority of the SEUS, and signal from sedimentary basins can overprint signals from deeper earth structure. Therefore, in my dissertation, I first develop a method to constrain the crust/mantle boundary in regions with sedimentary basins (Chapter 2), and then I constrain important basin/bedrock properties for hazard analysis in the SEUS (Chapter 3). Finally, I apply the new methodology to the SEUS to investigate the underlying lithosphere without sediment contamination (Chapter 4). This work has implications for improving characterization of lithospheric structure beneath regions with sediment, which may be up to 70% of the continental United States.

1.1 Overview of Chapter 2

Receiver functions are sensitive to sharp seismic velocity variations with depth and are commonly used to constrain crustal thickness. The H- κ stacking method of Zhu and Kanamori (2000) is often employed to constrain both the crustal thickness (H) and V_p/V_s ratio (κ) beneath a seismic station using P-to-s converted waves (Ps). However, traditional H- κ stacks require an assumption of average crustal velocity (usually V_p). Additionally, large amplitude reverberations from low velocity shallow

layers, such as sedimentary basins, can overprint sought-after crustal signals, rendering traditional H- κ stacking uninterpretable. We overcome these difficulties in two ways. When S-wave reverberations from sediment are present, they are removed by applying a resonance removal filter allowing crustal signals to be clarified and interpreted. We also combine complementary Ps receiver functions, Sp receiver functions, and the post-critical P wave reflection from the Moho (SP_{mp}) to remove the dependence on an assumed average crustal V_p . By correcting for sediment and combining multiple data sets, the crustal thickness, average crustal P-wave velocity, and crustal V_p/V_s ratio is constrained in geologic regions where traditional H- κ stacking fails, without making an initial P-wave velocity assumption or suffering from contamination by sedimentary reverberations.

1.2 Overview of Chapter 3

Thickness and seismic velocities of sedimentary basins strongly affect their response during earthquakes, prolonging and amplifying ground motions. We characterize shallow basin structure of the Atlantic Coastal Plain (ACP) using a passive-seismic approach based on high-frequency P-to-S receiver functions. We map the site-specific basin fundamental frequency for 64 USArray TA stations and confirm that the method yields results similar to those from traditional spectral ratio techniques, with basin fundamental frequencies between 0.1 and 1 Hz. In addition, using sediment S-wave reverberations and P-to-s phase arrival times measured directly from the receiver function, we invert for average basin S and P-wave velocity profiles of the ACP. We find that that V_s increases with depth following a power-law relationship ($V_s \propto \sqrt{z}$) while the increase of V_p with depth appears to be more linear. Finally, we

use variation of measured S-reverberation and P-to-s phase amplitudes with depth to validate the P and S wave velocity profiles for the ACP. These results have implications for seismic shaking across the ACP, which is home to millions of Americans.

1.3 Overview of Chapter 4

The Southeastern United States lies on a passive margin shaped by its complicated tectonic history of collisional events. Despite its distance from active plate margins, damaging earthquakes still occur whose mechanisms are poorly understood. Weaknesses in the lithosphere inherited from past collisional events are the most likely explanation, but the extent and magnitude of lithospheric variations in the SEUS has not been fully explored. Here, we use sediment removed P-to-s receiver functions (PRFs), combined with complimentary S-to-p receiver functions (SRFs), to constrain crustal and lithospheric variations across the entire SEUS. Through our investigation, we find evidence for deep mid-crustal layering (or a “double-Moho”) deepening westward beneath the blue ridge in eastern Tennessee as well as a shallow mid-crustal layer deepening eastward which has been interpreted to mark the location of the suture between Laurentia and Gondwana during the formation of the supercontinent Pangea (*Hopper et al. 2017*). We find no evidence for a strong lithosphere-asthenosphere boundary or mid-lithospheric discontinuities associated with the location of intra-crustal earthquakes; however, we find a correlation with sharp changes in the crustal thickness.

1.4 A Brief History of SEUS Tectonics

Here we provide a brief overview of the tectonic history of the southeastern United States (SEUS) beginning in the Proterozoic and continuing to modern day; generally following Wagner et al. (2018) who provide a more detailed tectonic history of the region.

The continental cratonic core of North America contains some of the oldest lithosphere on the planet. In the present day, this same cratonic lithosphere extends from the Rocky Mountains in the west to near the edge of the Appalachian Mountains in the east (Yuan et al., 2011). This core made up the continent Laurentia, and has remained stable since its formation in the Proterozoic. Between about 1.4 and 1.1 Gya the Grenville orogeny occurred which brought together multiple continental cores to create the supercontinent Rodinia (Whitmeyer and Karlstrom, 2007). The continent-continent collisions of the Grenville orogeny formed an extensive mountain range on the east coast of what is now the United States and Canada. Although the large mountains have eroded over time, evidence of their roots remain (Wagner et al., 2018). Much of what is now the SEUS did not exist at this time, and the exact location of westward extent of deformation that occurred during the Grenville orogeny, called the Grenville front (GF- **Figure 1.1**), remains elusive. Most studies agree that the extent of the GF is preserved past the Appalachian Mountains in what is now Tennessee and Ohio (Whitmeyer and Karlstrom 2007; Rivers et al., 2014). However, another suggests that the GF lies beneath the mid-continent rift in Wisconsin and Minnesota (Stein et al., 2018)

After a period of stability, Laurentia broke apart from the supercontinent Rodinia about 700 Mya and the vast Iapetus Ocean was formed. This major rifting event left other failed rifts within the SEUS including the Reelfoot Rift and the Rome Trough (RT- **Figure 1.1**) (*Whitmeyer and Karlstrom, 2007*). After this rifting event, further accretion occurred including the accretion of the Taconic island arc to New England and Canada during the Taconic Orogeny around 490-460 Mya. This event downwarped the crust and later erosion of these mountains led to the creation of the inland Appalachian Basin that overlaps some of the RT (AB- **Figure 1.1**) (*Clark, 2001*) With the subsequent closure of the Iapetus Ocean, additional accretion added an unknown number of terranes (*Hibbard, 2002; Hatcher, 2007; Hatcher, 2010; Hibbard 2010*) including some arc accretions. The accretion of the Taconic island arc and creation of the Taconic Mountains in New England downwarped the crust and created the Appalachian basin (AB-**Figure 1.1**). Constraining the number and extent of subsequent terrane accretions at depth is particularly challenging due to the massive re-working of the continent including crustal shortening and emplacement and possible changes in subduction vergence directions meaning that the underlying basement crust is often unknown (*Merschat and Hatcher, 2007; Wagner et al., 2012*). There is some evidence for the extent of the Piedmont terrane and Carolina terrane accretions (*Hibbard, 2000*) between 360-345 Mya and the boundary between the two, called the central piedmont suture is fairly well constrained (CPS- **Figure 1.1**)

The supercontinent Pangea formed with the collision of Gondwana and Laurentia during the Alleghanian orogeny beginning around 350 Mya (*Clark, 2001*). The

Alleghanian orogeny compressed and shortened the eastern margin of Laurentia at least 200 km (*Hopper et al., 2017*), creating the Appalachian Mountains and leaving the Brevard fault zone (BFZ- **Figure 1.1**), a series of major thrust faults between the Blue Ridge and the Piedmont that extend into the crust (*Christensen and Szymanski, 1988*). The suture zone of Gondwana and Laurentia is located off the coast of the SEUS for the most part, except for between Laurentia and the accreted Tallahassee-Suwanee terrane (of modern day Florida and Georgia) (SSZ- **Figure 1.1**- *Mueller et al., 2014; Hopper et al. 2017*).

The breakup of Pangea around 175 Mya marks the end of accreted terranes to the SEUS (*Whitmeyer and Karlstrom, 2007*). With the initiation of rifting came the formation of the South Georgia Rift basin (SGR **Figure 4.1**) and subsequent Central Atlantic Magmatic Province magmatism (*Whalen et al., 2015; Wagner et al. 2018*). As the SEUS transitioned into a passive margin, erosion and sedimentation along the eastern margin created the Atlantic Coastal Plain (ACP- **Figure 1.1**).

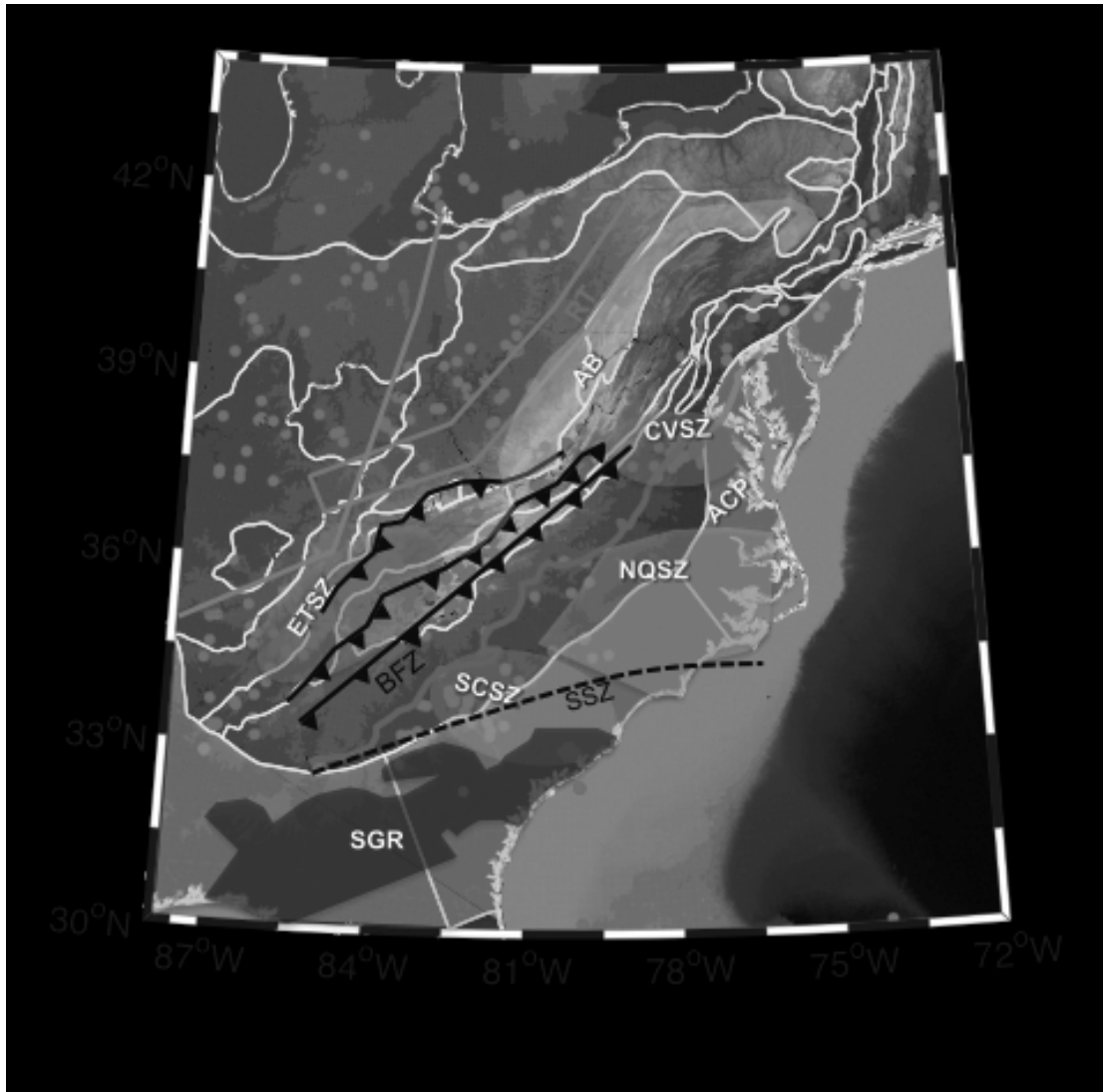


Figure 1.1- Major regions of interest in the southeastern United States modified from Wagner (2018) Topography is shown in the background. Red circles indicate the location of earthquake $M_w > 2.5$ since 1900. The brown line notes the location of the Grenville Front (GF) (Witmeyer and Karlstrom, 2007); Magenta indicates the region associated with the Rome Trough (RT), The Brevard Fault zone (BFZ) is shown as a series of lines with triangles (Powell et al., 2016). The blue line indicates the location of the Central Piedmont Shear Zone (CPS). Dotted black line is the location of the Suwannee suture zone (SSZ). Basins and rifts labeled in white with shaded regions showing their approximate extent. The seismogenic zones in purple are: ETSZ = eastern Tennessee seismic zone, SCSZ = South Carolina seismic zone, and CVSZ = central Virginia seismic zone while cyan is the NCSQ = North Carolina seismic quiescence. The SGR is the South Georgia Rift basin in black, AB = the 4000 ft contour of the sediment thickness of the Appalachian Basin which defines the deepest portions of the basin in orange, and light blue ACP region notes the location of the Atlantic coastal plain sediments.

1.5 Technical Background: Receiver Function Methodology

Layers in the earth (e.g. crust, mantle, core, etc.) contain different material properties that distinguish them from one another. The density, bulk, or shear modulus of a material can change the velocity of the seismic wave, reflecting changes in temperature and composition. Velocity and density differences (impedance contrasts) between different layers can be isolated using the receiver function method (*Langston, 1979*) and used to constrain their material properties.

Earthquakes produce a seismic wavefront that travels in all directions away from the source. Some energy from the seismic wave is recorded at distant seismic stations after traveling through the body of the earth. The resulting seismogram recorded at a station $u(t)$ can be considered the convolution (*) of functions describing the source, $s(t)$, and the structure, $g(t)$, of the earth that the seismic waves have passed through (*Figure 1.2*).

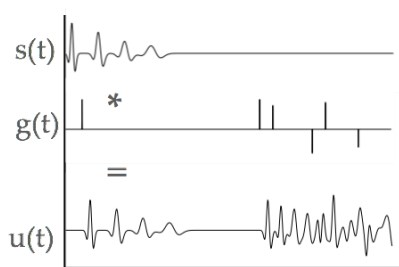


Figure 1.2 - Ideally the displacement recorded at a seismogram ($u(t)$) is the convolution of the source function ($s(t)$) and the earth response ($g(t)$). (Figure modified from Shearer, 2009)

In receiver function analysis, we aim to isolate the earth response, $g(t)$, which, in the case of receiver functions, is a result of seismic wavefield interactions with impedance discontinuities. To do this, the three-component seismograms are rotated in the direction of the earthquake source, upgoing P and S waves are estimated using near-surface velocities, and then the source-related signals $s(t)$ are removed through the process of deconvolution.

For an incoming P wave crossing a sharp velocity discontinuity, some of the energy from the direct P body waves is converted to a vertically polarized S wave (referred to as SV) across the discontinuity (**Figure 1.3**). A sharp discontinuity is one that occurs over a distance less than $\frac{1}{4}$ wavelength of the parent wave. In the case of the direct P wave, P is the parent and SV is the daughter waveform. Conversely, for an incoming S wave some of the SV energy is converted to a P wave (**Figure 1.4**); In this case SV is the parent wave and P is the daughter waveform. The parent waveforms contain the source information, $s(t)$, while the daughter waveforms contain the earth response information $g(t)$ convolved with source information $s(t)$. Receiver functions result from deconvolving source-related signals from the daughter using the parent waveforms. The relative amplitudes and arrival times of features in the receiver functions help constrain the earth's structure beneath the station (*e.g. Langston 1979, Farra and Vinnik, 2000*)

P - Converted Ray Paths

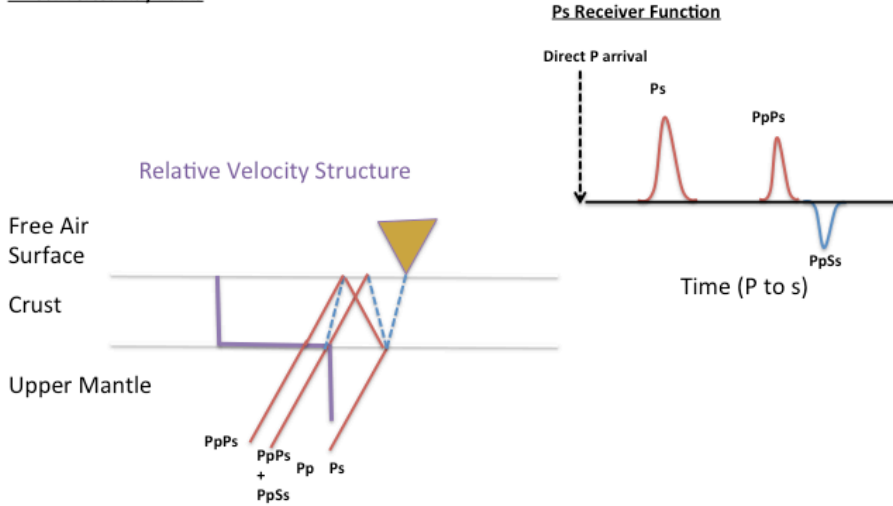


Figure 1.3 - Cartoon of converted P-wave energy across a Moho over mantle half space if no tilted axes of anisotropy are present. (Left) converted paths from a direct P wave at the Moho (P phases in red and S phases in dotted blue) and (right) their relative arrival times in a Ps receiver function.

S-Converted Ray Paths at MLD

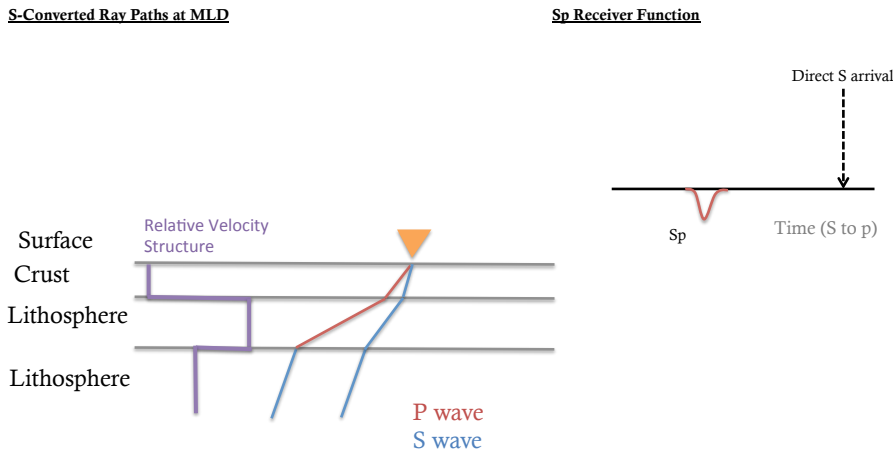


Figure 1.4- Cartoon of converted S-wave energy across a MLD over mantle half space if no tilted axes of anisotropy are present Left - converted paths from a direct S wave at the MLD (P phases in red and S phases in dotted blue) and Right - relative arrival times in a Sp receiver function.

1.5.1 Phase picking and P-SV-SH rotation

Often in receiver function studies, direct parent wave arrival times to each station are handpicked. However, due to the amount of data produced by USArray, handpicking waveforms for the entire array becomes impractical. For this reason, the automated

phase picking algorithm of Abt. et al. (2010) is used. In this algorithm, the predicted arrival of a parent phase is calculated through a 1-D velocity model (AK135) for the earth. To determine the actual arrival time, 25 seconds before and after the predicted arrival time is searched to find the arrival time that maximizes the ratio of the short term average (STA) to long term average (LTA), following the algorithm of Earle and Shearer (1994). If the maximum STA/LTA ratio is smaller than 2 then the predicted arrival from the 1-D model is used. Seismic stations record waveforms in 3 orthogonal components, often oriented to geographic North (N), East (E), and normal to the surface (Z). The N and E components are rotated relative to the earthquake source location to obtain motions in the radial (R) and transverse (T) directions. The R component describes the horizontal direction along which the P wave is propagating from the source, and the T component is orthogonal to R in the horizontal plane. The rotation is expressed mathematically given the back azimuth, θ (the angle of the earthquake location at the station from north):

$$(1.1) \quad \begin{bmatrix} R \\ T \end{bmatrix} = \begin{bmatrix} \cos\theta & \sin\theta \\ -\sin\theta & \cos\theta \end{bmatrix} \begin{bmatrix} N \\ E \end{bmatrix}$$

In order to isolate the converted phases in receiver functions, the components are transformed onto a coordinate system that isolates the parent and the daughter waveforms (P-SV-SH system). The waveform interaction at the free surface boundary can be described mathematically through the free surface transform matrix of Kennett (1991) and Bostock (1998) in terms of the P wave velocity (α), S wave velocity (β), and the horizontal slowness (ρ):

$$(1.2) \quad \begin{bmatrix} P \\ SV \\ SH \end{bmatrix} = \begin{bmatrix} \frac{p\beta^2}{\alpha} & 0 & \frac{\beta^2 p^2 - \frac{1}{2}}{\alpha q_\alpha} \\ \frac{1}{2} - \beta^2 p^2 & 0 & p\beta \\ \beta q_\beta & 0 & 0 \\ 0 & \frac{1}{2} & 0 \end{bmatrix} \begin{bmatrix} R \\ T \\ Z \end{bmatrix}$$

where q_α and q_β are vertical slownesses of P and S waves, respectively, defined by the equations:

$$(1.3) \quad q_\alpha = \sqrt{\alpha^{-1} - p^2} \quad \text{and} \quad q_\beta = \sqrt{\alpha^{-1} - p^2}$$

This transformation matrix describes how the seismic wavefield interacts at the free surface. The matrix transformation should isolate the parent and daughter phases allowing for deconvolution to take place.

1.5.2 Deconvolution

Deconvolution is the method by which I can isolate converted phases arrivals (s in Ps and p in Sp) to infer underlying velocity and geologic structure. In terms of the parent and daughter waveforms, the daughter waveform (d) can be written as the convolution (*) of the earth response (g) with the upgoing parent (p) waveform. Convolution in the time domain can be described as the integral of one signal with another that is reversed and shifted in time. Mathematically this is written as:

$$(1.4) \quad d(t) = g(t) * p(t) = \int_{-\infty}^{\infty} g(t - \tau) p(\tau) d\tau$$

Convolution in the time domain is equivalent to multiplication in the frequency domain and so equation can be expressed as:

$$(1.5) \quad D(w) = G(w) P(w),$$

where $D(w)$, $G(w)$, and $P(w)$ are the Fourier transform of the time domain signals $d(t)$, $g(t)$, and $p(t)$ respectively. It seems simple then to isolate earth response as the spectral division (though this is usually a bad idea in practice due to zeros and near-zeros of $P(w)$):

$$(1.6) \quad G(w) = \frac{D(w)}{P(w)}$$

The earth structure $G(w)$ can be transformed back into the time domain by taking the inverse Fourier transform. Because the time domain is related to the frequency domain through as Fourier transform, it should be possible to calculate equivalent and interchangeable receiver functions in either the time or frequency domain. There are two common methods of deconvolution that have been used most often to calculate stable RFs. The first is a variation of frequency domain deconvolution method of Bostock (1998); the second is an iterative deconvolution in the time domain following Ligorria and Ammon (1999). Because each deconvolution method has tradeoffs, both

methods are used and compared in our study. In the future, we could include the trans-dimensional hierarchical Bayesian deconvolution (THBD) developed by Kolb and Lekic (2014). The THBD method allows for an estimation of inversion likelihood through Bayesian statistics, but comes at the cost of much higher computation time.

1.5.3 Frequency Domain Deconvolution

Although the spectral division shown in equation 6 looks straightforward, complications can arise that make the deconvolution unstable. For example, if the denominator becomes sufficiently small, the deconvolution can in effect “blow up”. I can stabilize (i.e. “regularize”) the deconvolution by multiplying both the numerator and denominator by the complex conjugate $P^*(w)$ of the parent waveform and adding a small factor to the denominator. This is the frequency domain damped least squares deconvolution (Bostock 1998):

$$(1.7) \quad G(w) = \frac{D(w)P^*(w)}{P(w)P^*(w)+\delta}$$

the small factor, δ , in this case is the best regularization parameter. The best regularization parameter is the one that minimizes the generalized cross validation function (GCV). The GCV computes $G(w)$, convolves it with the parent to calculate a predicted daughter waveform, and then computes its misfit to the observed daughter. This is repeated over a range of regularization parameters (δ). The smallest GCV indicates which regularization parameter should be used. Adding the regularization parameter means that the least squares frequency domain deconvolution is not a pure

deconvolution, but it prevents the spectral division from “blowing up” by ensuring a non-zero denominator for division. **Figure 1.5** demonstrates the effect of changing the regularization parameter on the resultant receiver function for TA station J27A located in Hobbs, New Mexico.

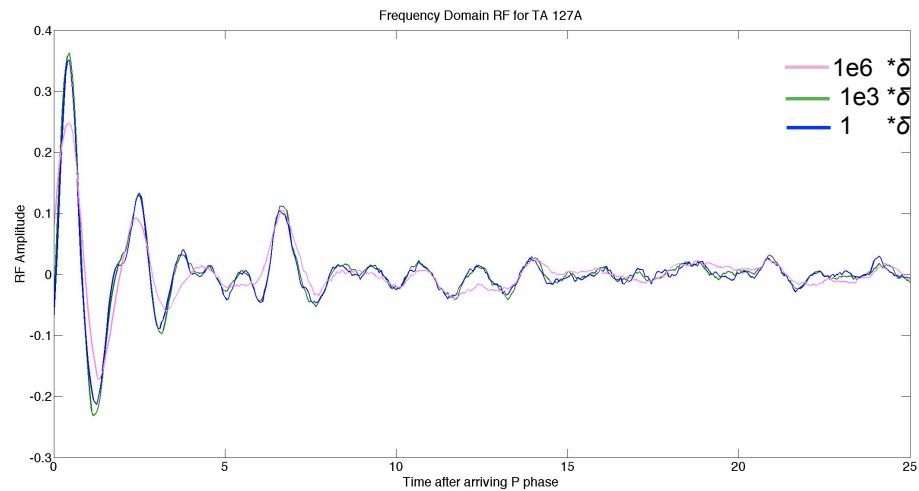


Figure 1.5— Ps RF for station 127A located in Hobbs, New Mexico. The y-axis shows the fraction of the amplitude of direct P arriving phase, the x-axis is in time.

The resulting RFs are shown when the regularization parameter δ is multiplied by 1 (blue line), 1000 (green line), or 10^6 (pink line). The conclusion drawn from this figure is that δ alone (without any further modification) is enough to stabilize the deconvolution.

As expected, a larger multiple of the regularization parameter in the denominator increases the stability but reduces the amplitudes of arriving phases to the solution. However, the integrity of the receiver function and phases arrivals remains consistent. A benefit of using the frequency domain deconvolution is that it is computationally

efficient. This is especially important when considering the large amount of data collected in the USArray.

Frequency domain RFs are computationally fast and fairly reliable, however, other methods may sometimes be preferred. Narrow spikes (relating to the impedance contrast of earth structure) exist in the time domain, and are associated with Fourier transforms whose power spans multiple frequencies. For example, the Fourier transform of a delta spike signal in the time domain has infinite width in the frequency domain. A longer duration signal, like a boxcar function will produce a Fourier transform that looks like the sinc function (**Figure 1.6**). Simply put, the more defined or sharp a pulse is in the time domain, the larger its extent in the frequency domain. This spectral extent of signals can interfere with spectral contribution of later arriving phases on a receiver function, or be distorted by the band-limited nature of the data itself, which only has usable signal-to-noise ratios across a relatively narrow band of frequencies. This means that when computing RFs, there is a tradeoff between localization of signals in time versus frequency. This is also the case with time-domain deconvolution methods.

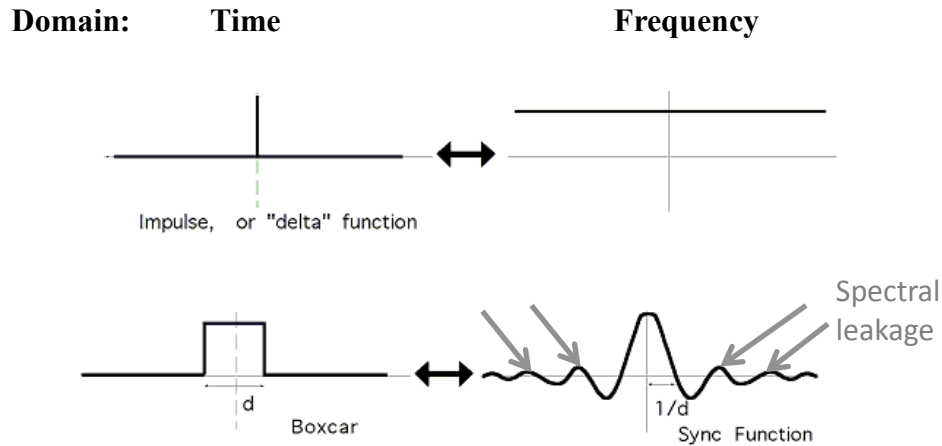


Figure 1.6- Fourier transform from time to frequency domain for common functions. Arrows indicate the Fourier transform was taken. Top - delta function in the time domain yields a flat spanning all frequencies in the frequency domain. Bottom - boxcar function in the time domain yields a sinc function with multiple frequencies (spectral leakage) in frequency domain.

1.5.4 Time Domain Deconvolution

The time domain simultaneous least squares deconvolution of Kikuchi and Kanamori (1982) and Ligorria and Ammon (1999) presents an alternate method of deconvolution. Instead of employing spectral division, a cross correlation of the parent and daughter components is performed. A Gaussian peak is introduced at a time lag that corresponds to the maximum cross correlation; this is then convolved with the parent component and subtracted from the daughter component. The width of the Gaussian peak used in the deconvolution is related to the frequency-time localization tradeoff discussed above in Chapter 1.1.3. The process is repeated until the set number of iterations is met. This method limits the addition of spectral artifacts in station TA 127A (**Figure 1.6**). The signal from the time domain receiver functions appears to be much more clear than the previous frequency domain

deconvolution, and the presence of side lobes is greatly reduced. However, the number of iterations determines the resolvability of each receiver function – a parameter chosen a priori, and the computation time is significantly larger.

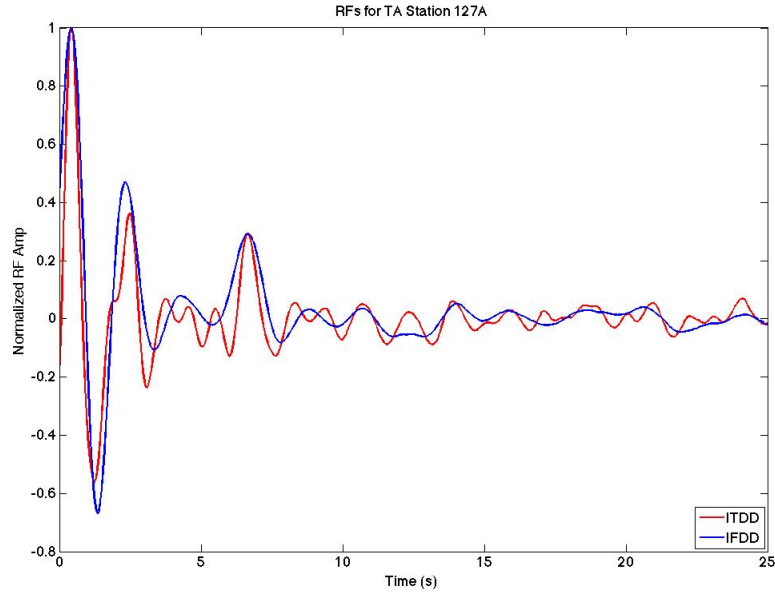


Figure 1.2– Time (ITDD in red) and Frequency (IFDD in blue) domain RF comparison for station 127A located in Hobbs, New Mexico. IFDD RF was filtered at 0.03-1 Hz and appears overall smoother than the ITDD RF. However, it is difficult to determine if the Ps arrival associated with the Moho occurs at 3.5 or 6 s. The ITDD RF was created with 300 iterations and appears to have more arriving phases, however, the spectral leakage has been reduced and the peaks narrow. The RF amplitudes for both frequency and time domain RFs have been normalized to 1.

Chapter 2: Constraining Crustal Structure in the presence of Sediment: A Multiple Converted Wave Approach

2.1 Introduction and Rationale for New Methodology

Across a sharp seismic impedance contrast, some of the seismic energy from direct teleseismic P waves converts to SV wave energy, and vice-versa. Receiver functions (RFs) isolate the time series of converted wave energy directly beneath a seismic station by deconvolving the parent waveform (P for P-to-s conversions and S for S-to-p) from the daughter waveform (S for Ps and P for Sp), removing complexity in the signal due to earthquake rupture and distant structure. RFs are sensitive to sharp seismic velocity variations with depth and are therefore used to constrain shallow crustal and lithospheric velocity discontinuities such as the boundary between the crust and mantle (Mohorovičić discontinuity or Moho) (*e.g Vinnik, 1977; Langston, 1979; Owens et al., 1984*). Stacking the amplitudes of RFs at the expected arrival times of the converted phase across the Moho and its primary reverberations (multiples) for a range of crustal thickness (H) and relative velocity (V_p/V_s ratio or κ) values will produce a maximum of the stack corresponding to the best estimate for H and κ (*Zhu and Kanamori, 2000*). Due to its simplicity and exploitation of both direct converted and reverberating phases, H- κ stacking has become a widely used method to obtain an estimate of the average crustal thickness and velocity beneath a seismic station. Traditional H- κ stacking has been used extensively to estimate the thickness and V_p/V_s of the crust (*Kumar et al., 2001; Ramesh et al., 2002; Eaton et al., 2006; Rychert et al., 2007; Audet et al., 2009; French et al., 2009; Yuan et al., 2010; Levander and Miller, 2012; Parker et al., 2013; Reeves et al., 2015; Biryol et al.,*

2018; Soto-Cordeo et al., 2018). With the deployment of large-scale seismic arrays, such as the EarthScope USArray, automated RF analysis in the form of H- κ stacking has been deployed to constrain crustal structure on a continental scale (Crotwell and Owens, 2005). While straightforward, the traditional method of Ps H- κ stacking is limited by two major factors: 1) The prior assumption of an average crustal velocity beneath a seismic station and 2) Contamination of crustal signal by sediment or other shallow-layer reverberations. These limitations have proved difficult to overcome, and can significantly bias estimates of crustal thickness and V_P/V_S ratios based on them.

Several studies have quantified how assuming an incorrect average V_P can bias crustal thickness and V_P/V_S estimates from H- κ stacks by up to 10s of kilometers for H (Sheehan, 1995; Zelt and Ellis, 1999; Yeck et al., 2013). At some locations, an accurate crustal velocity may be obtained from active source experiments or surface wave inversion studies; however, a continental scale study requires that these measurements are available at all locations and reflect the same region of lateral sensitivity as the receiver functions (Chai et al., 2015; Rychert and Harmon, 2016). Though Ps RFs do have some sensitivity to average crustal V_P (Kumar and Bostock, 2008; Bostock and Kumar, 2010), it is typically insufficient to provide robust estimates of V_P beneath the seismic station. Therefore, to remove the dependence on V_P , Sp RFs can be combined with Ps RFs to create stacks that constrain average crustal H, V_P , and V_S (Rychert and Harmon, 2016). The S-to-p wave conversion from the Moho arrives before the direct S, meaning that Sp RFs are not contaminated by

sediment reverberations in the same way as Ps RFs, although, Sp RFs have a smaller amplitude conversions and typically contain energy at lower dominant frequencies than Ps RFs. Because vertical resolution depends on frequency content, lower frequency Sp RFs yield a lesser vertical resolution. Due to the relatively low signal to noise ratio of Sp converted phases, the large amplitude post critical P reflection from the Moho, called the SP_{mp} phase, can be used to constrain average crustal P wave velocity (*Langston 1996; Owens and Zandt, 1997; Yu et al., 2012; Kang et al., 2016; Parker et al., 2016*). While the SP_{mp} phase has a broad region of lateral sensitivity, it is less impacted by sediment reverberations and depends on average crustal V_P and crustal thickness, rather than V_S .

However, even once crustal V_P is well constrained, a slow sedimentary layer beneath a seismic station can significantly bias crustal thickness estimates (*Yeck et al., 2013*) and large amplitude sediment reverberations can directly overprint Ps conversions from the Moho, rendering interpretation of Ps H- κ stacks challenging (*Zelt and Ellis, 1999*). Previous studies have removed sediment reverberations with some success, but these methods fail if more than one sedimentary layer exists or if sedimentary phase arrivals directly overlap Moho arrivals. (*Yeck et al., 2013, Wölbern and Rümpker 2017*), and require an assumption about average crustal V_P (*Yu et al., 2015*). Currently no single method overcomes limitations of traditional H- κ stacking, the assumption of crustal V_P , and contamination by one or many sedimentary layers.

To constrain average crustal thickness, V_P , and V_P/V_S in sediment dominated regions, contamination from sediment reverberations should be removed and data with complementary sensitivity should be incorporated. We propose a method that applies a resonance removal filter to Ps RFs when contaminated by sediment, and combines these sediment-removed Ps RFs with Sp RFs as well as the envelopes of SP_{mp} RFs. Stacking these three complementary datasets across a range of H , κ , and V_P and accounting for slowness in sedimentary layers yields a maximum at H , κ , and V_P values corresponding to the best estimate of all three crustal parameters. We call this method is called the sediment-removed, time-corrected (SRTC) H - κ - V_P triple stack. The ability of this method to constrain the crustal structure is demonstrated using synthetic data and results from three different geologic/tectonic regions using recordings from USArray Temporary Array (TA) stations. The two main benefits of this method are that it constrains all three crustal parameters in regions where sediment reverberations contaminate Ps RFs and that it can be automated to calculate these values for continental scale seismic arrays such as the EarthScope USArray.

2.2 SRTC H - κ - V_P Stacking

By removing source and path effects through deconvolution, receiver functions isolate the near receiver structure. Deconvolution can be performed in the frequency domain using modified spectral division (*Clayton and Wiggins, 1976; Bostock, 1996; Dueker and Sheehan, 1997; Lawrence and Shearer, 2006*); however, we choose to employ the time domain simultaneous least squares deconvolution of Kikuchi and Kanamori (1982) and Ligorría and Ammon (1999) to reduce the appearance of side

lobes. (For a full discussion of receiver function deconvolution techniques see Pesce, 2010) Traditionally, these Ps RFs are calculated and then stacked along predicted phase arrival times over a range of crustal thickness (H) and crustal velocity (V_P/V_S ratio or κ) to create H- κ stacks (Zhu and Kanamori 2000).

In this study, we review traditional H- κ stacking (section 3.1) and then introduce the approach for removing and correcting for shallow-layer reverberations (section 3.2), which is based on the resonance removal filter of Yu et al (2015). We then introduce and discuss metrics that allow us to determine when the shallow-layer corrections are needed (section 3.3). Once contamination from sediment reverberations has been removed, the complementary Sp (section 3.4) and SP_{mp} (section 3.5) data are added to form a SRTC H- κ - V_P triple stack (section 3.6). This SRTC H- κ - V_P stack explicitly removes the need to assume a crustal velocity, and thereby improves confidence in our estimates of crustal thickness and velocity.

2.2.1 Ps receiver functions in traditional H- κ - V_P stacks

The direct P-to-s conversion across the Moho (P_{ms}) is often used to constrain the Moho depth. The Moho depth estimate can be improved by including the multiple later arriving P-to-s primary reverberations, PP_{ms}, and PS_{ms}+ P_{ms}SP_{ms} whose ray paths are shown in **Figure 2.1A** and relative arrival times are shown in **Figure 2.1B**. The expected arrival time of the direct conversion and primary reverberations relative to the direct P wave arrival depend differently on crustal thickness (H) and crustal velocity (V_P and V_S) given a ray parameter (p) of the teleseismic P wave:

$$(2.1) \quad t_{P_{mS}} = H \left(\sqrt{V_S^{-2} - p^2} - \sqrt{V_P^{-2} - p^2} \right)$$

$$(2.2) \quad t_{PP_{mS}} = H \left(\sqrt{V_S^{-2} - p^2} + \sqrt{V_P^{-2} - p^2} \right)$$

$$(2.3) \quad t_{PS_{mS}} + t_{P_{mS}P_{mS}} = 2H \sqrt{V_S^{-2} - p^2}$$

Each Ps receiver function, $f_j(t)$, corresponds to incident P waves of ray parameter, p_j , where j is the index of the individual RF. By assuming H , κ , and an average crustal velocity, V_p , eqns. 1-3 can be used to compute the expected arrival times of the direct conversions and reverberations. The weighted sum of all N Ps receiver functions obtained at a seismometer are evaluated at the arrival times expected across a range of trial H and κ values to yield an H - κ stack:

$$(2.4) \quad s_{PS}(H, \kappa) = \sum_{j=1}^N w_1 f_j(t_{P_{mS}}) + w_2 f_j(t_{PP_{mS}}) - w_3 f_j(t_{PS_{mS}} + t_{P_{mS}P_{mS}})$$

Where w_1 , w_2 , and w_3 are the relative weights of the three phases. The most likely H and κ beneath the seismic station will be associated with largest amplitudes of the weighted sum, s_{PS} using the same weight values as Zhu and Kanamori (2000) where $w_1 = 0.7$, $w_2 = 0.2$ and $w_3 = 0.1$.

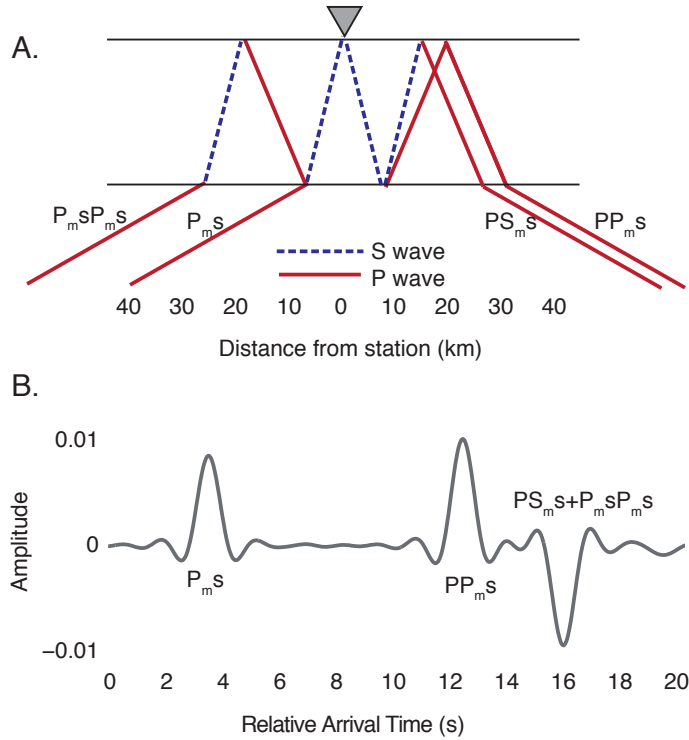


Figure 2.1- **A.** Ray-path geometry and **B.** synthetic receiver functions of P-to-s phases converted across the Moho at 30 km depth, from an incident plane wave of horizontal slowness 0.06 s/km. Crustal $V_P = 6.3$ km/s, $V_S = 3.7$ km/s, while mantle $V_P = 8$ km/s and $V_S = 4.6$ km/s. Arrival times of the direct Moho P-to-s conversion and first-order multiples are relative to the arrival time of the direct P wave.

In theory, Ps receiver functions spanning a range of ray parameters should contain information needed to constrain V_P on their own when stacked over a range of H , κ , and V_P values (Kumar and Bostock, 2008; Bostock and Kumar, 2010). Therefore Ps RF stacks are calculated over a range of average crustal V_P values creating a Ps RF H - κ - V_P triple stack, which is calculated in eq. (2.7) and is called $s_{Ps}(H, \kappa, V_P)$, where the absolute maximum should correspond to the most likely average crustal values beneath the seismic station. In practice, when shallow-layer reverberations are present, it is necessary to first remove their signature before determining V_P ; this procedure is discussed procedure in Section 1.3.2. Furthermore, noise in the receiver

functions and the range of incident ray parameters can prevent robust estimation of V_p , requiring the incorporation of independent data constraints; these independent constraints are discussed in Sections 1.3.3 and 1.3.4.

2.2.2 SRTC Ps receiver function H- κ - V_p stacks

When sedimentary layers are present, energy from conversions produced across the impedance contrast at the base of the sediment and reverberations within the sediment can get trapped within the low-velocity layer. These conversions and reverberations can produce large amplitude, long duration, and oscillatory (ringy) signals, which can directly overprint smaller amplitude signals from the Moho. The ray paths for the direct sediment conversion P_{bs} , and reverberations PP_{bs} , PS_{bs} , P_{bs} -2S, PP_{bs} -2S, PS_{bs} -2S, P_{bs} -4S, etc. are shown in **Figure 2.2A**, and relative arrival times are shown in **Figure 2.2B**. In Ps receiver functions, the largest amplitude, longest duration oscillatory reverberations are those that contain two S-legs in the sediment (the S-wave reverberations: PS_{bs} , P_{bs} -2S, PP_{bs} -2S, P_{bs} -4S, etc. **Figure 2.2B**), this is due to fact that Ps receiver functions are rotated, and the larger $\hat{S}\hat{S}$ reflection coefficient at the base of the layer, meaning the reverberations at longer times contain primarily S-wave energy (**Figure 2.3**). Even though the PP_{bs} phase arrival has large amplitude, it would only interfere with the P_{ms} Moho conversion when the crust is extremely thin (<20 km) and the sediment is both thick and unreasonably slow (**Figure 2.4**). Therefore, to interpret later arriving Moho signals in the Ps receiver function, the periodic S-wave sediment reverberations must be removed.

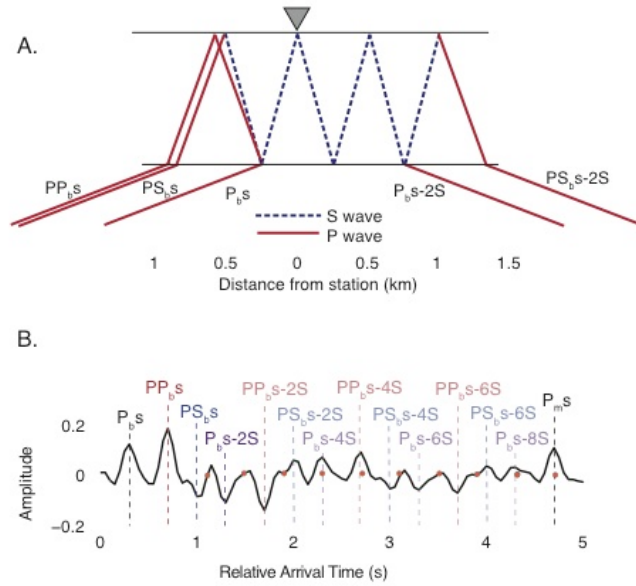


Figure 2.2- *A.* Ray-path geometry of P-to-s phases converted across the base of a 0.5 km thick sediment layer, along with the largest-amplitude first- and second-order multiples for an incident plane wave of horizontal slowness 0.0789 s/km. *B.* Synthetic receiver functions computed for a model with a 0.5 km thick sediment layer and horizontal slowness 0.06 s/km ($V_P = 2.5$ km/s, $V_S = 1$ km/s), crustal $V_P = 6.2$ km/s, $V_S = 3.5$ km/s, a Moho at 35 km depth, and mantle $V_P = 8$ km/s, $V_S = 4.6$ km/s. Direct conversions are in black, while the oscillatory pattern is attributed to sediment multiples, labeled in red, blue and purple. Orange dots indicate where the expected arrival of phases with more than 2 P-wave legs would arrive.

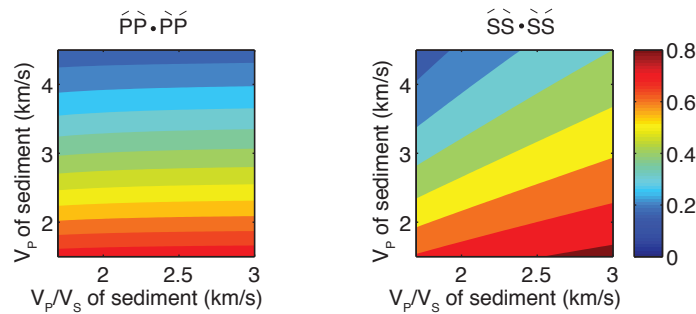


Figure 2.3- Absolute value of the reflection coefficients of PP*PP (left) and SS*SS (right) for a range of different sediment velocity variables using equations from Aki and Richards (1980) Because each reverberation will need to be

multiplied by an PPPP or SSSS reflection coefficient, the reverberations will get smaller, but the PPPP reverberation will get smaller faster, and SS*SS reverberations will remain visible in the Ps receiver function (See **Figure 2.2**).

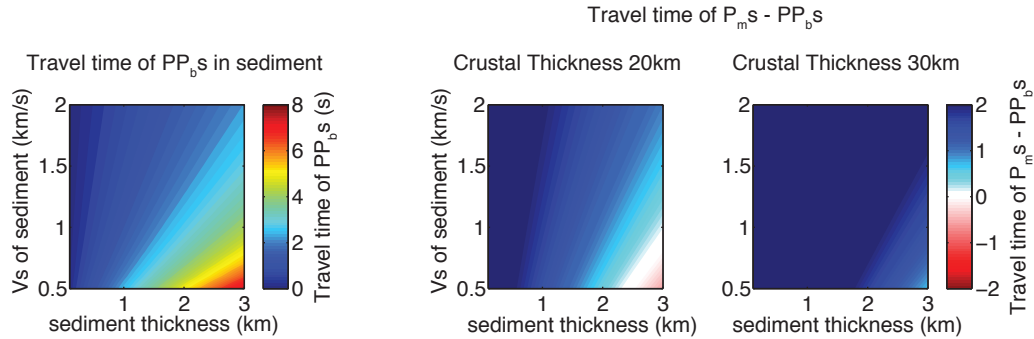


Figure 2.4- The SRTC H-k-VP stacking method may not work when the PP_{bs} and P_{ms} phase arrival intersect. (Left) Calculated PP_{bs} arrival time from sediment with varying thickness and V_S . The V_P/V_S ratio changes according to the mud line equation in Brocher (2005). (Right) the $P_{ms} - PP_{bs}$ arrival time for a crust with $V_P = 6$ km/s and $V_P/V_S = 1.76$. Area where the PP_{bs} arrival may interfere with the P_{ms} Moho arrival is shown in light blue to red. SRTC stacking may not work for an extremely thin crust of 20 km, if sediment thickness is greater than 1.5 km with excessively low V_S of 0.5 km/s.

The S-wave sediment reverberations can be suppressed from the Ps RF by applying a resonance removal filter proposed by Yu et al. (2015). The S reverberations have a resonant frequency associated with the two-way travel time of the S-wave in the sediment layer. A resonance removal filter can be constructed using the travel time of the S reverberation in sediment, Δt , and the relative strength of the S-wave reverberation, r_0 . While these values can be inferred directly from the Ps RF, both Δt and r_0 can be more reliably measured on the autocorrelation of the receiver function. In sediment, the autocorrelation of the Ps RF will have a decaying sinusoid pattern, showing a large, negative peak with amplitude r_0 , at time lag Δt (**Figure 2.5A**). A consistent method for determining these parameters, even when the autocorrelation is

complex with multiple minima (which suggests multiple shallow layers) involves finding the best-fit decaying sinusoid to the autocorrelation function of the form:

$$(2.5) \quad m(t) = ce^{-at} \cos\left(\frac{\pi t}{\Delta t}\right),$$

where t is the lag time of the autocorrelated RF, and the three parameters sought through the fitting procedure are the half-period of the oscillation, Δt , the amplitude of the autocorrelation at zero lag time, c , and the decay constant a . Because the half-period of the oscillation is precisely the travel time of the S reverberation, $m(\Delta t) = r_0$, both parameters of the resonance removal filter can be estimated (**Figure 2.5A**). While these parameters should depend somewhat on ray parameter, the lateral proximity of the S reverberation bounce points to the station for the range of teleseismic ray parameters means that this dependence is in practice small enough that computing a single best-fitting set of parameters across all ray parameters is justified (at least in the idealized synthetic case of **Figure 2.6**). For example, when sediment is 2 km thick with a $V_p = 2.5$ km/s and $V_s = 2.1$ km/s, the PS_{bs} reflection for an event with epicentral distance of 90 degrees may occur just 0.19 km from the station, while that for an event with epicentral distance of 30 degrees will occur 0.37 km from the station. Therefore the best-fit decaying sinusoid is found to the autocorrelation of the mean Ps RF at the station. The benefit to using **eq. (2.5)** is that it can be easily automated and may simplify the interpretations of Δt in complicated or noisy auto correlated signals. Furthermore, calculating the resonance removal filter on the mean Ps receiver function at each station has the benefit of leveraging more

waveforms to suppress noise and thereby stabilizes the inference of the optimal resonance removal filter parameters.

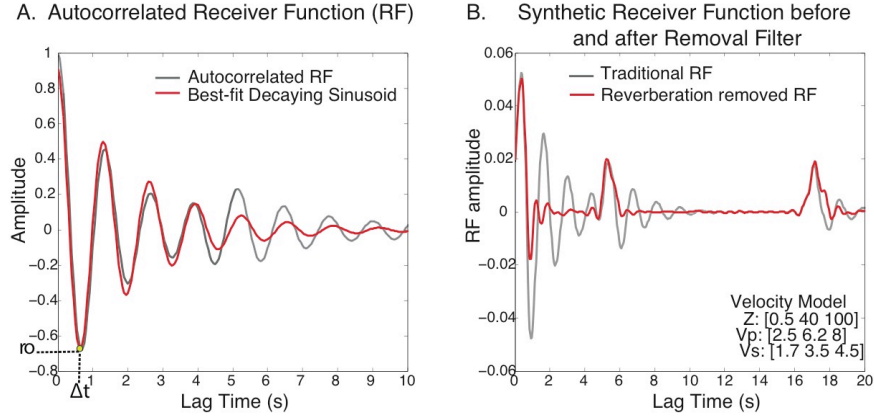


Figure 2.5- *A.* The autocorrelation of the mean synthetic receiver function (gray) and the best fit decaying sinusoid (red) used for determining the parameters of the resonance removal filter. The first large amplitude negative peak corresponds to the two-way s travel time in sediment (Δt) on the x-axis and the amplitude of the sediment reverberations (r_0) on the y-axis. *B.* Mean synthetic Ps receiver functions before (gray) and after (red) the resonance removal filter is applied; the filter successfully removes the reverberations and the direct P to s conversion across the Moho becomes clear.

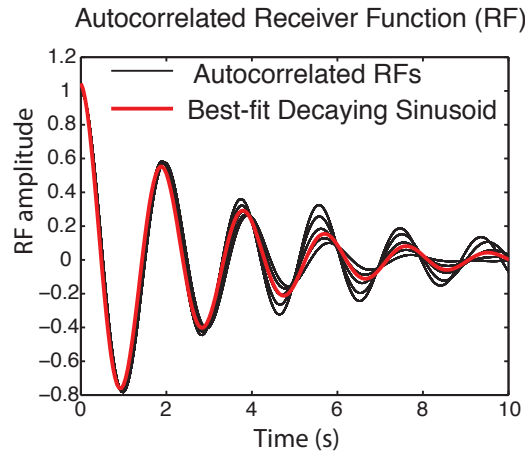


Figure 2.6- Dependence of resonance removal filter on ray parameter for an idealized synthetic case. The best-fit reverberation removal filter (red line) calculated from the autocorrelation of the mean synthetic receiver function provides a good fit to the autocorrelations of Ps RFs computed across the range of

possible ray parameters (black lines). The synthetic model used has a sediment layer 0.5 km thick with a $V_P = 2.5$ km/s and a $V_S = 1.7$ km/s overlying a 39.5 km crust with $V_P = 6.2$ km/s and $V_S = 3.5$ km/s and mantle with $V_P = 8$ km/s and $V_S = 4.5$ km/s.

Once the parameters Δt and r_0 are found, the resonance removal filter can then be constructed in the frequency domain:

$$(2.6) \quad F(\omega) = 1 + r_0 e^{-i\omega\Delta t}$$

The resonance removal filter is applied in the frequency domain by multiplying it with the Fourier Transform of the Ps RFs. We verify that the reverberations are successfully suppressed from the resulting receiver function, clarifying the later arriving P-to-s Moho phase (**Figure 2.5B**).

Although applying a resonance removal filter makes conversions from the Moho interpretable, it does not correct for the time delay that the Moho-related phases accumulate through the slow sedimentary layer. If the sediment time delay is not corrected when stacking the Ps receiver functions in the H- κ - V_P stacks, an incorrect crustal thickness estimate will be obtained (Yeck *et al.*, 2013; Yu *et al.*, 2015). Because slow sedimentary layers cause the assumed average crustal V_P to be lower than the actual V_P , the crustal thickness will be underestimated and the V_P/V_S will be overestimated.

To address this problem, the Moho phase arrivals used in the H- κ - V_p stack can be adjusted for the sediment time delay by using either the P_{bs} phase arrival, which will be the first large amplitude arrival on the receiver function (Yu *et al.*, 2015), or the PP_{bs} phase which is the largest amplitude arrival on the receiver function. The arrival time of the P_{bs} phase (δt) and the PP_{bs} (δtP) phase can overlap, especially in lower frequency (1Hz) P_s RFs. It is easiest to identify these phases on high frequency (4 Hz) P_s RFs. Using the high frequency RFs allows for tighter constraints on δt or δtP and helps separate the P_{bs} phase arrival from the PP_{bs} phase arrival when the sediment layer is thin (less than 0.5 km). In our automated procedure, we found it was easier to measure the arrival time of the larger phase δtP instead of the first arriving phase δt . Once δtP is determined, the predicted Moho phase arrival times are accounted for in computing the time adjusted H- κ - V_p stack:

$$\begin{aligned}
 (2.7) \quad s_{P_s}(H, \kappa, V_p) &= \sum_{j=1}^N w_1 f_j(t_{P_{ms}} + \Delta t - \delta tP) + w_2 f_j(t_{PP_{ms}} + \delta tP) \\
 &\quad - w_3 f_j(t_{P_{s_{ms}}} + t_{P_{ms}P_{ms}} + \Delta t)
 \end{aligned}$$

When sedimentary layers are present, **eq. (2.7)** corrects for the sediment delay time and yields an estimate of the sub-sediment crustal thickness. Using the mud-line equation from Brocher *et al.* (2005), which is appropriate for unconsolidated sediments, we assume a relationship between V_p and V_s in sedimentary layers. This relationship can be used to approximate the V_p , V_s , and thickness of sedimentary or shallow layer from the measurements of Δt and δtP . To further constrain the crustal

thickness and crustal velocity, we add the Sp and SP_{mp} phase arrivals (sections 2.2.4 & 2.2.5)

2.2.3 Determining when to correct for sedimentary layers

Applying a sediment removal filter and correcting phase arrival times on the Ps receiver function may introduce error if the data do not exhibit pronounced sediment reverberations. To avoid this, a set of criteria based on quantitative metrics is defined to decide whether the sediment removal filter and arrival time corrections should be applied.

The first criterion that needs to be satisfied for the sediment removal filter to be applied is that the variance of the differences between the sediment removed Ps RF and the original Ps RF (v_1) be larger than the variance of the differences between the autocorrelation of the original Ps RF and the resonance filter (v_2). If v_1 is larger than v_2 , the resonance filter fits the autocorrelation of the receiver function well (small v_2) and applying the resonance removal filter changes the resulting RF (large v_1). The second criterion is that the amplitude of the PP_{bs} arrival, $f(\delta tP)$, is at least 30 percent of the largest amplitude signal in the receiver function. Alternatively, the sediment removed receiver functions are used if the direct sediment conversion is 90 percent of the largest amplitude signal in the receiver function, regardless of v_1 or v_2 . If the direct sediment conversion is small, the sediment reverberations should not mask deeper arrivals, but if the direct sediment conversion is very large, then reverberations may be overprint deeper signal. If these criteria are met, then the sediment removal

filter is applied and delay time corrected to create the SRTC H- κ - V_p stack. By applying a single set of criteria, SRTC H- κ - V_p stacking can be automated for stations across various tectonic/geologic settings without having to decide *a priori* whether the station is significantly affected by sediment.

2.2.4 Sp receiver functions in H- κ - V_p stacks

To further constrain crustal properties beneath a seismic station, it is helpful to add the complimentary Sp receiver function. Like Ps RFs, S-to-p converted waves reverberate between the Moho and the free surface, producing multiples. The S-to-p conversion across the Moho occurs further from the station (*Figure 2.7*) and the S wave contains lower frequencies than the P wave and so Sp RFs are not used as often as the Ps RFs to constrain crustal properties. However, the Sp phase arrives before the direct S wave arrival and is not directly affected by sedimentary layers as the Ps phase. While the direct S_{mp} conversion across the Moho and its reverberations have been used to constrain crustal thickness and velocity (*Rychert and Harmon, 2016*), we find that signals from sediment multiples arriving immediately after the main S phase are difficult to isolate from source-time function complexity and distinguish from the noise; therefore, we choose to only use the direct Sp phase to constrain the crustal thickness.

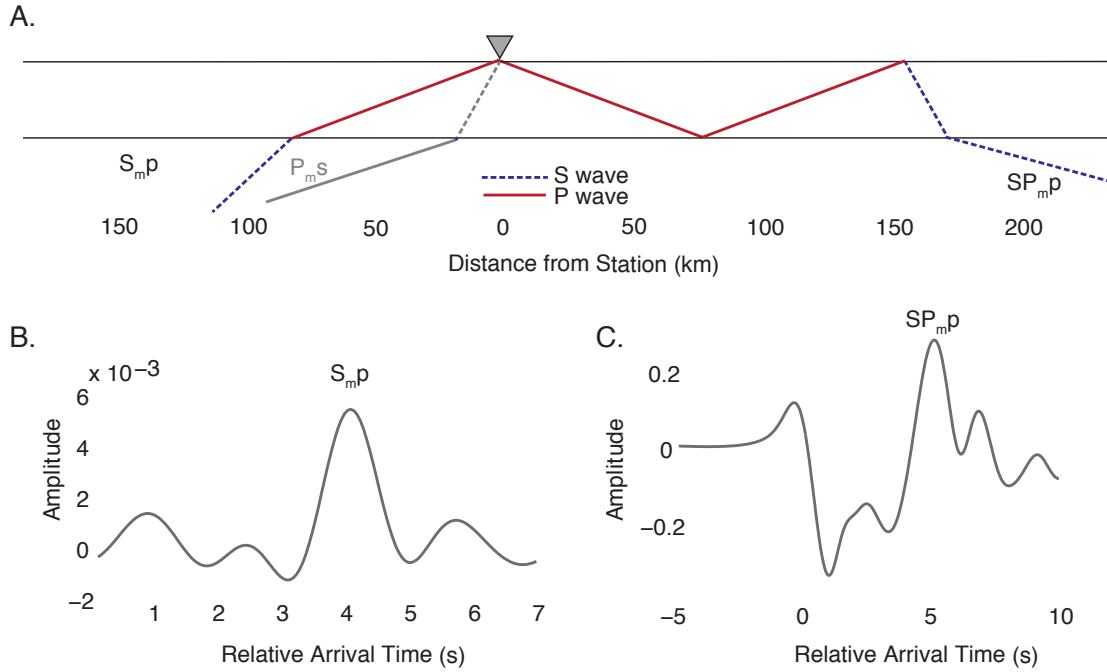


Figure 2.7– *A.* Ray-path geometry of S to p converted phases across the Moho at 30 km depth calculated for an incident plane wave of 0.14 s/km and the post critical P wave reflection across the 30 km deep Moho (SP_mp) with incident plane wave of 0.1486 s/km. The Ps conversions from the Moho are plotted for comparison (gray line). *B.* Synthetic receiver function of the S-to-p phases converted across the Moho. Time is relative to the direct S arrival (positive values indicate earlier arrivals). *C.* Synthetic receiver function of the Hilbert-transformed post-critical P phase at the Moho. Time is relative to the direct S arrival (positive values indicate later arrivals). Crustal $V_P = 6.3$ km/s, $V_S = 3.7$ km/s, while mantle $V_P = 8$ km/s and $V_S = 4.6$ km/s.

To compare, and eventually combine, the Sp and Ps RFs the Sp RFs polarity is flipped so that a conversion across an impedance increase with depth corresponds to a positive phase, and then the Sp RF is time-reversed so S_mp phase arrives after the direct S. In this convention, the relative arrival time of the direct Sp conversion depends on the crustal thickness (H), crustal velocity (V_P and V_S), and S-wave ray parameter (p_{Sp}) in exactly the same way as Ps arrival time (eq. 1). The sum of all Sp receiver functions (N_{Sp}) computed at a station, $f_j'(t)$, and evaluated at the expected

arrival times for a range of crustal thickness (H), V_P/V_S ratios (κ), and average crustal V_P yields the expression analogous to *eq. (2.4)*:

$$(2.9) \quad s_{S_{mp}}(H, \kappa, V_P) = \sum_{j=1}^{N_{Sp}} f'_j(t_{S_{mp}})$$

If the Ps RFs indicate the presence of a sufficiently thick shallow layer (see section 2.2.3), the delay time of the converted P-wave in sediment compared to the direct S-wave is estimated to be δt (same as the P_bS time above) by assuming vertical incidence in the sediment and correct for it when constructing the Sp H- κ - V_P stack:

$$(2.10) \quad s_{S_{mp}}(H, \kappa, V_P) = \sum_{j=1}^{N_{Sp}} f'_j(t_{S_{mp}} + \Delta t - \delta tP)$$

Stacking the direct S_{mp} conversions on their own does not result in a maximum at a single, optimal H- κ - V_P combination; rather, $s_{S_{mp}}$ yields a range of possible H, κ , and V_P values. This is nevertheless beneficial because traditional Ps RF H- κ stacks with noisy data can be characterized by spurious maxima arising from constructive interference of noise or multiples that do not correspond to correct crustal H and κ values. Therefore, in addition to helping to constrain V_P , the strength of including the complementary Sp stack is that it significantly restricts the range of possible maxima, especially regarding crustal thickness (H). To further improve the ability to determine crustal thickness, V_P/V_S , and especially average crustal V_P , constraints from the SP_{mp} conversion are incorporated.

2.2.5 SsPmp receiver functions in H- κ - V_p stacks

The SP_mp phase provides constraints complementary to those from Sp and Ps RFs since it is sensitive to crustal thickness and average crustal V_p . The SP_mp phase involves a post-critical reflection of the P-wave at the Moho which is produced when ray parameters of incoming teleseismic S-waves are sufficiently large, and are greater than the maximum ray parameters used in constructing typical Sp stacks (e.g. *Wilson et al., 2006*). As a result, the horizontal location of the conversion point is far away from the station (> 50 km) (**Figure 2.7A**). The raw SP_mp waveform contains complexity due to the earthquake source-time function and source-side propagation effects. Therefore, just as for the Sp RF, these source effects are suppressed by deconvolving the parent (S) component from the daughter component (P) and computing an SP_mp receiver function. Unlike the direct Sp phase, SP_mp arrives after the direct S-wave, and so it can be combined with the Ps RF without being flipped in time. Despite arriving after the direct S-wave, the SP_mp RF is less sensitive to sediment reverberations (*Parker et al. 2016*). In regions where the assumed average crustal V_p is inaccurate and sedimentary layers may mask Moho signals on the Ps RF, the large amplitude SP_mp phase has proven useful in obtaining crustal thickness estimates (e.g. *Langston, 1996; Owens and Zandt, 1997; Yu et al., 2012; Parker et al., 2013; Yu et al., 2013; Tian et al., 2015; Parker et al., 2016; Kang et al., 2016*).

The SP_mp RF should not be directly incorporated into a H- κ - V_p stack because the post-critical reflection produces phase shifts that result in waveform distortion. We remove these distortions by computing the envelope of each SP_mp receiver function

(*Bracewell, 1968*). The expected phase arrival time of the SP_mp conversion relative to the direct S wave arrival depends only on H , V_P , and the ray parameter, p_{SSPmp} :

$$(2.11) \quad t_{SSPmp} = 2H \sqrt{V_P^{-2} - p_{SSPmp}^2}$$

Because the post critical P wave reflection occurs for events within a small range of epicentral distances, fewer data are available for SP_mp RFs than for Ps and Sp RFs. So that SPmp arrives at positive lag times, we phase weight stack the SP_mp RFs in ray parameter bins, and require at least 3 events in each bin (*Schimmel and Paulssen, 1997*), yielding a set of $f_j''(t)$. As with Sp and Ps RFs, a H- κ - V_P stack can be constructed by summing all available $f_j''(t)$ (N_P) at expected arrival times, t_{SSPmp} **eq. (11)**, for a range of H, κ , and V_P values:

$$(2.12) \quad s_{SSPmp}(H, \kappa, V_P) = \sum_{j=1}^{N_P} f_j''(t_{SSPmp})$$

Note that this stack is identical for all values of κ . If the analysis of Ps receiver functions indicates that sediment corrections are necessary (see section 2.2.3), we correct the SP_mp travel time by again assuming vertical incidence within the sedimentary layer. The time-corrected H- κ - V_P stack is given by:

$$(2.13) \quad s_{SSPmp}(H, \kappa, V_P) = \sum_{j=1}^{N_P} f_j''(t_{SSPmp} + 2\delta tP - \Delta t)$$

The additional constraints provided by the SP_{mp} RFs, when combined with Ps and Sp stacks, will allow us to constrain V_p , as well as H and κ beneath a seismic station even when thick sediment layers are present.

2.2.6 Calculating combined SRTC H- κ - V_p stacks with error

The final step in creating the SRTC H- κ - V_p triple stack is to determine the best method to combine the Ps, Sp and SP_{mp} SRTC H- κ - V_p stacks and quantify error. Each stack is normalized by its absolute maximum, and the triple stacks (Ps, Sp, and SP_{mp}) are combined by adding them to create a joint SRTC H- κ - V_p triple-stack:

$$(2.14) \quad s(H, \kappa, V_p) = \overline{sPs(H, \kappa, V_p)} + \overline{sSp(H, \kappa, V_p)} + \overline{sSP_{mp}(H, \kappa, V_p)},$$

where the absolute maximum of the stack will be the best fit H, κ , and V_p crustal parameters to the Ps, Sp, and SP_{mp} RFs. This volumetric stack can be visually represented on three planes cutting through the maximum of the triple stack (see **Figure 2.8**).

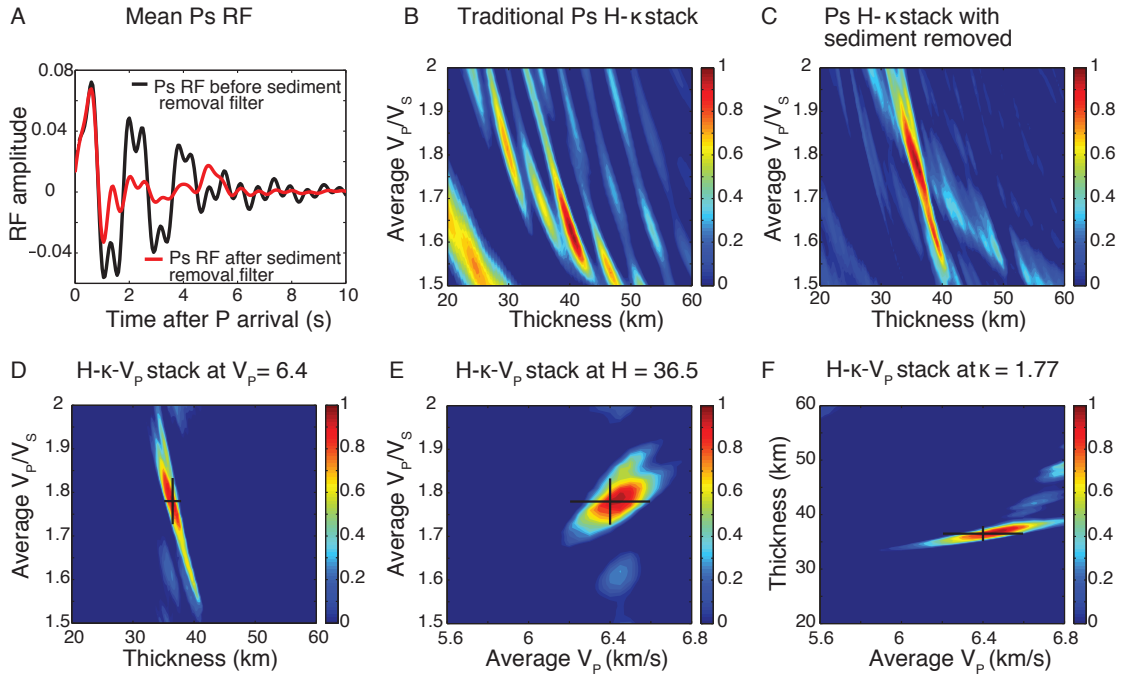


Figure 2.8— SRTC H- κ - V_p stacking of synthetic receiver functions, where negative values in the stack are clipped. Input model has a 0.5 km thick sedimentary layer, V_p of 2 km/s, and $\kappa = 2.3$, and a Moho at 37 km depth with crustal $V_p = 6.3$, and $\kappa = 1.76$. **A.** The mean Ps receiver function before (black) and after (red) the sediment removal filter is applied. **B.** Ps H- κ stack at assumed $V_p = 6.3$ shows no clear maxima. **C.** The Ps H- κ stack after the sediment removal filter and time correction is applied shows a clear maximum. **D, E, & F.** Three cross-sections through the maximum of the H- κ - V_p triple stack; black cross hairs denote 1σ error bars.

To quantify the uncertainty of the estimates of optimal H, κ , V_p values, we look at the spread of the stack amplitude along its three axes. We interpret stack amplitude as proportional to log-likelihood. Therefore, ignoring higher order terms of the Taylor series expansion of the stack around the maximum, the curvature of the stack can be related to the posterior covariance matrix representing uncertainty of our parameter estimates. Specifically, the posterior covariance matrix is given by the negative inverse of the second-derivatives matrix evaluated at the triple stack maximum (Sivia, 2006):

$$(2.15) \quad \begin{bmatrix} \sigma_H^2 & \sigma_{HV_P}^2 & \sigma_{H\kappa}^2 \\ \sigma_{HV_P}^2 & \sigma_{V_P}^2 & \sigma_{V_P\kappa}^2 \\ \sigma_{H\kappa}^2 & \sigma_{V_P\kappa}^2 & \sigma_\kappa^2 \end{bmatrix} = - \begin{bmatrix} \frac{d^2s}{dH^2} & \frac{d^2s}{dHdV_P} & \frac{d^2s}{dHd\kappa} \\ \frac{d^2s}{dHdV_P} & \frac{d^2s}{dV_P^2} & \frac{d^2s}{dV_Pd\kappa} \\ \frac{d^2s}{dHd\kappa} & \frac{d^2s}{dV_Pd\kappa} & \frac{d^2s}{d\kappa^2} \end{bmatrix}^{-1}$$

Where s is the triple stack (from **eq. 2.14**) amplitude at the optimal H, κ, V_P values. The original paper introducing the H- κ stacking method (*Zhu and Kanamori, 2000*) proposed calculating the uncertainty of H and κ estimates made from the stack by dividing stack variance by the second derivative for H and κ , which ignores the co-variance terms. This corresponds to computing the uncertainty on each parameter at the preferred value of the other parameter(s). Due to tradeoffs among parameters captured in the off-diagonal terms of the covariance matrix, however, this estimate is a lower bound on the true uncertainty. The uncertainty estimates represented by the variances in **eq. (2.15)**, on the other hand, are a more appropriate measure of uncertainty since they capture additional uncertainty arising from our ignorance about the true values of the other parameters. It should be noted that even for traditional H- κ stacks, the error should be calculated including the co-variance terms.

2.3 Receiver Function Data for H- κ - V_P Stacks

We evaluate the effectiveness of the H- κ - V_P stacking method for constraining crustal V_P , V_P/V_S and thickness using synthetic receiver functions as well as data recorded at three EarthScope Transportable Array (TA) stations, which span various geologic and

tectonic settings, but all suffer from shallow layer contamination. The stations are: (1) B30A located in Edmore, ND on the eastern edge of the Williston basin; (2) 448A in Bay Minette, AL located within the Mississippi embayment; and (3) U60A in Pendleton, NC within the Atlantic coastal plain (ACP) **Figure 2.9**.

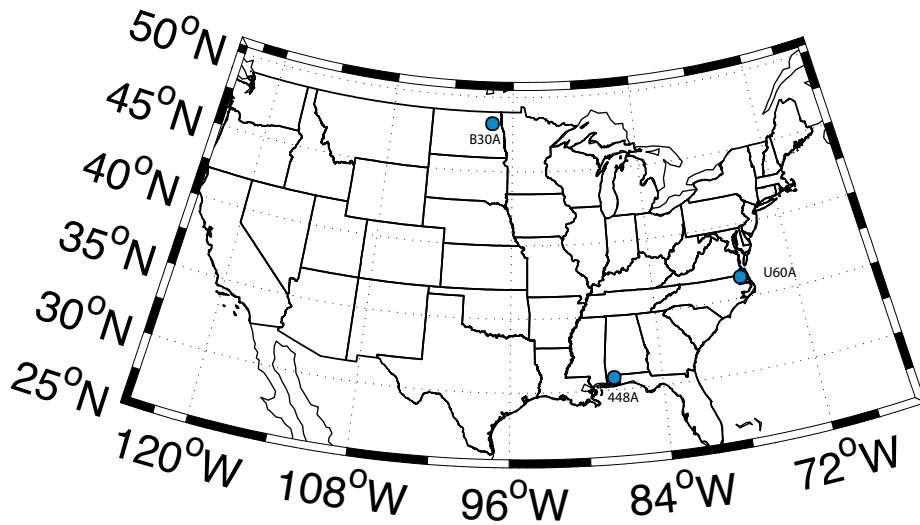


Figure 2.9 -Locations of USArray TA stations B30A, U60A, and 448A used in this study shown as teal circles.

To calculate Ps RFs for each station, we obtain 300 second three-component waveforms around the P arrival time for events with $M_w > 5.6$ at epicentral distances between 30 and 90 degrees from the station. (*Abt et al., 2010*). Sp receiver functions are further restricted to events with epicentral distances between 55 and 90 degrees from the station that occur at depths less than 300 km (*Wilson et al., 2006*). SP_{mp} waveforms are restricted to events with epicentral distances between 30 and 50 degrees (*Yu et al., 2013*). A summary of the number of Ps, Sp and SP_{mp} events, along with the slowness range for each station is shown in **Table 2.1**.

Table 2.1-Number of events and slowness range for each seismic station used in this study

Station	Geologic Setting	# of Ps RF events	Ps slowness range (ρ)	# of Sp RF events	Sp slowness range (ρ)	# of SP _{mp} RF events	SP _{mp} slowness range (ρ)
B30A	Williston Basin, MT	167	0.0475-0.774	49	0.1002-0.1196	37	0.1276-0.1411
U60A	Atlantic Coastal Plain, NC	120	0.0487-0.0772	113	0.1001-0.1201	8	0.1262-0.1409
448A	Mississippi Embay., MS	36	0.0504-0.773	81	0.1006-0.1201	8	0.1293-0.1339

The automatic quality-control procedure is detailed in Abt et al. (2010). In this study, we culled the dataset to have a minimum Z-to-R cross correlation of 0.3, and a maximum difference of 25s between the automatically determined arrival time and prediction for ak135. The minimum signal to noise ratio is set to 0 for Ps and Sp receiver functions, while for SP_{mp} RFs we require that the Hilbert transform of the SP_{mp} arrival is greater than 1.2 of the S-wave arrival amplitude. We follow the Abt et al. (2010) procedure for calculating RFs, using a free-surface transform matrix (Kennett, 1991) and finding the surface velocity that minimizes the parent amplitude (P for Ps and S for Sp) on the daughter component to project the waveforms onto the P-SV-SH system, pick the arrival times, and apply a fourth order Butterworth band-pass filter to waveforms of 0.03-1 Hz and 0.03-4 Hz for Ps, and 0.03-0.5 Hz for both Sp and SP_{mp}. We then use the iterative time domain deconvolution with Gaussian half-amplitude half-width of about 0.12 s 0.5 s and 1 s for 4 Hz, 1 Hz, and 0.5 Hz respectively. to calculate the receiver functions (Ligorria and Ammon, 1999).

To calculate synthetic receiver functions, the synthetic seismograms are generated using the flat-layer reflectivity algorithm ANIREC (*Levin and Park, 1997*) for a range of slowness and backazimuths. Then a fourth order Butterworth band-pass filter is applied to waveforms (0.03-1 Hz and 0.03-4 Hz for Ps, and 0.03-0.5 Hz for both Sp and SP_{mp}) and the parent waveform is deconvolved from the daughter waveform using the Wiener frequency deconvolution (*Wiener, 1964; Langston 1979*).

We calculate the triple stacks over a range of possible crustal H, κ and V_p , values where H ranges from 20 to 60 km, κ ranges from 1.5 to 2, and V_p ranges from 5.6 to 6.8 km/s.

2.4 Results and Observations from the SRTC H- κ - V_p Method

We show the results of SRTC H- κ - V_p stacking applied to synthetic waveforms and three EarthScope TA stations with a low velocity sediment layer. We compare the estimates of crustal thickness before and after the SRTC H- κ - V_p stacking method is used and also to crustal thickness estimates in these regions from previous studies.

Because time corrections are made to each phase to account for the slow sedimentary layer, the average crustal thickness, V_p/V_s , and V_p at each station will correspond to the crust below the sediment. To determine the Moho depth from our study and compare with other studies, the thickness of the sediment should be added to the crustal thickness estimates from the SRTC H- κ - V_p stacks. We estimate the sediment thickness at each station using the measurements of Δt and δtP and assuming a

relationship of V_P and V_S relationship from the mud-line equation (Brocher *et al.*, 2005). We find that the sediment thickness agrees within 0.1 km of the shallowest sediment layer from the CRUST 1.0 model (Laske *et al.*, 2013). We interpret this shallowest layer of sediment as the unconsolidated sediment thickness at each station. At station TA B30A, we find a sediment thickness of 0.3 km, which agrees with estimates of 0.3-0.5 from multiple datasets (AAPG, 1967; Laske *et al.*, 2013). At station U60A we find a sediment thickness of 0.78, similar to the estimate from CRUST 1.0 of 0.9 km (Laske *et al.*, 2013), but much thicker than the estimate of 0.3 km interpolated from drill hole data using Bouger gravity maps (Lawrence and Hoffman, 1993). This discrepancy in sediment thickness values at U60A could arise from differences in interpreting what constitutes the shallowest sedimentary layer; alternatively, they could be due to differences in the velocity used to determine the thickness of the sedimentary layer. Finally, at station TA 448A we calculate a sediment thickness to be 0.46 km, which lies in between the estimates of 0.6 km from CRUST 1.0 (Laske *et al.*, 2013) and 0.339 for nearby station Y46A from horizontal to vertical ambient noise measurements (Langston and Horton, 2014). Tighter constraints and better uncertainty estimates can be achieved by either using higher frequency receiver functions (*e.g.* Leahy, 2012) or by stacking receiver functions for predicted sedimentary multiples (*e.g.* Yeck *et al.*, 2013). However, since the goal of this study is accurate estimates of total crustal thickness, the rough estimation of sediment thickness from the travel time is sufficient, as the uncertainty of the resulting crustal thickness estimates are smaller than those achievable with the H- κ - V_P stacking method.

2.4.1 SRTC H- κ - V_p stacking with synthetic waveforms

The model used for calculating the synthetic waveforms has a sedimentary layer of thickness (H) of 0.5 km, V_p of 2.3 km/s, and κ of 2.1 underlain by 36.5 km thick layer more representative of crystalline rock, with $V_p = 6.4$ km/s and $\kappa = 1.76$. Before carrying out H- κ - V_p stacking, how the application of the sediment removal filter affects the appearance of mean Ps RFs relative to the results of traditional H- κ stacking is compared. (*Figure 2.8 A-C*).

The mean Ps RF computed from the synthetic waveforms is dominated by large amplitude sediment reverberations (black line, *Figure 2.8A*). After the sediment reverberation removal filter is estimated and applied (*eq. 2.6*), the mean Ps RF shows one clear arrival at ~ 5 s (red line, *Figure 2.8A*) corresponding to the Ps conversion across the Moho, but which was masked by sediment reverberations before the application of the resonance removal filter.

Ps RFs computed with and without the resonance removal filter yield dramatically different results when used for traditional and SRTC H- κ stacking, respectively. To illustrate this, traditional H- κ stacks computed using the original Ps RFs are plotted (black line - *Figure 2.8A*) and compared to SRTC H- κ stacks computed using the resonance removed Ps RFs (red line - *Figure 2.8A*) at an assumed crustal V_p of 6.3 km/s. While the traditional Ps H- κ stack shows no clear Moho maximum (*Figure 2.8B*), one might be interpreted at $H = 42$ km and $\kappa = 1.63$ (*Figure 2.8B*). SRTC H- κ stacks, on the other hand, show a much stronger maximum at $H = 37$ km and $\kappa = 1.79$

(**Figure 2.8C**), which is nearly identical to the model values used to calculate the synthetic waveforms.

Having validated that the SRTC H- κ stacks are much better at resolving the input crustal structure in the presence of a shallow low-velocity layer, complementary Sp RFs are added, as sediment reverberations will not contaminate them. If the sediment removal filter is not successful in removing all of the amplitude or there are multiple basin layers with phase arrivals overprinting Moho arrivals, the Sp H- κ - V_p stacks can help clarify crustal thickness. Finally, the SP_{mP} RFs are introduced to remove the dependence on an assumed average crustal V_p and better constrain the crustal thickness (H). A combined SRTC H- κ - V_p stack is computed (*eq. 2.14*) for the same input model by adding the weighted time-corrected Sp (*eq. 2.10*) and SP_{mP} (*eq. 2.13*) RFs to the SRTC Ps stacks, **Figure 2.8**. Unlike H- κ stacking, which can be fully visualized on a 2D contour plot, the H- κ - V_p stack varies in amplitude along three axes; therefore, slices through the stack volume are shown. In **Figure 2.8D**, when the Sp and SP_{mP} RFs are added, again there is one clear maximum in the SRTC H- κ - V_p stack (**Figure 2.8D-E**). The crustal parameters are $H = 41.25 \pm 2$ km, $V_p = 6.3 \pm 0.3$ km/s, and $\kappa = 1.75 \pm 0.09$.

To investigate the dependence of the SRTC H- κ - V_p stacking results on noise, this analysis is repeated for increasing amounts of white noise (filtered to have similar frequency content as typically encountered noise) with the maximum amplitude of the noise being 75% of the maximum amplitude of the daughter waveform (P for Sp and

S for Ps) added to all of the waveform components. The H , κ , and V_p values of the input model within error are still able to be resolved (**Figure 2.10**). This illustrates the ability of the SRTC H - κ - V_p stack to resolve the three crustal parameters from synthetic waveforms persists even under realistic noise levels. It also demonstrates that when a sedimentary layer is present, the sediment-removed, time-corrected Ps RFs, time-corrected Sp RFs, and time-corrected SP_{mp} are all needed to constrain parameters in the Ps H - κ - V_p stacks. Additionally, the sediment thickness is roughly estimated to be $H = 0.508$ km, which is consistent with the input sediment thickness value. Therefore, both the sediment and the crustal structure of the synthetic model are successfully retrieved using the SRTC H - κ - V_p stacking method.

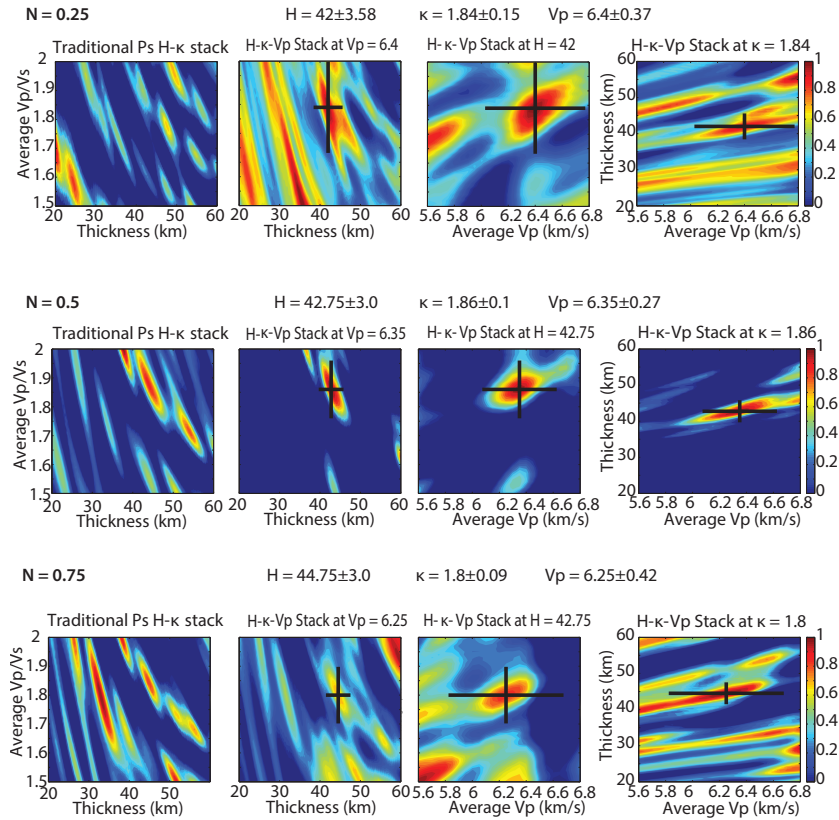


Figure 2.10– H- κ - V_p stacks generated from synthetic waveforms with increasing noise levels. The input model has a sedimentary layer 0.5 km thick, V_p of 2.3 km/s and $\kappa = 2.3$, a Moho at 42.5 km depth with crustal $V_p = 6.3$ km/s, and a κ of 1.76. White noise is filtered to have similar frequency content as typically encountered noise, with amplitude up to three-quarters of the maximum of the daughter waveform (s for Ps; p for Sp and SPmp). At increased noise levels, we are still able to constrain crustal H, κ , and V_p within error.

2.4.2 TA station B30A: eastern Williston Basin

Having validated the SRTC H- κ - V_p stacking method on synthetics, we apply it to data recorded at a station where reverberations from shallow sediments can be expected. EasrthScope Temporary Array (TA) station B30A lies on the eastern edge of the Williston basin in northeastern Montana. The Ps RFs were calculated using the best-

fit rotation velocities of $V_P = 5.3$ km/s and $V_S = 2.9$ km/s. The measurement of δtP is made on the 4Hz Ps RFs (**Figure 2.11**) and is 0.6 s. The measurement of Δt at station B30A is 1.17 s and is measured from the autocorrelation of the 1Hz Ps RF. However, there no difference between the 1Hz and 4Hz RF for this measurement (**Figure 2.11**). At station B30A, the arrival time of Δt does not depend on event location or frequency of autocorrelated RFs.

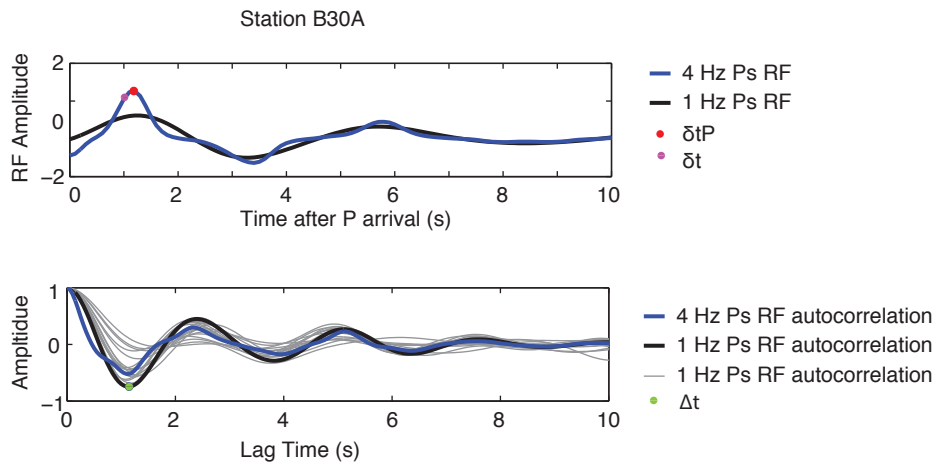


Figure 2.10– (Top) Mean 4 Hz (blue) and 1Hz (black) Ps RF for station B30A shown with picked arrival time for δtP and δt shown in the red and magenta circles respectively. The arrival time of the two phases (P_b s and PP_b s) likely overlap at this station. (Bottom) Autocorrelation from the mean 4Hz (blue) and 1Hz (black) RF with picked arrival time for Δt . Autocorrelation of a random subset of individual RFs are shown as gray lines in the background.

The Ps RF before the sediment removal filter is dominated by large amplitude, oscillatory signals due to S-wave reverberations within the low velocity shallow layer (black line, **Figure 2.12A**, **Figure 2.13**). From the measurements of Δt and δtP , sediment thickness is estimated to be 0.37 km. The traditional Ps H- κ stack has a maximum at $H = 28.5$ km and $\kappa = 1.62$ (**Figure 2.12B**), which would suggest anomalously thin crust and a crustal V_P/V_S representative of quartz sandstone (>57%

SiO₂) to the base of the crust (*Christensen, 1996*). After the sediment removal filter is applied to the Ps RFs, the amplitude of the receiver function decreases with increasing lag-time (red line – *Figure 2.12A*), and the oscillatory behavior is suppressed. The SRTC Ps H- κ stack shows a stronger maximum, indicative of a better fit to the direct conversions and multiples, which occurs at a greater depth, $H = 40$ km and a higher V_p/V_s , $\kappa = 1.77$ (*Figure 2.12C*). When complimentary Sp and SP_{mp} RFs are added to create a SRTC H- κ - V_p stack, the maximum occurs at $H = 44.25 \pm 2.63$ km, $V_p = 6.75 \pm 0.43$ km/s, and $\kappa = 1.76 \pm 0.09$. (*Figure 2.12D-E*). By applying the SRTC H- κ - V_p triple stacking method to this station, a thicker continental crust is found with a more realistic average V_p/V_s – consistent with a generally more mafic crustal composition (*e.g.* diorite or amphibolite per *Christensen, 1996*) compared to traditional H- κ stacking, and estimate average crustal V_p instead of having to assume it *a priori*.

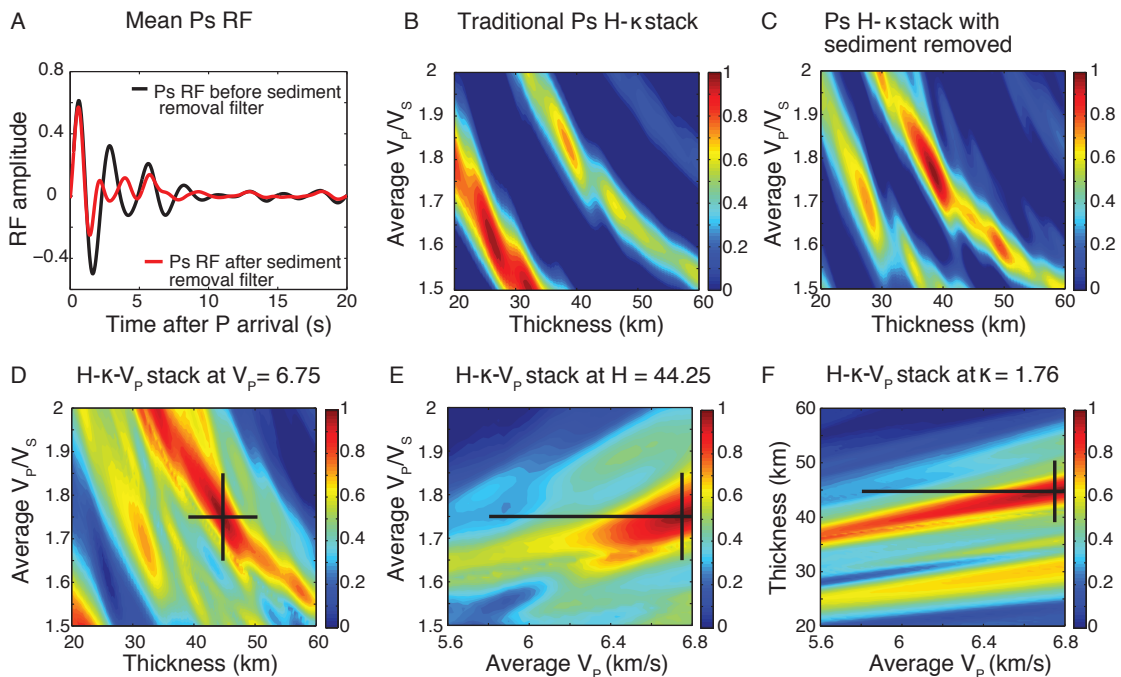


Figure 2.12 – SRTC H- κ - V_p stacking of B30A receiver functions, where negative values in the stack are clipped. Station B30A is located on the eastern edge of the Williston Basin in Montana. **A.** The mean Ps receiver function before (black) and after (red) the sediment removal filter is applied. **B.** Ps H- κ stack at assumed $V_p = 6.3$ km/s shows a maximum of the stack at $H = 28.5$ km and $\kappa = 1.62$. **C.** The Ps H- κ stack after the sediment removal filter and time correction is applied; the stack maximum now corresponds to larger H and κ values **D, E, & F** Three cross-sections through the maximum of the H- κ - V_p triple stack; black cross-hairs denote 1σ error bars.

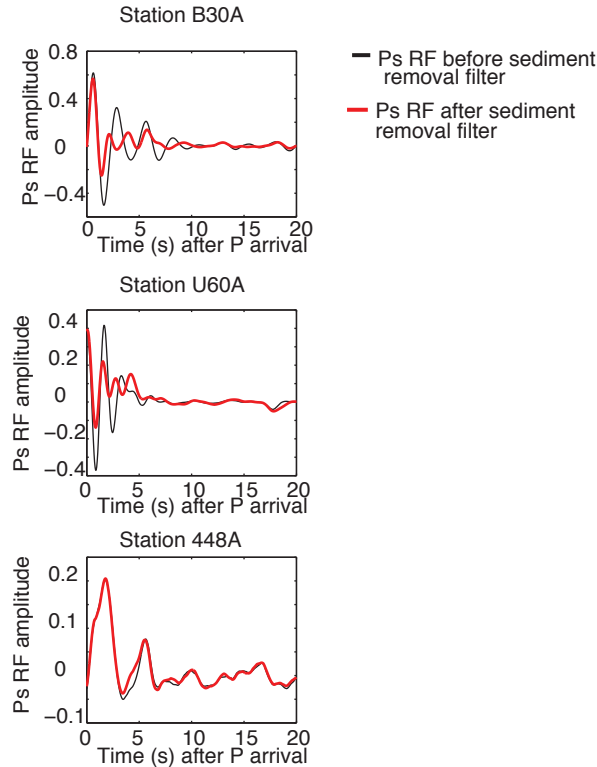


Figure 2.13 - 1Hz Ps receiver functions before (black) and after (red) sediment removal filter is applied plotted from 0 to 20 seconds after the direct P arrival. (Top) station B30A (Middle) station U60A (Bottom) station 448A.

Previous studies near the location of TA station B30A estimate the Moho depth to be between 38 and 45 km (Cook et al., 1981; Langston, 1994; Chulick and Mooney, 2002). Those values agree within error with our estimate for crustal thickness of 44.25 ± 2.63 km (or a Moho depth of 44.72 km). However, the EarthScope Automated Receiver Survey (EARS), which uses a modified version of the traditional H- κ stack,

finds a much lower estimate for the crustal thickness of 30 ± 5.8 km (Crotwell and Owens, 2005). The V_p/V_s (κ) from the SRTC H- κ - V_p triple stack is 1.76 ± 0.09 , while the EARS estimate of κ is much lower at 1.65 ± 0.07 . The likely explanation for the inconsistency between these two results is that by implementing the sediment removal filter and adding Sp and SP_mp stacks, the amplitude of the shallower maximum is reduced (**Figure 2.12B**) and the deeper maximum is highlighted. (**Figure 2.12C-F**). The average crustal P-wave velocity (V_p) of 6.75 ± 0.43 km/s is consistent within error of previous results where the velocity is between 6.53 and 6.6 km/s (Langston 1994; Chulick and Mooney, 2002; Laske et al., 2013) and agrees with the higher V_s found under the Williston Basin (Schulte-Pelkum et al. 2017). The consistency of the three crustal parameters with previous studies gives us confidence that the H- κ - V_p triple stacking method is valid in this region.

2.4.3 TA station U60A: Atlantic Coastal Plain

Due to shallow sedimentary layers, one particularly challenging region for receiver function interpretation has been the Atlantic coastal plain. EarthScope TA station U60A lies on the eastern North Carolina portion of the Atlantic coastal plain. The Ps RFs were calculated using the best-fit rotation velocities of $V_p = 6$ km/s and $V_s = 3.4$ km/s. The measurement of δtP is made on the 4Hz Ps RFs (**Figure 2.14, Figure 2.13**) and is 0.2 s. The measurement of Δt at station U60A is 0.8 s and is measured from the autocorrelation of the 1Hz Ps RF. However, there is slight difference between the 1Hz and 4Hz RF for this measurement (**Figure 2.14**). The Ps RF before the sediment removal filter for station U60A has a large amplitude oscillatory signal

between at lag times <5 seconds due to shallow layer reverberations (black line, **Figure 2.15**). From the measurements of Δt and δtP , the sediment thickness is estimated to be 0.8 km and calculate a sediment removal filter. When the filter is applied to the Ps RFs, the amplitude of the early arriving oscillatory phases is reduced and a peak appears in the sediment removed Ps RF (red line, **Figure 2.15A**) at approximately 4 seconds. In the traditional Ps H- κ stack calculated with the Ps RFs before the resonance removal is applied, no clear maxima appear deeper than 20 km (**Figure 2.15B**), and no realistic constraint on crustal thickness and V_p/V_s can be placed. However, when the SRTC Ps H- κ stack calculated with the resonance removed Ps RFs, a deeper maximum becomes clear at $H = 30.5$ km and $\kappa = 164$. When the time-corrected Sp and SP_mp RFs are incorporated in the SRTC H-k-V_p triple stack, a maximum is found at $H = 31.75 \pm 2.28$ km, $V_p = 6.0 \pm 0.38$ km/s, and $\kappa = 1.65 \pm 0.09$ (**Figure 2.15D-E**), which suggests thinner and slower average crust than that present beneath the Williston basin., the sediment removal filter and the SRTC H- κ -V_p triple stack allows meaningful constraints to be placed on average crustal properties. Even when the sediment multiples completely mask the crustal signal in the Ps RF; the SRTC H- κ -V_p stack finds a reasonable maximum associated with the crust where none existed in the traditional H- κ stack.

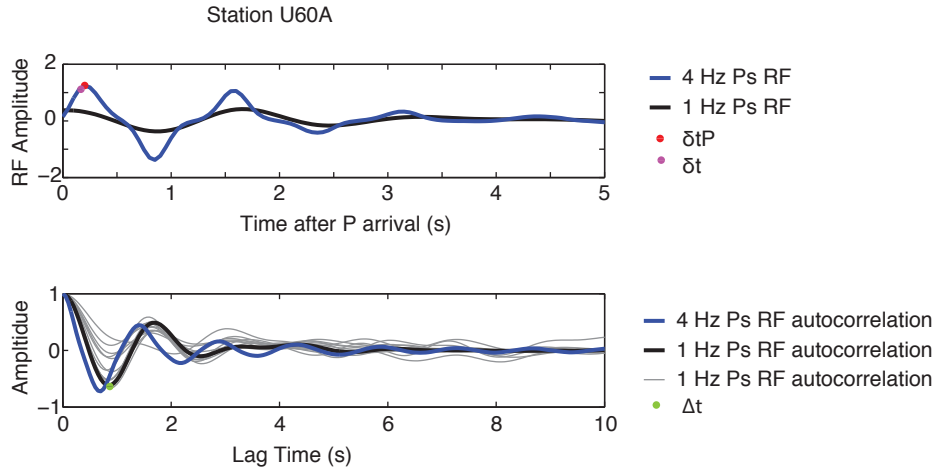


Figure 2.11– (Top) Mean 4 Hz (blue) and 1 Hz (black) Ps RF for station U60A shown with picked arrival time for δt_P and δt shown in the red and magenta circles respectively. The arrival time of the two phases (P_b s and PP_b s) likely overlap at this station. (Bottom) Autocorrelation from the mean 4 Hz (blue) and 1 Hz (black) RF with picked arrival time for Δt . Autocorrelation of a random subset of individual RFs are shown as gray lines in the background. At station B30A, the arrival time of Δt does not depend on event location and only changes slightly with frequency of autocorrelated RFs.

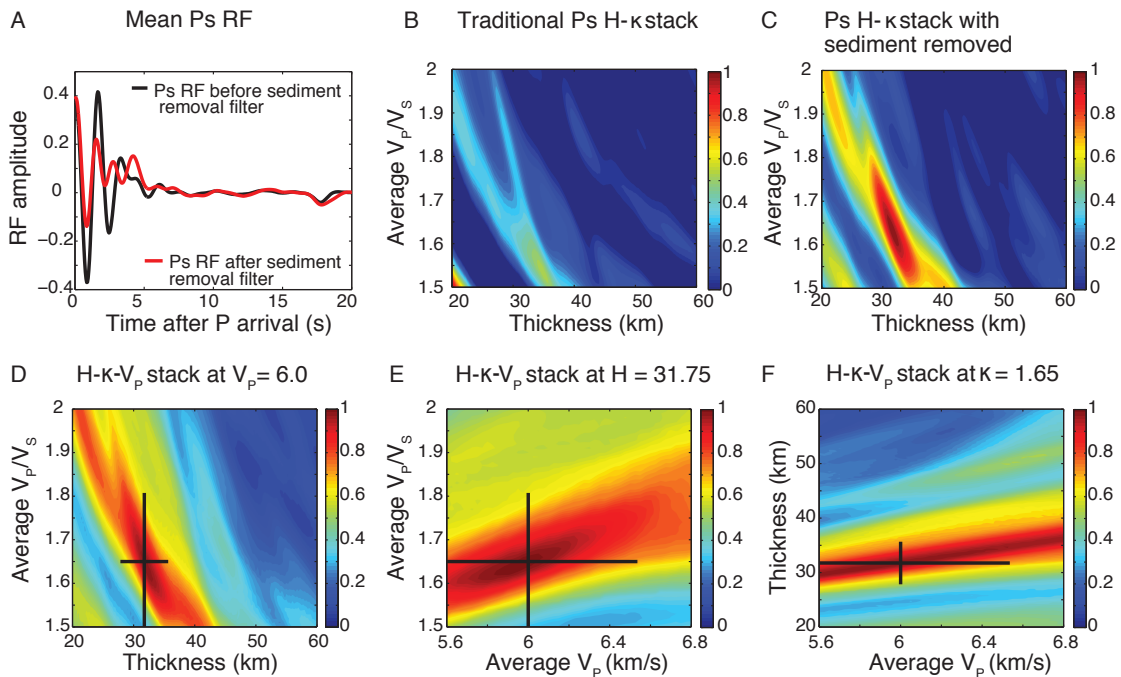


Figure 2.12– SRTC H- κ - V_p stacking of U60A receiver functions, where negative values in the stack are clipped. Station U60A is located on the Atlantic Coastal Plain in North Carolina. **A.** The mean Ps receiver function before (black) and after (red) the sediment removal filter is applied. **B.** Ps H- κ stack at assumed $V_p = 6.3$ km/s shows no clear maxima. **C.** The Ps H- κ stack after the sediment removal filter and time correction is applied has a clear maximum. **D, E, & F.** Three cross-sections through the maximum of the H- κ - V_p triple stack; black cross-hairs denote 1σ error bars.

Most regional and active source studies of the Atlantic coastal plain that directly interpret their results in terms of the geology have taken place further south than TA U60A. There is a slight disagreement on the Moho depth in on the Atlantic coastal plain, where the Moho depth may be shallower, between 30-35 km (*Cook et al., 1981; Chulick and Mooney, 2002; Li and Fischer., 2002; Abt et al., 2010; Laske et al., 2013; Cook, 2016; Parker et al., 2016*), or deeper, between 35-40 km (*Crotwell and Owens, 2005; Lynner and Porrit, 2017*). We find the crustal thickness at station U60A to be thin 31.75 ± 3.52 km (a shallow 32.55 km Moho depth), agreeing with the first set of studies. We find a low with a V_p/V_s (κ) of 1.65 ± 0.17 which agrees within error other estimates of V_p/V_s in the Atlantic coastal plain between 1.69-1.72 (*Musacchio et al., 1997; Parker et al. 2013*). . We also find a slow average crustal V_p of 6.0 ± 0.79 km/s compared to some studies which estimate that $V_p = 6.4-6.7$ km/s (*Laske et al., 2013*) but that agrees with previous studies, which suggest the crustal P-wave velocity is between 6.0 and 6.5 km/s. (*Chulick and Mooney, 2002*) The large error of the V_p estimate means that SRTC stacking at this station is not able to well resolve the average P-wave velocity at this station.

2.4.4 TA station 448A: Mississippi Embayment

The final station on which SRTC H- κ - V_p triple stacks calculated is EarthScope TA station 448A, located within the lower Mississippi embayment. The Ps RFs were calculated using the best-fit rotation velocities of $V_p = 5.9$ km/s and $V_s = 3.2$ km/s. The measurement of δt_P is made on the 4Hz Ps RFs (**Figure 2.16A**) and is 0.85 s. The measurement of Δt at station 448A is 2.2 s and is measured from the autocorrelation of the 1Hz Ps RF. However, while there is little difference between the 1Hz and 4Hz RF for this measurement (**Figure 2.16B**), we do see two negative peaks in the 4Hz autocorrelation, which implies that there are multiple sedimentary layers beneath station 448A. From the measurements of Δt and δt_P we estimate sediment thickness to be 0.46 km at this station. Unlike the two previous stations, applying the sediment removal filter at 448A does not significantly change the amplitude or arrival time of phases in the mean Ps RFs (red line compared to black line, **Figure 2.17A**, **Figure 2.13**). Therefore, one might expect that the traditional and SRTC Ps H- κ stacks would be similar to SRTC stacks. Nevertheless, this is not the case, as implementing the time corrections (**eq.7**) significantly changes the coherence in the SRTC H- κ stacks. While the traditional H- κ stack has a maximum at $H = 22$ km and $\kappa = 1.5$ (**Figure 2.17B**), the SRTC Ps H- κ stack (**Figure 2.17C**) has a deeper maximum at $H = 35.5$ km and $\kappa = 1.67$. While the sediment time corrections applied to the Ps RFs has a significant effect on improving the coherence, the multiple sediment layers that likely exist beneath station 448A may have sediment reverberations, which overprint Moho arrivals. Station 448A provides a good example on how the Sp and SP_mp RFs can improve the interpretation of crustal values

in a region with multiple sediment layers. When time-corrected Sp and SP_{mp} RFs are incorporated, the crustal properties corresponding to the maximum of the SRTC H- κ - V_P triple stack are $H = 39.5 \pm 2.39$ km, $V_P = 6.5 \pm 0.29$ km/s, and $\kappa = 1.65 \pm 0.08$. (**Figure 2.17D-E**). Station 448A highlights the importance of applying time corrections when calculating the H- κ stack in the presence of a low velocity shallow layer, even if the Ps RFs remain similar before and after the sediment removal filter is applied.

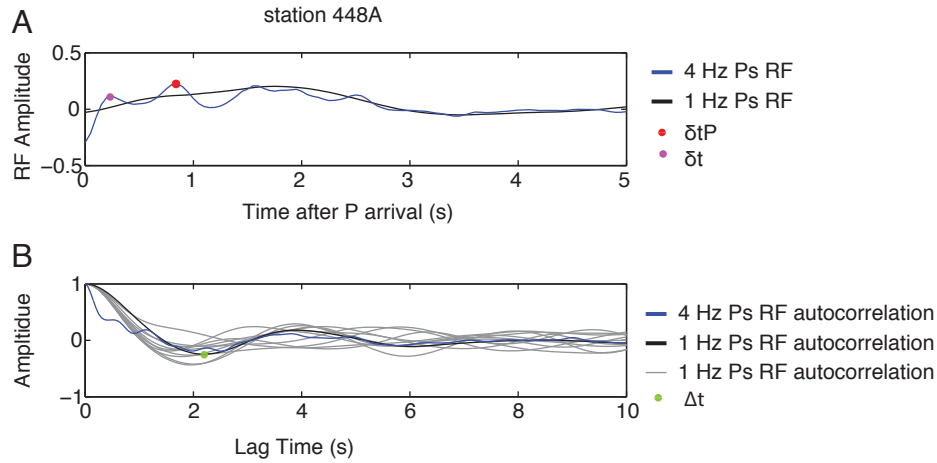


Figure 2.13– (Top) Mean 4 Hz (blue) and 1 Hz (black) Ps RF for station 448A shown with picked arrival time for δtP and δt shown in the red and magenta circles respectively. The arrival time of the two phases (P_{bs} and PP_{bs}) likely overlap at this station. (Bottom) Autocorrelation from the mean 4 Hz (blue) and 1 Hz (black) RF with picked arrival time for Δt . Autocorrelation of a random subset of individual RFs are shown as gray lines in the background. At station 448A, the arrival time of Δt is challenging to pick, likely due to the multiple sediment layers (multiple negative bumps seen in the 4 Hz autocorrelation).

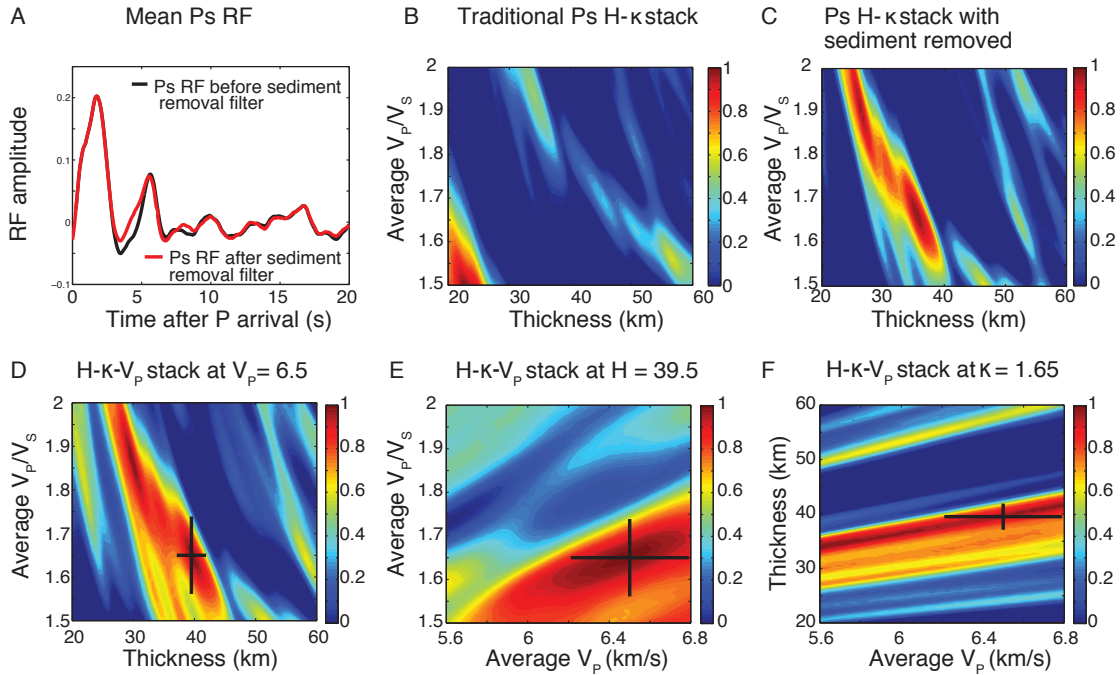


Figure 2.14– SRTC H - κ - V_p stacking of 448A receiver functions. Station 448A is located on the Mississippi Embayment in Mississippi. **A.** The mean Ps receiver function before (gray) and after (red) the sediment removal filter is applied, which do not appear significantly different at this station. **B.** Ps H - κ stack at assumed $V_p = 6.3$, and the maximum of the stack is $H = 24$ km and $\kappa = 1.5$. **C.** The Ps H - κ stack after the sediment removal filter and time correction is applied has a maximum at $H = 36.25$ km and $\kappa = 1.83$. **D, E, & F.** Three cross-sections through the H - κ - V_p triple stack through the maximum of the stack; black cross-hairs denote 1σ error bars.

Several previous studies of the lower Mississippi embayment near the location of TA station 448A find similar results to the crustal values obtained in the SRTC H - κ - V_p triple stacks. In southern Mississippi (slightly further west than station 448A) the Moho depth was found using seismic refraction to be ~ 35 km with an average crustal V_p of 6.4 km/s (Warren *et al.*, 1966), shallower than the SRTC H - κ - V_p stack crustal thickness estimate of 39 km. A global Moho study finds that the Moho depth in this region is between 32 and 36 km with an average crustal V_p of 6.5 km/s (Cook *et al.*,

1981; Mooney et al., 1983). Finally, while there are no EARS results for station 448A, the results for a nearby station, US BRAL, finds a Moho depth of 38 km, a V_p/V_s of 1.87, assuming an average crustal V_p (from Crust 2.0) of 6.53 km/s (Crotwell and Owens, 2005). At this station our crustal thickness estimate is closer to that of EARS estimates at station US BRAL, with a lower V_p/V_s . The low V_p/V_s value found in this study would indicate that the crustal composition beneath this station would be felsic in composition, possibly quartzite or granite (Christensen, 1996).

2.5 Discussion of H- κ - V_p Methodology

By creating the SRTC H- κ - V_p stack, we address two of the major limitations of traditional H- κ stacking: contamination by sediment layers and the *a priori* assumption of an average crustal V_p .

In regions overlain by a sedimentary layer, such as the Williston basin, Atlantic coastal plain, and Mississippi embayment, sediment reverberations overprint deeper crustal conversions and traditional H- κ stacking methods fail. Yeck et al. (2013) proposed the sequential H- κ stacking approach, which characterizes the sediment V_p/V_s and thickness, and uses the result to correct for sediment effects and interpret Moho depth. By using the resonance removal filter and time corrections of Yu et al. (2015), we are similarly able to characterize and suppress the S basin multiples, which are likely to dominate the reverberation signal (**Figure 2.3**) before interpreting Moho depth. However, unlike sequential H- κ stacking, the SRTC H- κ stack is able to constrain crustal properties even when the S-basin multiple and Moho phase arrivals are coincident in time due to the sediment time corrections. Unlike Yu et al. (2015),

we find that in practice, it is easier to use the arrival time of the PP_{bs} phase instead of the P_{bs} phase, due to its larger amplitude.

Assuming an incorrect average crustal V_P may lead to biased estimates of the crustal thickness, even when no sedimentary layer is present (*Yeck et al., 2013*). The H-V stacking method of Rychert and Harmon (*2016*) uses the direct Sp arrival as well as Sp multiples (from the Sp RFs) to constrain average crustal V_P , V_S , and thickness, removing the dependence on average V_P . While this method is robust in areas without sedimentary reverberations, the low amplitude Sp multiples can make it difficult to use Sp RFs when substantial noise is present, which is often the case. For this reason, we choose to supplement the constraints provided by SRTC H- κ by incorporating only the direct Sp conversion in our stacks. The Sp phase arrival is able to provide an additional constraint on the crustal thickness, when the sediment structure has multiple layers (such as at station 448A). To constrain V_P , the SP_{mp} RF is also added, which has proven useful to constrain crustal thickness and velocity in a region where sediment is present (*e.g. Parker et al., 2016*).

A significant concern for the SP_{mp} phase is the effect of azimuthal anisotropy or dipping layers on the arrival time of the SP_{mp} phase. SP_{mp} is observed on a very restricted epicentral distance range (30-50 degrees), and so to look at the variation in arrival time based on back azimuth (BAZ), binned SP_{mp} events are plotted over a range of BAZ bins for permeant seismic station ANMO used because it has events from a range of backazimuths. When plotted by BAZ, the SP_{mp} phase does not show

a strong directional dependence for station ANMO (*Figure 2.18*). This is especially significant as station ANMO lies near the Rio Grande Rift with the Colorado Plateau to the north and the basin and range to the south. The geologic regions have differences in crustal properties and thickness that might be expected to manifest as back-azimuthal variations in the SP_{mp} phase arrival; however, that is not the case, and the SP_{mp} phase shows a clear and consistent arrival from all BAZ bins with more than three existing events, suggesting that stacking SP_{mp} observed at a station is justified. Similar concerns exist for S_p and P_s phases in H- κ stacking, although the back-azimuthal dependence of S_p due to anisotropy is expected to be very complex. In future studies, harmonic decomposition of P_s phases (*e.g. Olugboji and Park, 2016*) can be used to detect and isolate the signature of anisotropy and/or dipping layers, helping to constrain average crustal anisotropy. Additionally, extra care must be taken when considering SP_{mp} RFs for stations near oceanic crust. Since the SP_{mp} waveform is affected by distant crustal structure, and oceanic and continental crust differ dramatically in thickness, analysis should be restricted to include only events with back azimuths that sample the continental crust.

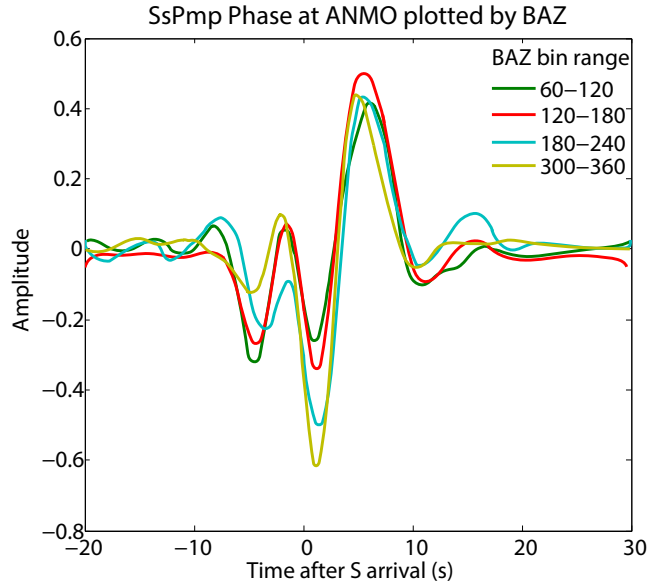


Figure 2.15– SP_{mp} RFs for events between 30 and 50 epicentral distances. Each line is a bin of backazimuthal (BAZ) directions from station ANMO, chosen due to its large range in BAZ of SP_{mp} events. The amplitude and location of the SP_{mp} at ~ 6 s does not change significantly based on BAZ direction which indicates that the SP_{mp} waveforms show evidence of neither crustal anisotropy nor crustal thickness variations with BAZ. We expect this observation to hold true for most other stations, due to the low frequency of SP_{mp} waveforms.

The resonance removal filter will effectively remove S-wave reverberations associated with the low velocity layer in Ps RF. One concern is that contamination from additional sedimentary reverberations (such as PP_{bs} reverberations) may still mask the crustal phase arrivals even after the resonance removal filter is applied. We find that if the sedimentary V_S is very low (has an average velocity of less than 0.5 km/s) and sediment is thick (around 3 km), while the crust is extremely shallow (less than 20km) it is possible for large amplitude PP_{bs} to arrive at the same times as direct P_{ms} conversion from the Moho and its reverberations to arrive directly after Moho phases. In these rare cases, the sediment P-wave multiples may stack coherently near the maxima, biasing the crustal thickness estimate 0.5-1.0 km deeper than input

values and V_p/V_S by 0.02-0.03 higher than input value and therefore, the SRTC H- κ - V_p triple stack may be contaminated by PP_bs and should not be used (**Figure 2.4**). When the average sediment V_S is larger or the sediment is not as thick, S-wave reverberations are the most dominant signal in the Ps receiver functions. (**Figure 2.2, Figure 2.3**).

One limitation of the resonance removal filter is that it assumes a single shallow layer, and only removes reverberations from the largest amplitude resonances – typically, the S-wave reverberations – in the Ps RF. The way it has been implemented in this study, the resonance removal filter does not remove reverberations from multiple distinct shallow layers that may add further reverberations. While we find that removing the largest reverberations is sufficient to constrain the crustal thickness and crustal average crustal velocities (V_p/V_S and V_p) at these stations, applying a secondary resonance removal filter could further reduce oscillatory conversions associated with multiple layers. For example, in the case of multiple low velocity sediment layers, a secondary resonance removal filter, applied after the first, may be able to remove reverberations associated the layer bounded by second-largest impedance contrasts. In regions where S-wave reverberations of the whole crust are particularly prominent, an extension of this method may be to apply a secondary resonance removal filter to remove reverberations from the crust/mantle boundary (Moho) that can mask intra-lithospheric arrivals at approximately 7-10 seconds (about 80-100km).

2.6 H- κ - V_p Conclusions

Traditional H- κ stacking is commonly used to constrain crustal thickness and V_p/V_s beneath a seismic station, but requires an assumed average crustal V_p and fails in the presence of a low velocity sedimentary layer. Previous studies have been able to remove sediment contamination (Yeck *et al.*, 2013) or remove the dependence on average crustal V_p (Rychert and Harmond, 2016) with some success. We present the sediment-removed, time corrected (SRTC) H- κ - V_p stacking method that is able to remove sediment contamination even when multiples directly overprint crustal signals while also yielding constraints on average crustal V_p .

The SRTC H- κ - V_p stacking method uses quantitative thresholds to determine whether large amplitude oscillatory sedimentary reverberations are present in the Ps RF. It then applies a resonance removal filter and time corrections from Yu *et al.* (2015) to the Ps RFs, and adds complementary Sp and SP_mp RFs, with their respective time corrections. Synthetic data is used to verify that this method is effective in constraining crustal properties when sediment reverberations contaminate deeper crustal conversions. When applied to EarthScope TA stations in the presence of sediment, and find that overall, our estimates of H, κ , and V_p agree well with previous studies. At stations where traditional H- κ stacking implies an unlikely crustal thickness and V_p/V_s ratio, a more reasonable estimate for the crustal properties is obtained after the SRTC H- κ - V_p stacking method is applied. Because using the H- κ - V_p stacking method requires fewer *a priori* assumptions about the underlying crustal

structure, including whether a sedimentary layer is present, it is straightforward to be applied to large seismic arrays regardless of geologic/tectonic regime.

We show that both resonance removal and time corrections can reduce the complexity introduced into traditional H- κ stacks by shallow layer reverberations. We ensure that error calculations capture uncertainty arising from our ignorance about the values of the other parameters. This allows us to better define and estimate error around one clear maximum in the triple stack. However, this method does not provide an efficient way to express error if multiple maxima are present. For a large-scale study using the SRTC H- κ - V_p stacking, a complexity term based on the amplitude of the next closest maxima in the stack is suggested. In a regional study, when multiple maxima are present at a station, nearby stations can be used to constrain the correct crustal parameters in complex stacks, and a search range for H, κ , and V_p be based on existing crustal models near the seismic station, such as Crust 2.0 (Crotwell and Owens, 2005) can be implemented to constrain reasonable crustal values and reduce computation time.

Though our method avoids making prior assumptions about average crustal V_p , which is necessary in traditional H- κ stacking, V_p is often poorly constrained using this method, with error up to ± 0.6 km/s. While the constraint on crustal V_p is sufficient for this study, we recognize that tighter constraints on crustal V_p may be necessary to for other applications, such as for drawing inferences about crustal composition. Even when including complementary Ps, Sp and SP_{mp} data, we find that the data are not

particularly sensitive to V_p , which is reflected in our estimated errors (between 0.3-0.6 km/s). Where data from active source studies is available (e.g. Lithoprobe (Clowes *et al.*, 1987; Cook *et al.*, 1988; White *et al.*, 1994; Ross *et al.*, 1995) or COCORP (Cook *et al.*, 1981; Allemendinger *et al.*, 1983; Peterson *et al.*, 1984) seismic lines), V_p can be constrained more tightly using them. Alternatively, joint inversion of receiver functions with surface wave data can better constrain crustal V_p (e.g. Julia *et al.*, 2000; Lawrence and Wiens, 2004; Shen *et al.*, 2013). Because our work suggests that removal of sediment multiples can clarify constraints from receiver functions, it is likely to improve results of such joint inversions.

From the Ps receiver functions and resonance removal filter, we obtain information that can be used to constrain sedimentary layers. Specifically, the amplitude and travel time of the S-wave reverberation in the sediment that when combined with assumptions about the relationship of V_p and V_s may be used to estimate sedimentary thickness and velocity. Thick sedimentary layers lead to increased amplitude and duration ground shaking during a seismic event, so mapping the structure of sedimentary basins over large regions has implications for seismic hazard mapping.

Chapter 3: Constraining Basin Fundamental Frequency and Velocity Profiles of the Atlantic Coastal Plain using Receiver Functions

3.1 Introduction to Hazard in the Atlantic Coastal Plain

Despite being situated on a passive margin, the East Coast of the United States has suffered from very damaging and costly earthquakes. Many densely populated East Coast cities that lie on Coastal Plain sediments contain old buildings and infrastructure (**Figure 3.1**). The large impedance contrast between Atlantic Coastal Plain (ACP) basins and underlying igneous or metamorphic bedrock cause incoming seismic waves to become amplified and trapped in the basin, leading to prolonged and damaging ground motion (e.g., *Field et al., 1990; Fischer et al. 1995; Baise et al., 2016; Yilar et al. 2017*). Amplification by sedimentary layers and matching fundamental frequencies of sedimentary basins and built structures is likely responsible for the substantial damage resulting from even moderate-sized earthquakes on the East Coast, such as the Mw 5.8 2011 Mineral, VA earthquake (*Pratt et al., 2017*).

Mapping the fundamental frequency and amplification of basins is useful for geoen지니어ing and hazard assessment as overlap between the fundamental resonant frequencies of basins and buildings can be particularly damaging (e.g. *Flores et al., 1987*). Typically, the average velocity to 30 m depth (V_{S-30}) is used as a proxy for site amplification in hazard analysis and ground motion prediction equations (e.g. *Abrahamson and Silva; 2008*). These site characterizations by V_{S-30} are typically used to inform seismic building codes (e.g. *NEHRP Provisions*). However,

characterizing only the very shallow soil and sediment to 30 m may not be sufficient to describe damaging site effects, particularly for larger buildings and infrastructure. More recent studies argue that fundamental period (inverse of fundamental frequency), or fundamental period combined with a velocity term (e.g. V_S-30 , $Z_{1.0}$, or $Z_{2.5}$) is a better proxy for site amplification and response and reduces uncertainty in ground motion prediction equations (*Luzi et al. 2011; Pitilakis et al. 2013; Zhao and Xu, 2013*).

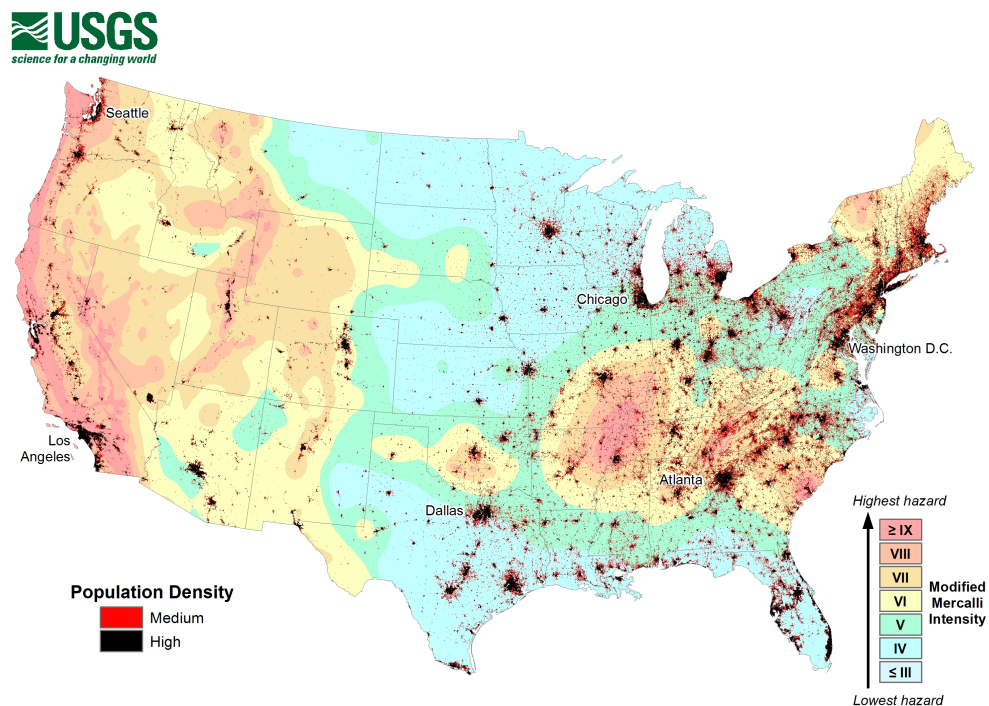


Figure 3.1- USGS map showing the location of populations in red/black on top of the intensity of potential earthquake ground shaking that has a 2% change of occurring in 50 years (Figure from *Jaiswal et al., 2015*)

High fundamental frequencies associated with soil and shallow sediment reverberations pose a problem to short buildings that may have matching resonant frequencies. However, the large impedance contrast between the bedrock and the basin in the ACP means that the peak amplification should occur at the basin fundamental frequency (*Pratt et al. 2003; Narayan, 2010*). Because basins within the ACP are relatively thick and wide when compared to West Coast (*AAPG Basement Map of North America, 1978*), the basin fundamental frequency in the ACP will be low and will influence shaking over larger areas. The low fundamental frequencies of the basin predominantly affect larger structures with matching resonant frequencies (e.g. bridges, tall buildings, industrial facilities), which is of particular concern for cities situated on the East Coast where large buildings and infrastructure were constructed before current seismic building codes were in effect. Thus, it is crucial for hazard analysis to constrain the amplification and fundamental frequencies across the ACP.

Common methods employed to estimate fundamental frequency are the standard spectral ratio (SSR), and the ambient noise or earthquake horizontal-to-vertical spectral ratio (HVSr or E-HVSr respectively). The SSR technique requires comparing ground motions from local earthquakes at a target site located on sediment to a reference site with no sediment that overlies the same bedrock material. (e.g. *Borcherdt 1970; Frankel et al., 2002; Pratt et al. 2017; Perron et al. 2018*). However, good reference sites with the same underlying bedrock material may not be available for all ACP stations. Mismatch in the bedrock material between the target

and reference sites will degrade the accuracy of the seismic hazard interpretation (Steidl *et al.*, 1996). In contrast, the HVSR techniques do not require a reference station. Instead, HVSR isolates the horizontal response from the vertical through spectral division, as horizontally polarized S-wave will cause the most ground shaking during an earthquake (e.g. Nakamura, 1989; Lermo *et al.*, 1993; Nakamura, 2000; Mendeck *et al.*, 2014; Pratt *et al.* 2017). In some cases where available data is sparse, such as in the central and eastern US, the resonance peak that is used to infer fundamental frequency may not be clear and may prove difficult to interpret (Pratt *et al.*, 2017). In the Central and Eastern US dense high-frequency seismic surveys are rare, and so broadband seismic stations may be useful for constraining the fundamental frequency. However, with traditional techniques constraining the fundamental frequency of the Atlantic Coastal Plain basin may still prove difficult (Yassminh *et al.*, 2019).

Here, we propose, validate, and apply a different approach to constrain key basin properties by using high frequency P-to-s receiver function analysis. P-to-s receiver functions (PRFs) isolate the S-wave conversions across a large impedance contrast (product of velocity and density) through deconvolution, similar to H/V techniques. However, they can be analyzed in the time domain where individual arrivals are easily associated with S or P-wave reverberations. Although PRFs are traditionally used to constrain crustal and lithospheric structure, high-frequency PRFs are strongly sensitive to shallow impedance contrasts such as that between the basin and bedrock (Zelt and Ellis, 1999; Leahy *et al.*, 2012; Yeck *et al.* 2013). Therefore, we propose to

use measurements of converted S-waves and reverberations from the high-frequency PRFs calculated for *EarthScope* USArray Transportable Array (TA) broadband seismic stations to characterize the basin structure in the ACP.

Due to the large impedance contrast between basin and bedrock material, strong S-wave reverberations are present in the P-wave coda. Computing the autocorrelation of the PRFs allows us to easily measure the two-way S-wave reverberation time (T_{Ss}) in the basin (*Yu et al., 2015*), which is directly related to the fundamental frequency of the basin. The basin fundamental frequency is calculated from measurements of T_{Ss} at each broadband seismic station, allowing for a map of basin fundamental frequency across the ACP to be created.

We find that PRFs are also useful in constraining other basin properties, including the P and S-wave velocity profiles. Using T_{Ss} , along with interpolated basin thickness (*Figure 3.2*), an average basin S-wave velocity profile of the ACP is inferred. By incorporating the arrival time of one additional phase, T_{PPbs} , an average P-wave velocity profile is also obtained. We validate these velocity profiles using calculated reflection coefficients of the basin impedance contrast compared to amplitudes of the measured phase arrivals (PP_{bs} and the S-wave reverberation), as the amplitude is related to the impedance discontinuity between basin and bedrock.

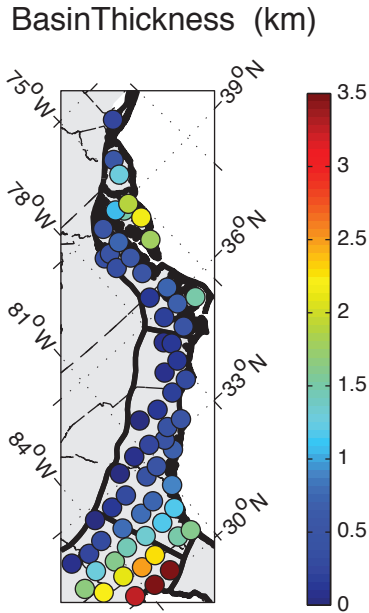


Figure 3.2- Basin thickness for stations on the Atlantic Coastal Plain (*Fenneman and Johnson 1946*) inferred from basement depth interpolated from *AAPG Basement Map of North America, 1978*

3.2 Receiver Function Data for the ACP

High-frequency P-to-s receiver functions (PRFs) are calculated for 75 broadband seismometers from the *EarthScope* Transportable Array (TA) stations located on the Atlantic Coastal Plain of the United States (*Fenneman and Johnson, 1946*). To calculate PRFs, we use 300 s long windows of three-component waveform data (aligned so that the P arrival is at 75 s) from teleseismic events with $M_w > 5.6$ and epicentral distances between 30° and 90° from each station. The events are quality controlled, extracting those with a minimum Z-to-R cross correlation of 0.3, and a maximum difference of 25s between the automatically-determined arrival time and prediction for ak135, with no requirement on minimum signal to noise threshold. (See Data and Resources, *Abt et al., 2010*). We use a free-surface transform matrix

(Kennett, 1991) and find the surface velocity that minimizes the parent amplitude (P for PRFs) on the daughter component to project the waveforms onto the P-SV-SH system. We pick the arrival times and apply a fourth order Butterworth band-pass filter to waveforms of 0.03-4 Hz. We then use the iterative time domain deconvolution with Gaussian half-amplitude half-width of ~ 0.12 s to calculate the 4Hz PRFs (Ligorria and Ammon, 1999). This is done following the automated procedure detailed in Abt et al. (2010).

The 75 seismic stations within the ACP are further culled to only those that show clear sedimentary basin arrivals in the receiver functions. Following the guidelines laid out in **Chapter 2**, we require that the autocorrelation of the PRF can be sufficiently-well fit by a decaying sinusoid – meaning that the PRF displays the oscillatory effect of reverberations trapped in a sediment basin – and that amplitude of the PP_{bS} conversion is at least 30% of the maximum amplitude in the signal. We find that 11 of the stations determined to be in the ACP are located on bedrock material with no significant sediment signal in the PRF. In the end, we obtain a dataset of 64 stations that meet these criteria, exhibiting visible sedimentary reverberations, and containing between 31 and 304 individual PRFs per station.

3.3 Basin Fundamental Frequency

In order to map the basin fundamental frequency across the ACP, we measure the two-way S-wave travel time in sediment from PRFs at each station. The large impedance contrast between the basin and basement material means that PRFs are particularly sensitive to s-wave reverberations. The conversions and reverberations

produced from this impedance contrast appear as peaks on the receiver function corresponding to ray paths shown in **Figure 3.3A** and relative phase arrival times shown in **Figure 3.3B**. In PRFs, the largest amplitude, longest duration oscillatory phases are those that contain the two-way S-wave reverberation (PS_bS , P_bS-2S , PP_bS-2S , PS_bS-2S , P_bS-4S , PP_bS-4S , etc.), which dominate the PRF signal. The reverberations at longer times contain primarily S-wave energy due to fact that PRFs are computed from upgoing P and S waveforms estimated using the free-surface transform (*Kennett, 1991*), and because the SS reflection coefficient at the base of the layer is large. While the S-wave reverberation time (T_{Ss}) and amplitude (r_0) can be inferred directly from the PRFs, a more reliable method is to make this measurement on the autocorrelation of the receiver function (*Yu et al., 2015; Chapter 2*). When a low velocity basin layer is present, the autocorrelation of the receiver function will have a large negative peak at reverberation time T_{Ss} and amplitude $-r_0$. Because the S-wave reverberations are nearly vertical, the mean PRF at each station can be used to calculate the autocorrelation. We validate this with a synthetic receiver function (**Figure 3.4A**) and show example station measurements (**Figure 3.4B-C**).

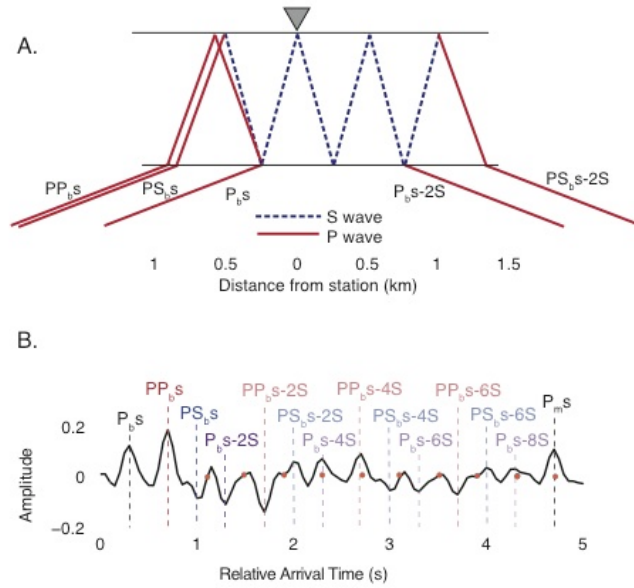


Figure 3.3- *A.* Ray-path geometry of P-to-s phases converted across the base of a 0.5 km thick sediment layer, along with the largest-amplitude first- and second-order multiples for an incident plane wave of horizontal slowness 0.0789 s/km. *B.* Synthetic receiver functions computed for a model with a 0.5 km thick sediment layer and horizontal slowness 0.06 s/km ($V_P = 2.5$ km/s, $V_S =$ km/s), crustal $V_P = 6.2$ km/s, $V_S = 3.5$ km/s, a Moho at 35 km depth, and mantle $V_P = 8$ km/s, $V_S = 4.6$ km/s. Direct conversions are in black, while the oscillatory pattern is attributed to sediment multiples, labeled in red, blue and purple. Orange dots indicate where the expected arrival of phase with more than 2 P-wave legs would arrive.

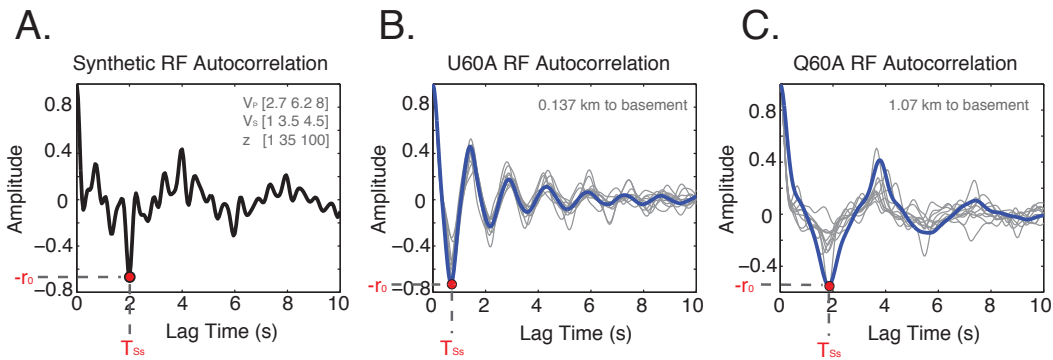


Figure 3.4- TSs and r_0 measurements from 4 Hz Ps receiver function autocorrelations. With increasing sediment thickness, TSs increases. *A.* Autocorrelation of Synthetic RF calculated for velocity model described in

top right corner. TSs and r_0 are picked as the first negative large amplitude, shown by the red dot. B. Autocorrelation of 4 Hz Ps RFs for station U60A located on 0.137 km of basin material. Mean autocorrelation shown in blue and a range of Ps RF autocorrelation events shown in gray. TSs and r_0 pick shown as red dot. C. Autocorrelation of 4 Hz Ps RFs for station Q60A located on 1.07 km of basin material. Mean autocorrelation shown in blue and a range of Ps RF autocorrelation events shown in gray. TSs and r_0 pick shown as red dot.

Measurements of T_{Ss} and r_0 are made for stations across the ACP. As expected, with increasing basin thickness from west to east, T_{Ss} increases (**Figure 3.5A**, **Figure 3.6A**). Deeper basins will have faster velocities at the base, reducing the impedance contrast between basin and bedrock. Therefore, as basin thickness increases, r_0 is expected to decrease, consistent with our observations shown in **Figure 3.5B** (**Figure 3.6B**).

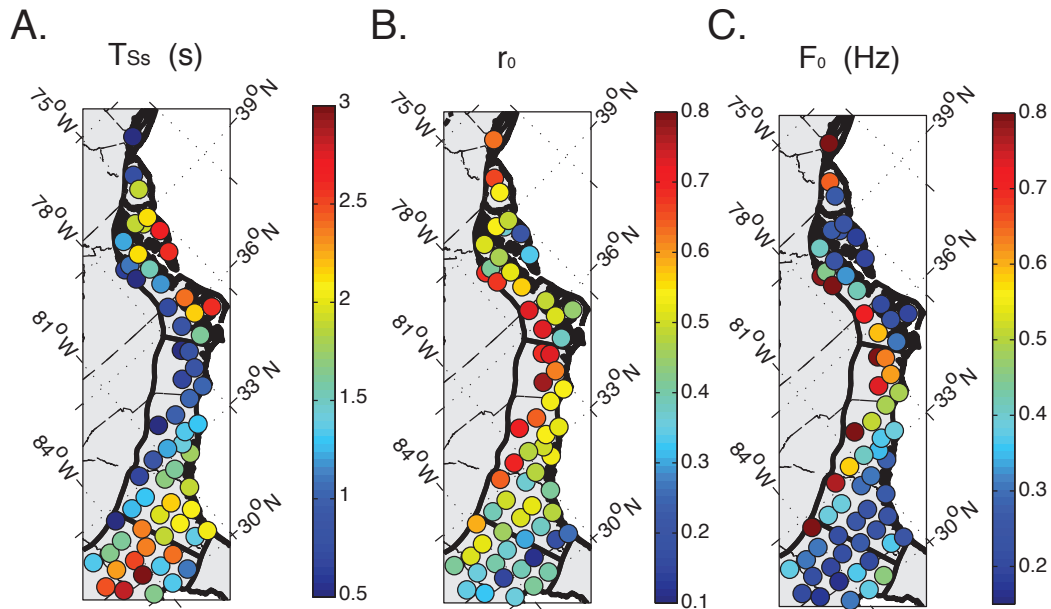


Figure 3.5- Measurements from the 4Hz Auto-correlated RFs across the ACP. A. Measurements of T_{Ss} at each station across the ACP. As basin thickness increases T_{Ss} increases. B. Measurements of r_0 across the ACP. As basin thickness increases, the r_0 (related to the impedance contrast) decreases. C. Fundamental Frequency which is related to T_{Ss} as $F_0 = \frac{1}{2T_{Ss}}$ across the ACP.

Assuming that the S-wave reverberations are near vertical in the slow sedimentary basin, the relationship between T_{Ss} and basin fundamental frequency becomes quite simple. The basin fundamental frequency (F_0) depends on the S-wave velocity (V_S) and basin thickness (H_b) in the quarter wavelength approximation (Joyner *et al.*, 1981; Shearer and Orcutt, 1987; van der Baan 2009) as: (3.1) $F_0 = V_S/4H_b$. Assuming near-vertical incidence in the low velocity basin layer, two-way S-wave travel time in sediment (T_{Ss}) is: (3.2) $T_{Ss} = 2H_b/V_S$, so that fundamental frequency is related to T_{Ss} by: (3.3) $F_0 = 1/2T_{Ss}$. Assuming vertical incidence introduces errors that are negligible compared to observational uncertainty; for example the approximation introduces an error of $< 0.2\%$ (3 ms for a 2 s travel-time) in T_{Ss} for a typical ray parameter of 0.05 s/km for the incoming P wave and a 1 km thick sediment with $V_S = 1$ km/s. Transforming the station measurements of T_{Ss} for F_0 accordingly, we produce a map of site-specific fundamental frequency across the Atlantic Coastal Plain (**Figure 3.5C**) obtaining fundamental frequencies ranging from 1.1 Hz in shallow basins to 0.16 Hz in deeper ones (**Figure 3.6C**).

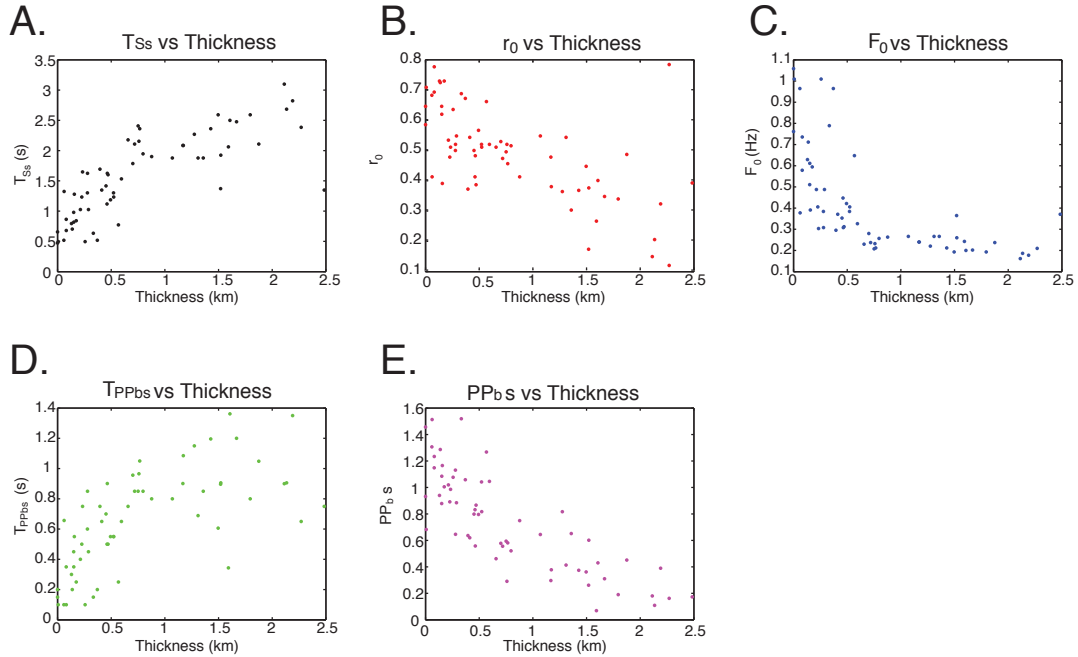


Figure 3.6- Station measurements plotted vs. basin thickness. *A.* T_{Ss} increases with increasing basin thickness *B.* r_0 decreases with increasing basin thickness *C.* F_0 decreases with increasing basin thickness *D.* T_{PPbs} increases with increasing basin thickness *E.* $PP_b s$ decreases with increasing basin thickness.

3.4 Basin Velocity Profiles

3.4.1 ACP Basin V_S Profile

When the basement depth and fundamental frequency is known, the S-wave velocity of the sediment can be found (*e.g. Bodin et al., 2001; Parolai et al., 2002; Setphenson et al. 2019*). Due to trade-offs between sediment thickness and velocity, inferring the average S-wave velocity structure of the ACP using measurements of T_{Ss} requires additional information and assumptions. The most important additional information needed is that sediment thickness at each seismic station can be estimated

from existing studies. Borehole data with estimates of basin thickness along the Atlantic Coastal Plain is available from AAPG (*AAPG Basement Map of North America, 1978*) and aggregates state-by-state surveys of basin thickness. The basin thickness data is interpolated from published contour maps to give an approximate sediment thickness at each of our station locations (*Figure 3.2*). Because basins within the ACP are relatively thick and wide containing nearly horizontal layers of sediment (*DiPietro, 2018; Pratt, 2018*), we make the assumption that sediment within the ACP at a given depth will have similar velocities across fairly wide geographic regions, allowing for the inversion of the average ACP basin velocity profiles instead of separate profiles beneath each station. Finally, we assume that the seismic velocity in the basin does not have internal interfaces and that V_S increases smoothly with depth. These assumptions, along with measurements of T_{Ss} from receiver functions, allow us to estimate an average 1-D velocity profile for the ACP.

To invert for the S-wave velocity of the ACP, we seek a single velocity profile that minimizes the misfit between predicted and observed T_{Ss} at all stations. We parameterize the velocity profile assuming a power-law dependence of V_S with depth, which has been found to be a good description in the shallow subsurface (*Delgado et al., 2000*). An additional advantage of this parameterization is that multiple studies have computed generic surface wave dispersion and eigenfunction expressions for such velocity profiles (*Godin and Chapman, 2001; Tsai and Atiganyanum, 2014*). In order to explicitly account for uncertainty in our measurements, we use a Bayesian inversion framework. To minimize the influence of outliers on the inferred V_S

profiles, we define an L1-norm misfit function $\phi_d(m)$ for N stations: (3.4)

$$\phi_d(m) = \sum_{i=1}^N \frac{|T_{Ss_i}^{obs} - T_{Ss_i}^{pred}|}{\epsilon};$$

where $T_{Ss_i}^{obs}$ is the observed and $T_{Ss_i}^{pred}$ is the model-predicted T_{Ss} at each station i , and ϵ is the standard deviation of the T_{Ss} error measurement. Based on variations observed using different subsets of data, we fix ϵ to be 0.1 s.

The predicted T_{Ss} are calculated from *eq.(2)* using the S-wave velocity at each depth calculated as: (3.5) $V_S(z) = V_0 + a_1(z)^p$, where V_0 is the starting S-wave velocity at the surface, z is the depth and a_1 and p are parameters which describe the shape of the power-law dependence of velocity with depth, and $0 < a_1 < 2.7$ and $0 < p < 1$. We use a Markov Chain Monte Carlo approach to obtain best-fit parameter values and map out uncertainties and trade-offs among them.

We find that the best-fit V_S profile does not adequately predict the measurements of T_{Ss} for very thick basins, greater than 2.5 km to basement (**Figure 3.7**). The four stations that lie on top of very thick basins (454A, 553A, 554A, 555A) are within the South Georgia Rift Basin (SGR- **Figure 1.1**) (*Wagner et al., 2018*). We interpret the T_{Ss} picks at these stations to likely be coming from an intra-sedimentary interface with a large impedance contrast (such as between unconsolidated and consolidated sediment), and not from the basin/basement impedance contrast. Therefore, these points are excluded and the inversion is performed for stations with a basement depth of less than 2.5 km thick. We invert for the average profiles of the entire ACP, as well as for the Florida and Eastern Gulf Coastal Plain sediments (FEG) and Coastal Plain

(CP) profiles, separately. The three resulting V_S profiles are very similar (**Figure 3.8**); with the parameters of the inversion also remaining similar (**Figure 3.9**). This justifies our assumption of geographic uniformity of velocity at a particular depth within the ACP, and produces an equation for V_S velocity of the basin as: (3.7) $V_S(z) = 0.46 + 0.53(z)^{0.54}$. Interestingly, p remains close to 0.5 for all of the models, which implies a linear increase of shear rigidity with depth (*Chapman and Godin, 2001*).

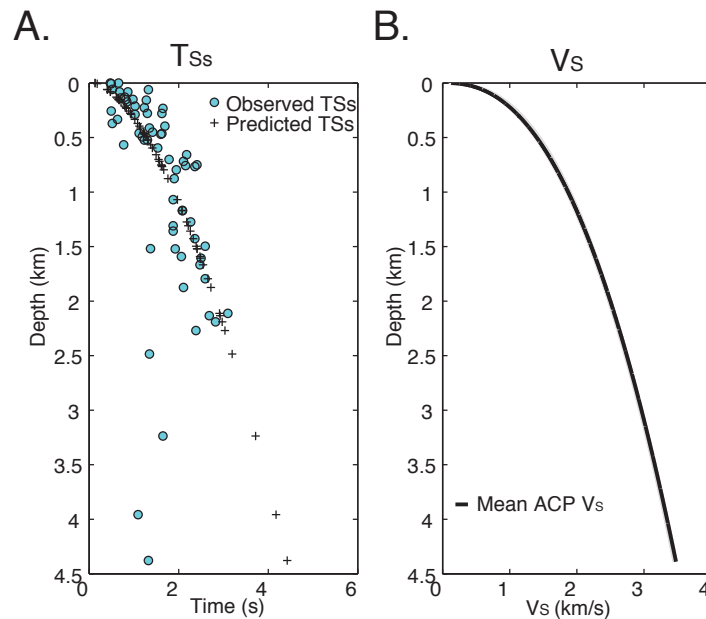


Figure 3.7- V_S velocity profile from inversion. **A.** T_{Ss} measurements from and 4Hz Ps RFs (cyan circles) compared to T_{Ss} predicted from the mean V_S profile from our best-fit inversion (black crosses) **B.** V_S velocity inversions using T_{Ss} measurements and assuming V_S increases in a power-law fashion with depth. A range of velocity inversions using all stations is plotted in gray, and the mean of these models is plotted in black

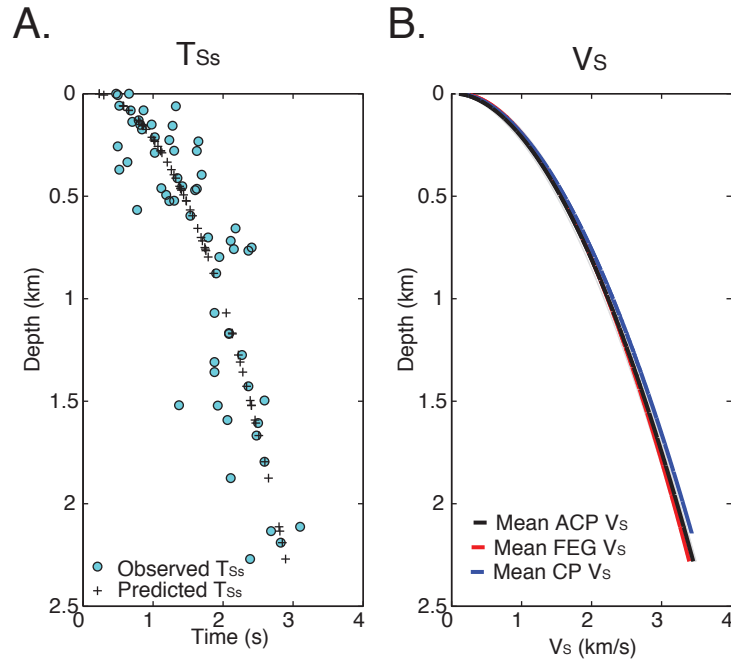


Figure 3.1- V_S velocity profile from inversion. **A.** T_{Ss} measurements from and 4Hz Ps RFs (cyan circles) compared to T_{Ss} predicted from the mean V_S profile from our best-fit inversion (black crosses) **B.** V_S velocity inversions using T_{Ss} measurements and assuming V_S increases in a power-law fashion with depth. A range of velocity inversions using stations with basin thickness less than 2.5 km are plotted in gray, and the mean of these models is plotted in black. The mean velocity inversion for the stations in the Florida and Eastern Gulf Coastal Plain sediments (FEG) is plotted in red, and the mean velocity inversion for the stations in the Costal Plain (CP) is plotted in blue.

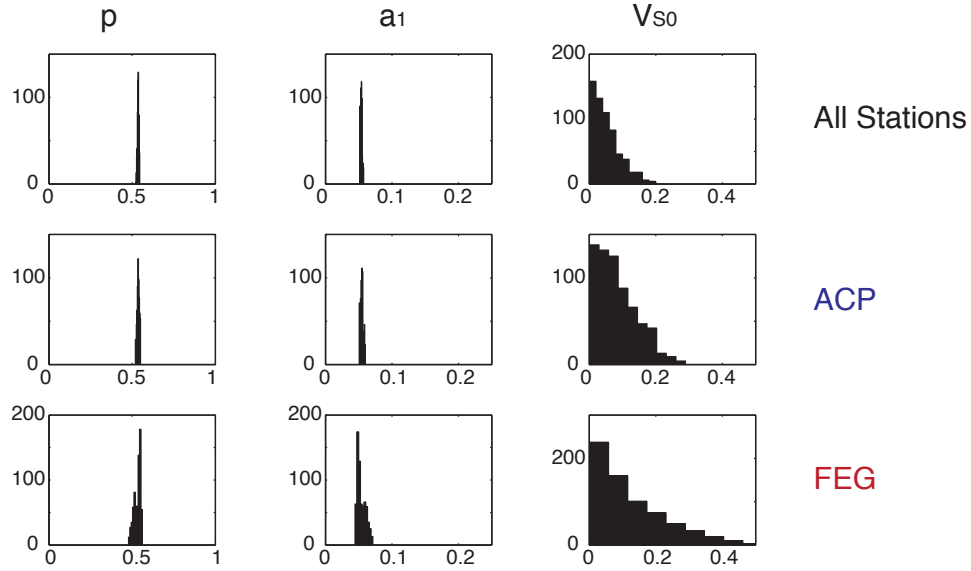


Figure 3.2- Parameters from VS profile inversion (p , a_1 , and V_{S0}) for all stations with basement thickness less than 2.5; ACP stations; FEG stations.

3.4.2 ACP Basin V_P Profile

Because the P reverberations within the sedimentary column are less prominent than S reverberations, constraining the average ACP V_P profile from receiver function data is more difficult. Indeed, since P-to-S receiver functions isolate the S-wave conversions from subsurface interfaces, prominent phases always include at least one S-wave leg; therefore the timing of any phase arrival will depend on the S-wave travel time through the basin. Therefore, inverting for the V_P profile requires not only making an arrival time measurement on a phase sensitive to the V_P in the basin, but also involves the same data – measurements of T_{Ss} – and assumptions used for obtaining a V_S profile. Here, we focus on PP_{bS} , which is usually the largest amplitude phase arrival on the RF that contains a P-wave traveling in the sediment (**Figure**

3.3B). Assuming near vertical incidence, the travel time of PP_{bs} (T_{PPbs}) depends on the basin thickness (H_b), P-wave velocity (V_P), and basin S-wave travel time as (3.8) $T_{PPbs} = H_b/V_P + \frac{1}{2}T_{SS}$. The measurement of T_{PPbs} and the PP_{bs} phase amplitude is shown for a synthetic receiver function (**Figure 3.10A**) and for two example stations with varying sediment thicknesses (**Figure 3.10B-C**). It is important to note measurements of T_{PPbs} depend on the frequency of the receiver function. For thin sediments, the large amplitude PP_{bs} phase and the earlier arriving direct P-to-s sediment conversion, P_{bs} , may become indistinguishable from one another and overlap in time (**Chapter 2**). For this reason we use the high frequency 4Hz RF to measure T_{PPbs} .

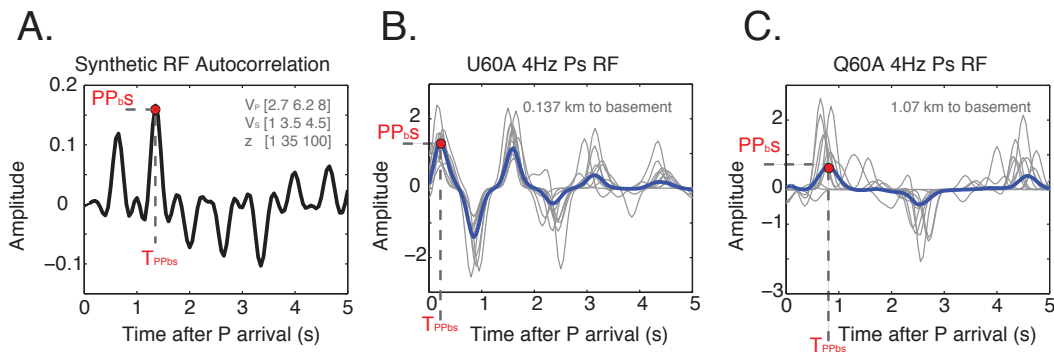


Figure 3.3- T_{PPbs} and PP_{bs} measurements from 4 Hz Ps receiver functions. With increasing sediment thickness, T_{PPbs} increases. A. Autocorrelation of Synthetic RF calculated for velocity model described in top right corner. T_{PPbs} and PP_{bs} are picked as the largest positive amplitude, shown by the red dot. B. 4 Hz Ps RFs for station U60A located on 0.137 km of basin material. Mean Ps RF shown in blue and a range of Ps RFs shown in gray. T_{PPbs} and PP_{bs} pick shown as red dot. C. 4 Hz Ps RFs for station Q60A located on 1.07 km of basin material. Mean Ps RF shown in blue and a range of Ps RFs shown in gray. T_{PPbs} and PP_{bs} pick shown as red dot

Measurements of T_{PPbs} and the PP_{bs} phase amplitude are made across the ACP. The

same trends as with T_{Ss} are found. With increasing basin thickness from west to east, T_{PPbs} increases (**Figure 3.11A, Figure 3.6D**). Deeper basins will have faster velocities at the base, reducing the impedance contrast between basin and bedrock. Therefore, as basin thickness increases, as expected, the PP_{bs} phase amplitude decreases (**Figure 3.11B, Figure 3.6E**). This systematic behavior gives us confidence in the travel time and amplitude measurements of PP_{bs} made on high frequency RFs.

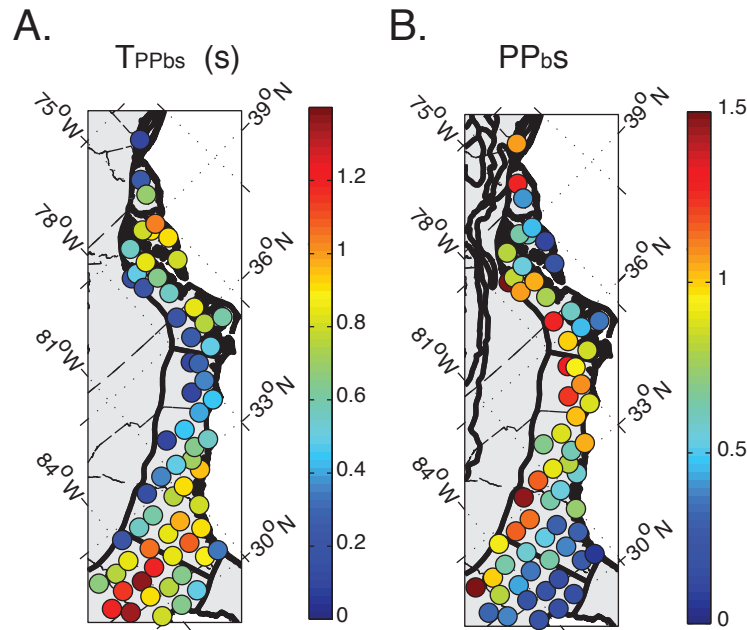


Figure 3.4- Measurements from the 4Hz RFs across the ACP. A. Measurements of T_{PPbs} at each station across the ACP. As basin thickness increases T_{PPbs} increases. B. Measurements of r_0 across the ACP. As basin thickness increases, the amplitude of PP_{bs} (related to the impedance contrast) decreases.

The V_p velocity profile is obtained assuming the same type of power law relationship with depth used for V_s (**Figure 3.12**). We invert for the V_p profile using all stations with basins thickness of less than 2.5 km, as well as separately for stations in the FEG and on the CP. We find that all three inversions prefer higher exponents (p) than for V_s , and that the accepted models show more variation than those of the V_s profile;

both a_1 and p are poorly constrained by the data (**Figure 3.13**). Inverted V_P profiles are compared to the V_P profile predicted by the V_S profile by the regression fit of Brocher (2005) (specifically, *eq. (9)* in that study), which is valid for sedimentary lithologies with S-wave velocities less than 4.5 km/s. The “Brocher regression” V_P profile (predicted from V_S profiles inverted from our data) is significantly different from the V_P profiles calculated with the power-law relationship. Therefore, we repeat the inversions for V_P profiles fixing $p = 1$, i.e. assuming that V_P increases linearly with depth. Assuming a linearly increasing V_P with depth, i.e. (3.9) $V_P(z) = V_0 + a_1(z)$, where V_0 is the V_P at the surface, and a_1 is the velocity gradient with depth, and $0 < a_1 < 2$. We perform the inversion on the same station groups and find much better agreement between model solutions (**Figure 3.14**); elimination of p as a free parameter results in both a_1 and V_0 are well constrained (**Figure 3.15**) producing a V_P profile follows the equation: (3.10) $V_P(z) = 1.99 + 1.95(z)$. When the resulting linear V_P profiles are compared to the V_P profile obtained from applying the Brocher (2005) relationship to the V_S profiles obtained previously, the differences are observed to be minimal.

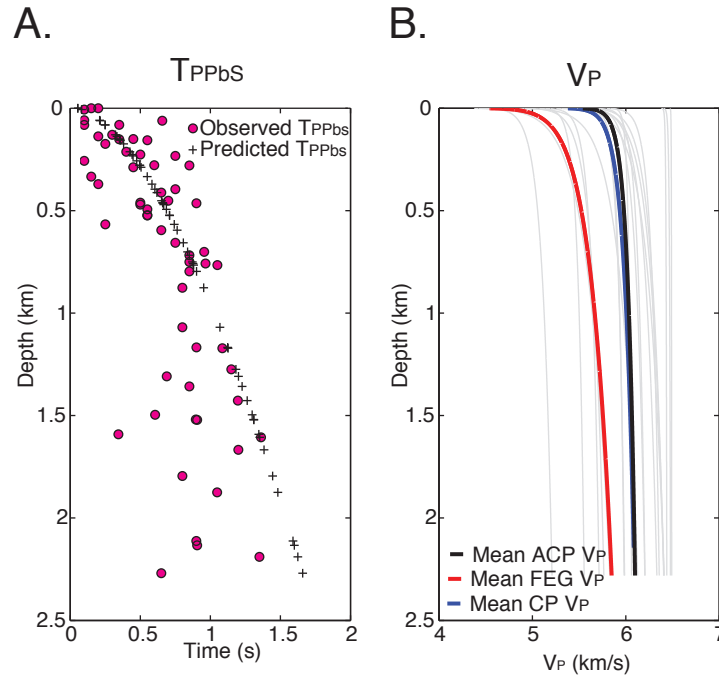


Figure 3.5– V_P velocity profile from inversion. **A.** T_{PPbs} measurements from and 4Hz Ps RFs (magenta circles) compared to T_{PPbs} predicted from the mean V_P profile from our best-fit inversion (black crosses) and T_{PPbs} predicted from the Brocher (2005) relationship of V_P and V_S (green crosses) **B.** V_P velocity inversions using T_{PPbs} measurements and assuming V_P increases in a power-law fashion with depth. A range of velocity inversions using stations with basin thickness less than 2.5 km are plotted in gray, and the mean of these models is plotted in black. The mean velocity inversion for the stations in the Florida and Eastern Gulf Coastal Plain sediments (FEG) is plotted in red, and the mean velocity inversion for the stations in the Coastal Plain (CP) is plotted in blue, and the V_P profile from the Brocher (2005) relationship is plotted in green. The velocity profile is not well constrained by any of the data.

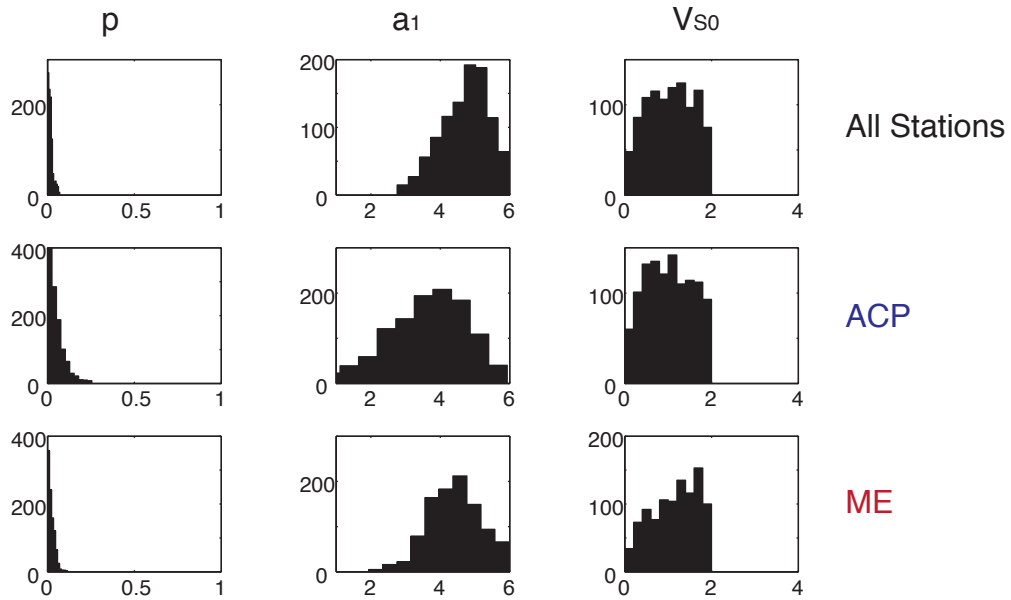


Figure 3.6– Parameters from VP profile inversion (p , a_1 , and V_{S0}) for all stations with basement thickness less than 2.5; ACP stations; FEG stations

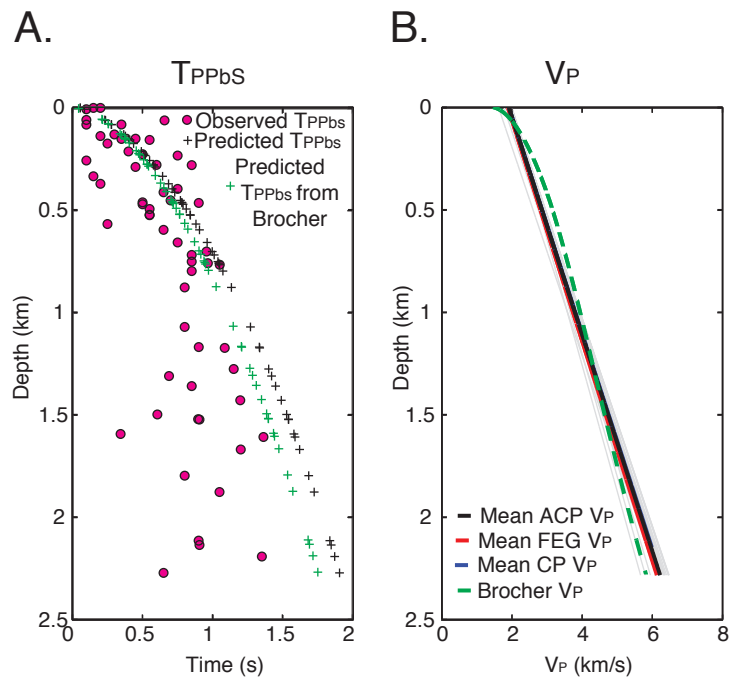


Figure 3.7– V_P velocity profile from inversion. **A.** T_{PPbs} measurements from and

4Hz Ps RFs (magenta circles) compared to T_{PPbs} predicted from the mean V_P profile from our best-fit inversion (black crosses) and T_{PPbs} predicted from the Brocher (2005) relationship of V_P and V_S (green crosses) **B**. V_P velocity inversions using T_{PPbs} measurements and assuming V_P increases in a linearly with depth. A range of velocity inversions using stations with basin thickness less than 2.5 km are plotted in gray, and the mean of these models is plotted in black. The mean velocity inversion for the stations in the Mississippi Florida and Eastern Gulf Coastal Plain sediments (FEG) is plotted in red, and the mean velocity inversion for the stations in the Costal Plain (CP) is plotted in blue, and the V_P profile from the Brocher (2005) relationship is plotted in green. The linear relationships for V_P agree with each other, and are consistent with the Brocher (2005) regression relationship.

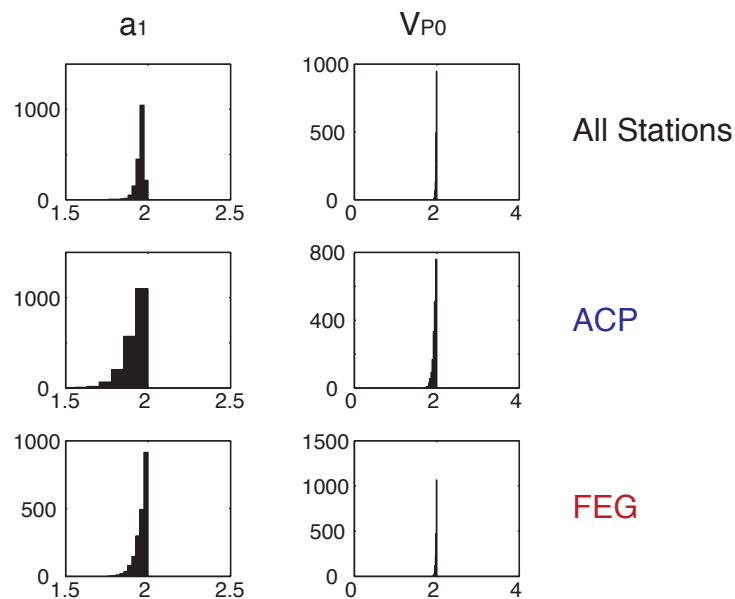


Figure 3.8– Parameters from linear VP profile inversion $b1$ and $VS0$ for all stations with basement thickness less than 2.5; ACP stations; FEG stations

3.5 Validation

Measurements of basin fundamental frequency presented in this study agree with values observed in regions with similar basin thickness (e.g. Parolai et al. 2002; Pratt, 2018;). For example, the basin fundamental frequency at station Y57A above a

shallow basin (0.12 km) has a fundamental frequency of 1 compared to ~ 1 Hz predicted in Parolai et al. (2002) and ~ 1.1 Hz measured from HVSR in Pratt (2018), while station 356A above a thick basin (1.16 km) has a fundamental frequency of 0.28 Hz compared to 0.3 Hz and from Pratt (2018). However, when shallow unconsolidated sediments are present within the basin, damaging amplification can occur at higher frequencies. Most studies of fundamental frequency in the ACP measure the large amplification at the fundamental frequency from these shallow layers, which ranges from 1.5-12 Hz (e.g. Fischer et al., 1995; Fairbanks, et al. 2008; Pratt et al., 2017). Amplification at these high frequencies from shallow unconsolidated layers may be large and damaging to shorter buildings and smaller infrastructure. However, in this study we focus solely on the peak amplification produced from basin/bedrock impedance contrasts, which may be larger and has implications for large buildings, and contributes to the overall basin shaking effect.

We could not identify any studies in the ACP that systematically map fundamental frequency of the entire basin, as opposed to the shallow sedimentary layers. Therefore, we carry out two different analyses to validate that our measurements of T_{ss} imply the same basin fundamental frequencies as would be obtained by traditional methods. We identify a set of teleseismic earthquakes that are recorded at three stations with increasing sediment thickness (**Figure 3.16**). We then compute radial and transverse component spectral ratios using a method similar to the E-HVSR technique, where the radial (R) and transverse (T) component multitaper power spectral density estimates are compared to the vertical (V) component multitaper

power spectral density estimates event-by-event, where the time-halfbandwidth product is 4. Peaks in these ratios correspond to the resonant frequencies of the sediment and are shown in *Figure 3.16*. In addition, we compute a “PRF spectral ratio” which is motivated by the SSR technique where multitaper power spectral density estimates at stations on sediment are compared event-by-event to the mean spectrum of stations on bedrock where the time-halfbandwidth product is 4. Here, we choose as our bedrock reference stations the 11 stations determined to be in the ACP, but that do not have significant sediment contributions, as pointed out in **DATA**. The “PRF spectral ratios” also exhibit peaks at frequencies corresponding to basin resonances and are plotted in *Figure 3.16*. For stations U60A, Q59A, and Q60A with basin thickness of 0.137 km, 0.534 km and 1.07 km respectively our T_{Ss} -based fundamental frequency estimates are 0.71 Hz, 0.39 Hz, and 0.26 Hz respectively. For these same stations, the E-HVSR and “PRF spectral ratio” techniques demonstrate that the peak amplification occurs at congruent frequencies. As expected, the fundamental frequency using measurements of T_{Ss} is consistent with the more traditional methods, show increasing fundamental frequency with increasing sediment thickness.

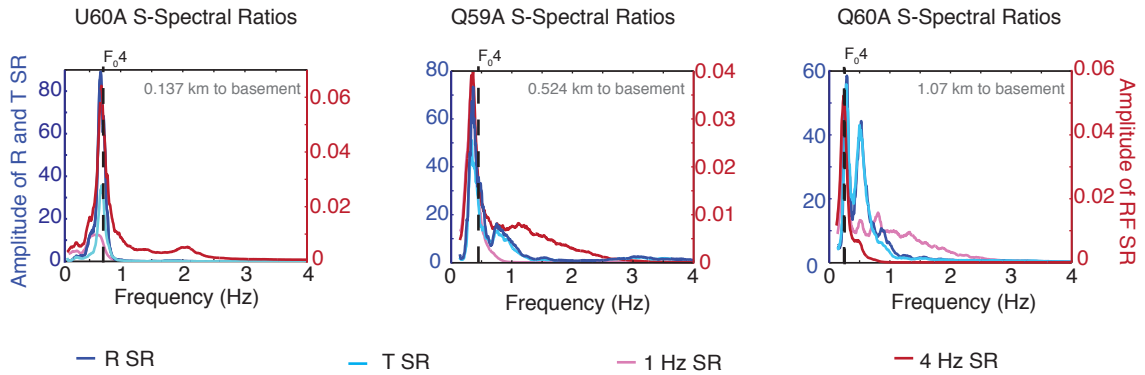


Figure 3.9- Comparison of site fundamental frequency (F_{04}) measurements obtained in this study compared to more traditional spectral ratio techniques of estimating site fundamental frequency from peak amplitude. HVSR techniques applied to Radial (R, dark blue) and Transverse (T, cyan) component data recorded at the seismic station. SSR techniques applied to PRF data for create "PRF spectral ratios" using 1Hz (pink) and 4Hz (red) PRFs. Method applied to three stations on differing basin thicknesses (U60A, Q59A, Q60A).

Using the S-reverberation and PP_{bs} arrival-time measurements made on high-frequency PRFs, we infer S and P wave velocity profiles for the ACP, for basin thickness thinner than 2.5 km. We find that S velocities increase with the square root of depth, starting at very low wavespeed at the surface (0.1 km/s) and increasing to about 3.5 km/s at 2.5 km depth. Our estimates of V_S at 0.1-0.5 km agree with previous studies of the average S-wave velocity of the ME, CP and Central United states basins of 0.45-0.67 km/s at the near surface (*Chen et al., 1996; Liu et al., 1997; Bodin et al., 2001*). We find that the P-wave velocity profile agrees well with that predicted by the Brocher V_P/V_S regression, starting at ~ 2 km/s at the surface and increasing to ~ 6 km/s at 2.5 km depth. Due to the fact that V_P is much greater than V_S in the shallow sediment (V_P/V_S is generally greater than 2), the P-leg of the PP_{bs} phase accumulates much less travel-time than the s-leg. Therefore, when using any

phase arrival visible on the PRF to infer V_P profiles, even small errors in picking can result in large errors in estimated V_P . We find that the average velocity profiles for FEG and CP groups of stations are consistent with each other, at least for the top 2.5 km of the basin; below 2.5 km the FEG basin is likely to consist of 2 or more underlying layers. This suggests that the CP and FEG strata above 2.5 km considered in this study are similar, which agrees with previous studies (*Cook et al., 1981; Pratt, 2018*). The velocities obtained at 2.5 km depth are relatively fast for sedimentary rock, but agree well with previous S and P velocity estimates at the same depth (*Cook et al., 1981; Dreiling et al. 2016*). These studies suggest a shallow reflector of sedimentary material with an average V_P of 2-3 km/s above a deeper and seismically faster Triassic basin with an average $V_P = 4.5-5$ km/s (*Herrman, 1979; Cook et al., 1981*). The velocity estimates from our V_P profiles at the very near surface of 2km/s are fast when compared to previous studies in the ACP V_P , which suggest that V_P at the very near surface (< 2 m) is around 1.4 km/s (*Yantis, 1983; Chapman, 2003; Wells et al. 2015*); the difference is likely due to the limited resolution of our 4 Hz RFs at the very near surface, where our method is likely to average velocities in the upper ~100 m. The ~6 km/s velocity at 2.5 km that our models obtain agree well with studies which predict that thick sediment layer may exist (>1 km) with V_P of 6 km/s (*Langston and Horton, 2014; Dreiling et al. 2016*).

We further validate our velocity profiles by comparing the amplitudes of r_0 and PPbs measured directly on the PRF with amplitudes from the reflection/transmission coefficients calculated using the velocity profiles obtained above. Having found that

Brocher V_P/V_S scaling relationships are compatible with the data, we use density- V_S relationships to construct density profiles for the ACP. Together with crustal parameters of $V_P = 6.7$ km/s and density = 2.69 g/cm³ from NGA East (*Drieling et al., 2016*), we use our V_P , V_S , and density profiles to calculate reflection and transmission coefficients for PP_{bs} and the SS reverberation (r_0) at each depth using expressions from Aki and Richards (1980). For thin portions of the basin (< 0.5 km), the calculated $\hat{S}\hat{S}$ reflection coefficients have similar amplitude as the measured $-r_0$ at each station (**Figure 3.17A**), suggesting that the S-velocity profiles obtained are not only consistent with amplitude measurements not used in the inversion, but also that they may be expected to yield reasonable amplitude predictions when used in wave simulations. For thicker basins (> 0.5 km), measured amplitudes tend to be somewhat higher than those predicted by our velocity profiles, suggesting that there may be multiple small layers of sediment in the deeper portion of the basin. The relatively large variability in measured r_0 likely reflects variability in the lithology of the bedrock amalgamated in past collisions and accretionary events (*Wagner et al., 2018*). The PP_{bs} reflection coefficient is related to the $\hat{P}\hat{P}_0$ reflection at the free surface multiplied by the $\hat{P}\hat{S}$ reflection coefficient at the basin/bedrock interface. We find that the $\hat{P}\hat{P}_0 \cdot \hat{P}\hat{S}$ amplitude predicted by our ACP velocity profiles fits the measured PP_{bs} amplitudes (**Figure 3.17B**), except for thinnest basins (< 0.15 km), where the PPs phase gets amplified from merging with the Ps phase. The agreement between measured and predicted PP_{bs} amplitudes provides independent validation of our P-velocity profile, and supports our finding that Brocher scaling relationships are appropriate for used in the ACP.

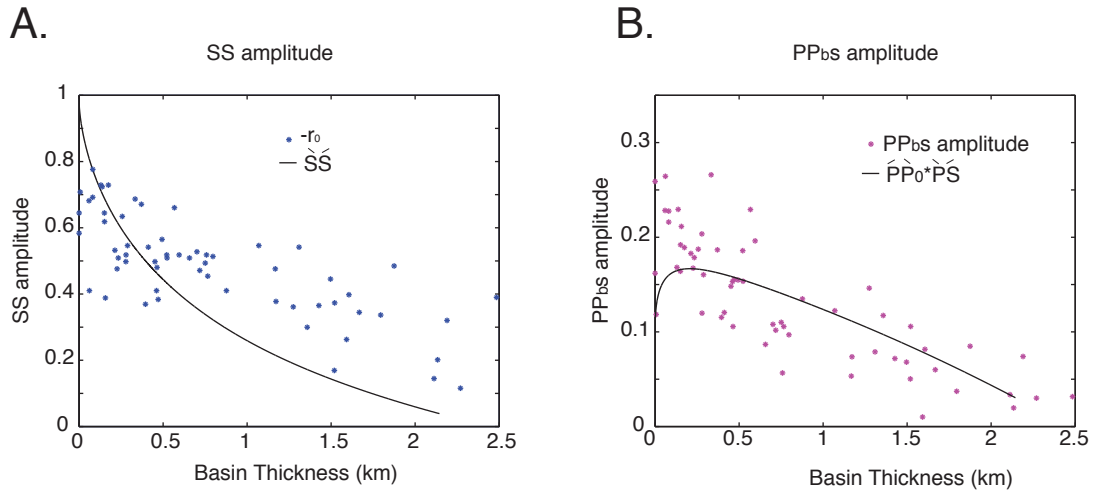


Figure 3.17 – Amplitude measurements from PRFs compared to calculated reflection/transmission coefficients for the sediment velocity models obtained in this study using Aki and Richards (1980). Sediment density calculated using the Brocher (2005) relationships; crustal parameters are obtained from Drieling et al. (2016). **A.** r_0 measurements (blue circles) compared to calculated $\hat{S}\hat{S}$ reflection coefficients (black line) for a range of basin thickness. **B.** Measurements of PP_{bs} (pink circles) compared to calculated $\hat{P}\hat{P}_0 \cdot \hat{P}\hat{S}$ reflection coefficients (black line) for a range of basin thickness.

3.6 Discussion of ACP results

In large regions like the Atlantic Coastal Plain, where broadband seismic stations have been installed but regional seismicity is rare, obtaining basin structure constraints using more traditional methods developed for regions with an abundance of seismicity may prove challenging. High-frequency P-to-S receiver functions provide an underutilized approach for constraining the basin fundamental frequency and velocity profiles using teleseismic events.

Traditional SSR or HVSR techniques to measure site-specific basin properties rely on local earthquakes or the ambient noise field. The lack of widespread seismicity on the

ACP, requires that passive seismic techniques are used. While ambient noise techniques have shown great promise in improving data coverage in largely aseismic areas, the accuracy of the retrieved Green's functions depends on assumptions about the isotropic distribution of noise sources and stationarity of the signal (*e.g. Yao et al. 2009; Tsai, 2009*). In the ACP, the dominant source of the seismic noise is the Atlantic Coast (*e.g. Koper and Burlacu, 2015*), resulting in a highly anisotropic noise wavefield. This anisotropy can introduce bias into phase and group velocity measurements made from ambient noise cross-correlations.

Because receiver functions are calculated from teleseismic events, and do not rely on local earthquakes or ambient noise, existing broadband station deployments (such as USArray) can be used to characterize site-specific basin fundamental frequency and regional velocity profiles across large geographic areas without relying on local earthquake events or ambient noise measurements. When the velocity contrast is significant, and the sedimentary layer is thick (greater than 0.1 km), phase arrivals are large and visible on the mean PRF with arrival times that increase, as expected, with increasing sediment thickness. However, relatively low frequency bandpass corners of 0.5 - 1 Hz typically used in PRF studies of crustal structure are insufficiently high to distinguish between and interpret different phase arrivals (particularly P_{bs} and PP_{bs}) when sediment is less than 1 km thick, as is the case across much of the ACP (see **Figure 3.18**). Here, we show that much higher frequency signals can be reliably extracted from teleseismic PRFs, enabling the characterization of sediments as thin as 0.1 km. In regions where broadband stations have not been deployed or coverage is

insufficient, receiver functions can be calculated from nodal array deployments (e.g. Ward and Lin, 2017; Liu et al. 2018), which have optimal sensitivity in the frequency range of interest. Indeed, the ease of deployment and low cost of nodal deployment also enable targeted, detailed mapping of sedimentary basins based on PRF technique.

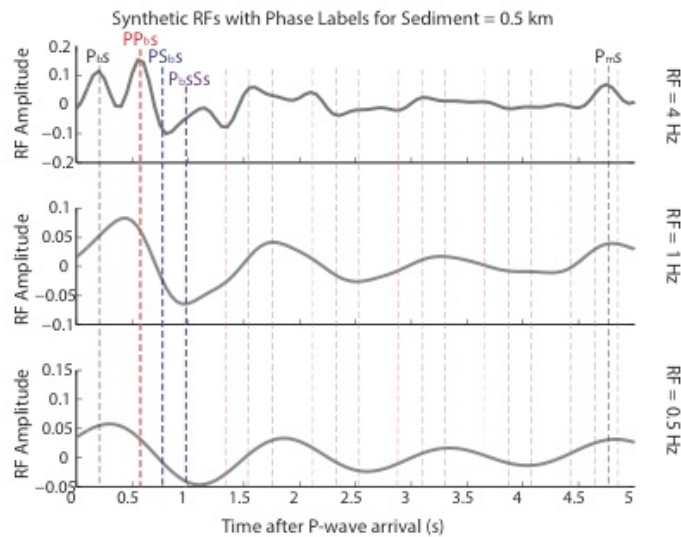


Figure 3.18 – Synthetic PRFs calculated for a 0.5 km thick sediment. In order to distinguish between the Pbs and PPbs phase arrivals, High frequency PRF (with high corner frequency of 4Hz) must be used.

PRFs are most often used to map interfaces within the deep crust and underlying mantle. However, interpreting PRF signals from deeper structures often requires accounting for signals due to sedimentary basins (**Chapter 2**), yielding useful constraints on sediment structure as a byproduct. S-reverberation time (and basin fundamental frequency) must be estimated when constructing shallow-layer reverberation removal filters, and Ps phases must be identified when applying shallow-layer corrections to H-k stacks. Therefore, velocity profiles can be calculated whenever PRFs are used in regions with significant sedimentary cover. While

requiring more labor than traditional SSR or HVSR techniques, high frequency PRFs may be useful in constraining basin properties over large areas especially in regions with low or intermittent seismic activity.

3.7 Conclusions

Receiver function analysis of teleseismic events recorded at broadband seismic stations from USArray places constraints on basin fundamental frequency and velocity profiles. We constrain these basin properties across the Atlantic Coastal Plain from phase arrivals on high-frequency (4 Hz) P-to-S receiver functions. From measurements of the two-way S-wave travel time on the receiver function, the basin fundamental frequency is mapped across the ACP. While shallow sediment structure may result in even higher fundamental frequencies, the basin fundamental frequencies presented in this work are consistent with basin thickness and results from applying more traditional techniques to teleseismic data. In addition to providing site-specific fundamental frequencies, the relationship of T_{Ss} (or fundamental frequency) and basin thickness may provide a method to estimate the expected fundamental frequency at any basin thickness for thick sedimentary basins. The amplitudes measured on the RFs match expected patterns with increasing basin thickness. ACP and ME strata used in this study share a similar high velocity profile for V_S until about 2.5 km thick, implying that above this depth, they share similar basin structure. The V_S profile increases as the square of depth, while V_P profiles for the ACP and ME are fit well using the Brocher regression fit. The receiver function amplitudes at the phase arrival times validate the high velocity V_P and V_S profiles.

Chapter 4: Crustal and Lithospheric Structure in the Southeastern US using Receiver Function Common Conversion Point (CCP) Stacking

4.1 Introduction

The Southeastern United States (SEUS) lies on the passive eastern North American margin and preserves a long geologic record of continental collision, rifting, and volcanism. The multiple episodes of continental collisions have left a chaotic assortment of accreted terranes and faults. The lithospheric structure reflecting these accreted terranes documents the evolution of the SEUS, where lithospheric thickening indicates the locations of past compressional or collisional events and lithospheric thinning suggests a past extensional or rifting events. Constraining the geographic extents of these lithospheric variations will help clarify the tectonic history of the region.

The dense deployment of the USArray Transportable array seismic network allowed for seismic imaging of the often-neglected passive margin with higher resolution than ever before. Despite the numerous studies that investigate the lithospheric structure of the SEUS (e.g. *Parker et al. 2016; Biryol et al. 2016; Hopper et al. 2017; Lynner and Porrit, 2017; Soto-Cordero et al., 2018; Wagner et al., 2018*) questions about the underlying large-scale structures remain. For example, some studies have found evidence for a low velocity ‘mid-lithospheric discontinuity’ (MLD) beneath the Appalachian Mountains (*Abt et al. 2010; Long et al., 2017*), while others suggest that the MLD and LAB coincide in depth in this region (*Liu and Gao, 2018*). While the existence of a low velocity discontinuity at 80-120 km has been well documented in

continental cratons, mechanisms controlling this MLD have remained elusive with explanations spanning the rheological, chemical, and mechanical realm.

Even the base of the lithosphere-asthenosphere boundary (LAB) is not well constrained across the SEUS. While most receiver function studies find that the LAB beneath the Piedmont shallows to 100-120 km depth (*Wagner et al. 2018, Hopper and Fischer, 2018*), recent magnetotelluric studies suggest the lithosphere in the same region can be no thinner than 200 km (*Murphy and Egbert, 2017*).

The multiple continental collisions undergone in the SEUS left a complex crustal structure, complicating the imaging of deeper structure. SRF CCP stacking has shown evidence of multiple crustal layers of crustal emplacement on Laurentian basement during past collisional events, indicating that past Proterozoic tectonics in the region may have been analogous to modern tectonics. Seismic imaging of complicated fault structure in the Blue Ridge beneath seismically active zones in Tennessee has pointed to additional layering at mid-crustal depths trending both south-southeast (*Bobyarchick, 1998; Culotta et al., 1990, Wagner 2012*) and north-northwest (*Culotta et al., 1990; Wagner 2012, Powell et al., 2016*). These mid-crustal layers may be evidence of crustal emplacement during a separate orogeny and may be related to the underlying seismicity.

Despite its distance from active margin tectonics, the SEUS contains multiple zones of seismic activity capable of producing damaging earthquakes. Because large earthquakes in this region occur infrequently, little is known about the mechanisms

controlling the locations and magnitudes of these events. The seismogenic zones are dispersed throughout the SEUS and include the central Virginia seismic zone (CVSZ), the Eastern Tennessee seismic zone (ETSZ), and the South Carolina seismic Zone (SCSZ) (**Figure 4.1**). Previous studies have suggested that stresses that control intra-plate seismogenic zones are correlated with boundaries between accreted terranes and variations in deeper earth structure. Specifically, these seismogenic zones have been found to correlate with abrupt changes in thickness of the tectonic plate (lithosphere) (*Biryol et al., 2016*), a weak intra-lithospheric layer (*Thybo et al., 2000*), and sharp changes in thickness of the continental crust (*Soto-Cordero et al., 2017*). We explore these hypotheses by systematically mapping variations in lithospheric structure using CCP stacks beneath regions of seismicity and seismic quiescence, looking for structural patterns that may highlight which mechanisms play a role in controlling the location of passive margin seismicity.

Receiver functions have proven extremely useful in constraining crustal and lithospheric variations, as they are particularly sensitive to sharp changes in the elastic parameters. P-to-s receiver functions (PRFs) isolate S-wave conversions produced across impedance contrasts beneath a seismic station, and the relative phase arrival times can be used to constrain the deeper structure. Similarly S-to-p receiver functions (SRFs) isolate P-wave conversions produced across impedance contrasts. PRFs contain higher frequency energy are thus preferred to constrain structure variations since they are able to provide higher vertical and horizontal resolution. However, reverberations produced within low-velocity shallow layers, such as sedimentary basins, can contaminate traditional PRFs (*Yeck et al. 2013, Yu et al.,*

2015, Schulte-Peklum et al., 2017). In the SEUS, sedimentary basins cover most of the region, making interpretations of lithospheric structure from PRFs nearly impossible. We remove large amplitude sedimentary reverberations by applying a resonance removal filter and creating reverberation-removed PRFs (e.g. Yu et al., 2015; Cunningham and Lekic, 2019). Common conversion point (CCP) stacking of receiver functions is a useful tool to image lithospheric structure variations across an array (e.g. Dueker and Sheehan 1997; Gilber et al. 2003; Frassetto et al., 2010). CCP stacking uses a velocity model to migrate the relative arrival times of converted phases to depth and lateral locations beneath the station. We calculate reverberation-removed PRFs CCP stacks across the SEUS to look for structure variations at relatively high resolution. SRFs are not contaminated by sediment reverberations in the same way as PRFs; therefore, we calculate complimentary SRF CCP stacks which provide a relatively low resolution view of lithospheric structure across the region. Using both the sediment removed PRF and SRF CCP stacks, we constrain the crustal and lithospheric structure beneath the SEUS. We focus our investigations on identifying crustal and lithospheric thickness variations, any evidence of accreted terranes preserved as intra-lithospheric or intra-crustal layering, and identifying correlations between lithospheric structure variations and seismicity.

4.3 Receiver Function Data for Common Conversion Point (CCP)

Stacking

For this study, we calculate PRFs and SRFs for station in the Southeastern United States. Locations of 236 stations from the USArray Temporary Array between 30 - 42.25N and 86.5 - 73.5W are shown in **Figure 4.2**.

Data is collected from the IRIS DMC for earthquakes before January 1, 2018 with $M_w > 5.5$ and epicentral distances between 30 and 90 for PRFs and between 55 and 80 for SRFs (*Wilson et al., 2006*). The events are quality controlled, requiring a minimum Z-to-R cross correlation of 0.3 and a maximum difference of 25 seconds between observed and predicted arrival times. The RFs are calculated following the automated procedure detailed in Abt et al. (2010), where the waveforms are projected onto the P-SV-SH system using the free surface transform matrix and finding the surface velocity that minimizes the amplitude of the parent wave (P for PRFs and S for SRFs) on the daughter component. A fourth order band-pass filter is applied to waveforms of 0.03-1Hz (for 1Hz PRFs), 0.03-4Hz (for 4Hz PRFs) and 0.03-0.5Hz (for SRFs). Using the time-domain deconvolution of Ligorria and Ammon (1999), we calculated the RFs with Gaussian half-amplitude half-width of ~ 0.12 s to calculate the 4Hz PRFs, of ~ 0.5 s to calculate the 1Hz PRFs, and of ~ 1 s to calculate the SRFs. We find a median of 93 PRFs and between 80 SRFs per station (**Figure 4.2**). We choose the time domain deconvolution over frequency domain deconvolution technique as the damping or regularization parameter added to stabilize the frequency-domain deconvolution results in less-detailed RFs with stronger side-lobes (*Lekic and Fischer, 2017*).

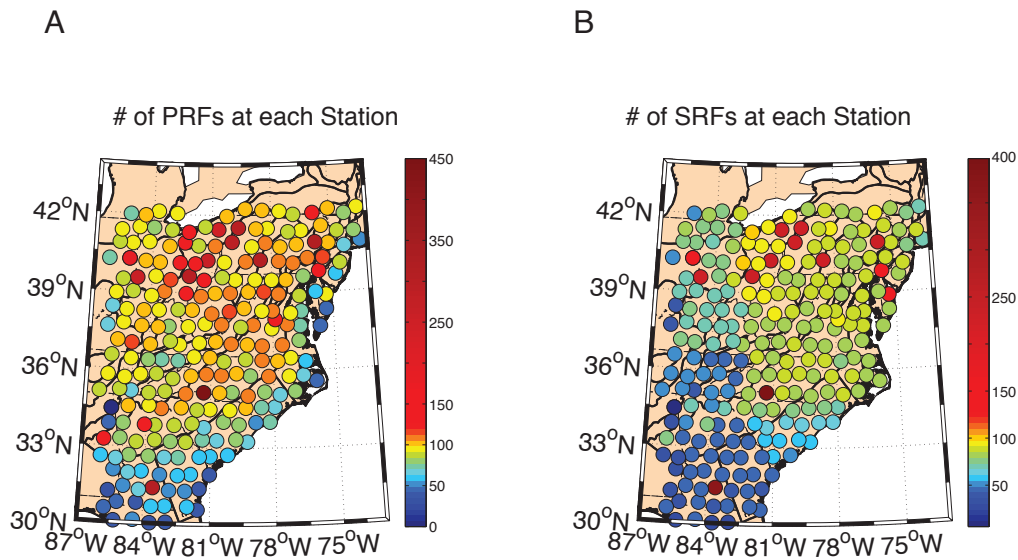


Figure 4.1- The locations of USArray TA stations used in this study colored by the number of P-to-s (A) and S-to-p (B) receiver functions calculated at each station. Dark red circles are stations that have been deployed for a longer time.

4.4 Common Conversion Point (CCP) stacking

4.4.1 CCP stacking overview

When considering the structure beneath an array, RFs are often combined using common conversion Point (CCP) stacking to create a 3-D image of the subsurface. CCP stacking takes advantage of the range of source events and receivers, projecting individual RF amplitudes to depth along their ray path and backazimuth using a velocity model and stacking them in volumetric bins, which suppresses noise present on individual RF traces. The velocity model used to migrate the RFs from time to

depth can be a general 1-D reference model such as ak-135 (*Kennett et al., 1995*) or can be modified to include measured crustal values obtained from H- stacking (*Zhu and Kanamori, 2000*). The velocity model we use in this study is based on crustal values obtained from SRTC H-k- V_p stacking of PRFs and SRFs (discussed in section 3.2 below).

CCP stacks are calculated following the method detailed in the supplement of *Lekic and Fischer (2011)*, where the stack at each depth (z_k) and latitude-longitude location is calculated as the weighted average of the individual RFs at that point. The weighting factor (γ) depends on the cubic spline at the horizontal distance (Δ) of each migrated ray from the CCP stack point. The horizontal distance of each migrated ray at depth (Δ) is normalized by the knot spacing of the cubic spline (Δ°), which increases as a function of depth written in terms of the wavelength (λ) at each discrete depth (z_k):

$$(4.1) \quad \Delta^\circ = \frac{1}{2} \sqrt{\left(\frac{\lambda}{2} + z_k\right)^2 - z_k^2} .$$

The weighting factor γ of each individual RF contributing to the CCP stack at a given point is calculated as:

$$(4.2) \quad \gamma(\Delta) = \begin{cases} \frac{3}{4}\bar{\Delta}^3 - \frac{3}{2}\bar{\Delta}^2 + 1, & \bar{\Delta} \leq 1 \\ \frac{1}{4}(2 - \bar{\Delta})^3, & 1 \leq \bar{\Delta} \leq 2 \\ 0, & \bar{\Delta} > 2 \end{cases}$$

where $\bar{\Delta} = \Delta / \Delta^\circ$. Therefore, if the migrated RF is spatially close to a given location in the subsurface volume, the weighting factor is close to 1, while at distances of $\frac{\lambda}{2}$ the weighting factor will tend toward 0. The weighting factor $\gamma(\Delta)$ has the effect of horizontally smoothing physical structure through the zero offset Fresnel zone half-width; as depth increases, the Fresnel zone half-width (and effectively the smoothing length scale) increases. The benefit to using this type of weighting or smoothing method is that it reduces the possibility of over-smoothing and losing sub-Fresnel zone structure (*Lekic and Fischer, 2017*).

PRFs contain higher frequencies than SRFs and so near the station the horizontal distance becomes too small; for this reason PRF CCP stacks have a Δ° set to 50 for all depths and will demonstrate both higher vertical and horizontal resolution than SRFs. PRFs will be able to image sharp lateral variations better than SRFs, but are more sensitive to contamination by shallow layer multiples. For this reason, we calculate and compare the results from both PRF and SRF CCP stacks through the SEUS.

The CCP stacking volume for both PRFs and SRFs is discretized by 0.5km in depth, and 0.25° in latitude and longitude. The results of CCP stacking are shown as both N-S and W-E cross-sections through the stack volume (*Figure 4.3*).

Common Conversion points and cross sections

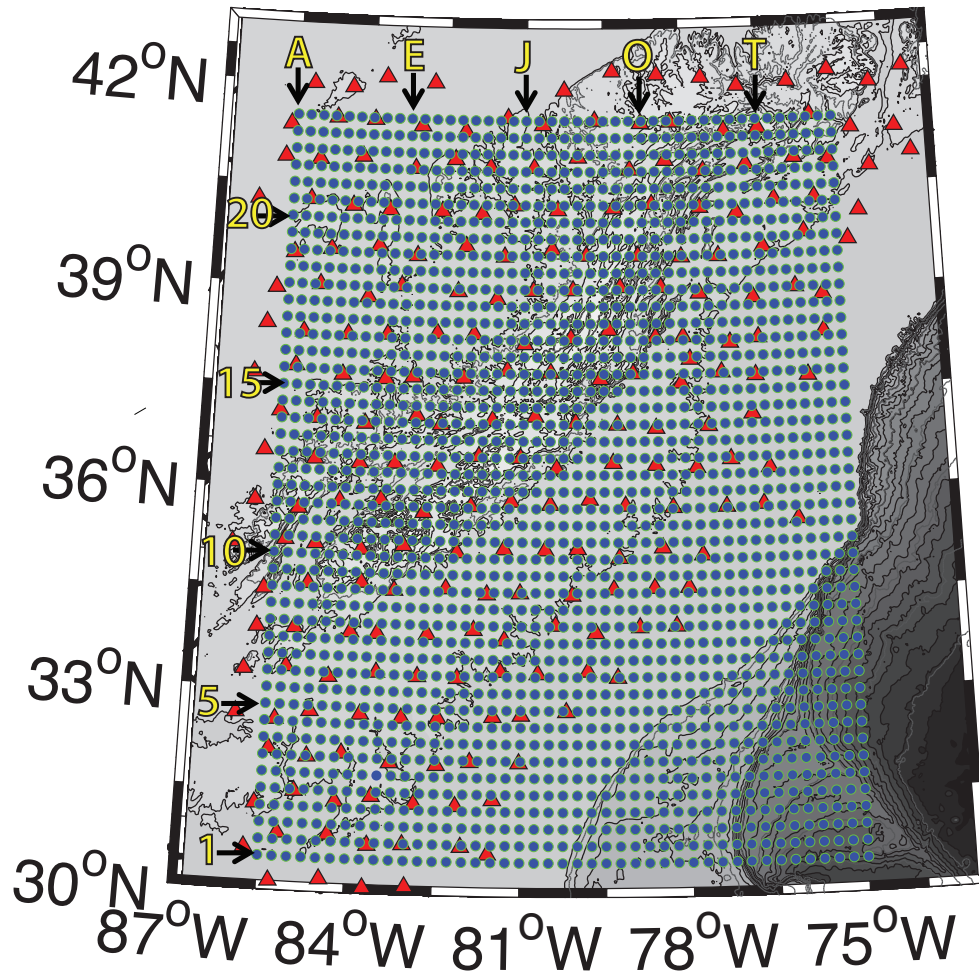


Figure 4.2- Locations of CCP stacking points (blue) and stations (red triangles). Cross sections shown are calculated along vertical and horizontal lines in the grid. Each cross section number indicates a W-E cross section, while letters indicate a N-S cross-section.

4.4.2 Regional Velocity Model with SRTC H- κ - V_p Stacking

Common conversion point (CCP) stacking requires that the individual RFs be migrated from time to depth using a velocity model of the subsurface. While global models such as ak-135 can be used, errors in the velocity structure lead to errors in depth in the CCP stack (Hopper *et al.*, 2017). To alleviate errors associated with an incorrect velocity model, we calculate a velocity model for the SEUS based on crustal thickness and velocity parameters obtained at each station through an H- κ - V_p stacking technique.

Traditional H- κ stacking uses predicted arrival times of converted phases on the PRFs to constrain the velocity beneath the seismic station assuming an average crustal P-wave velocity (Zhu and Kanamori, 2000). However, an incorrect assumption of average crustal V_p for a region can lead to error of up to 10 km in crustal thickness (H) and 0.4 in V_p/V_s ratio (κ) (Figure 4.4). Because both PRFs and SRFs have some sensitivity to average crustal P-wave velocity (V_p), combining them into H- κ - V_p will constrain all three crustal parameters (e.g. Rychert and Harmon, 2016).

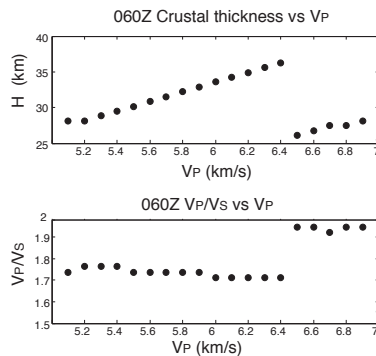


Figure 4.3- The velocity assumption in H- stacking is extremely important and can significantly change inferred crustal properties. Results from traditional H-k

stacks calculated for station 060Z on Atlantic Coastal Plain sediments. Top. As the assumed average crustal V_P velocity used to calculate the stacks increases, the crustal thickness estimate increases until a new maximum is inferred (at 6.5 km/s). Bottom. As the assumed average crustal V_P increases, the V_P/V_S ratio (or κ) decreases, until again a new maximum is inferred.

In regions with a low-velocity sediment layer, such as the Atlantic Coastal Plain (ACP), crustal signal in PRFs is often contaminated by sediment multiples (Yeck *et al.*, 2013; Yu *et al.*, 2015; Schulte-Pelkum *et al.*, 2017). For this reason, we calculate sediment removed (SR) PRFs for stations with sediment reverberation contamination. The SR PRFs are calculated following the method detailed in Chapter 2, where a resonance removal filter is constructed to remove the oscillatory reverberation signal. The filter is constructed using measurements of the two-way travel time of the S-wave in the sediment (Δt) made from the autocorrelation of the mean PRF. To correct for time delays introduced from a slow sedimentary layers, the arrival time of the PP_{bs} phase (δtP) made on the high-frequency (4Hz) PRF as it depends on both V_P and V_S of the sedimentary layer. Measurements of Δt and δtP are made at each station with sediment reverberations (**Figure 4.5**).

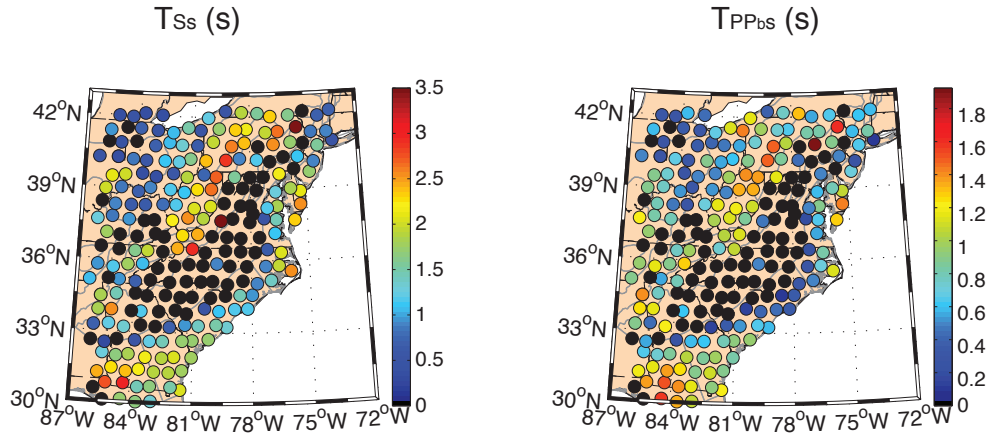


Figure 4.4- Measurements of sediment phase arrival times at each station. The two way S-wave travel time in sediment (left) and the arrival time of the PP_{bs} phase (right) are shown. In regions with thicker sediment, both T_{Ss} (Δt) and T_{PPbs} (δtP) are large, while in regions with thinner sediment T_{Ss} and T_{PPbs} are small. Stations in black do not demonstrate a sedimentary signal in the receiver functions.

When the SR PRFs and sediment time-delay corrections to each phase are used to calculate a stack over a range of input H , κ and V_p values, we call this sediment removed time-corrected (SRTC) H - κ - V_p triple stack. The equation for a (SRTC) H - κ - V_p triple stack (s) using the predicted P_{ms} , PP_{ms} , and $PS_{ms}+P_{ms}P_{ms}$ phase arrival times ($t_{P_{ms}}$, $t_{PP_{ms}}$, $t_{PS_{ms}} + t_{P_{ms}P_{ms}}$ respectively) for N number of PRFs computed a station $f_j(t)$ and the predicted S_{mp} phase arrival time ($t_{S_{mp}}$) for N_S number of SRFs computed at the same station $f'_j(t)$ is written as:

$$(4.3) \quad s(H, \kappa, V_P) = \sum_{j=1}^N w_1 f_j(t_{P_{ms}} + \Delta t - \delta t P) + w_2 f_j(t_{P_{P_{ms}}} + \delta t P) - w_3 f_j(t_{P_{S_{ms}}} + t_{P_{mSP_{ms}}} + \Delta t) + \sum_{j=1}^{N_S} f'_j(t_{S_{mp}} + \Delta t - \delta t P) +$$

where w_1 , w_2 , and w_3 are the relative weights of the three PRF phases (set to 0.7 0.3 and 0.1 respectively).

We calculate the triple stack over a range of H, κ and V_P values where H ranges from 20 to 60 km and κ from 1.5 to 2. In chapter 2, we found that even by combining sediment removed time corrected PRFs, SRFs, and the post-critical reflection at the Moho (SsPmp) the V_P obtained from the triple stack is not well constrained. Therefore, we restrict or search for average crustal V_P to values within +/-0.2 km/s of values predicted by Crust2.0 (*Bassin et al., 2000*). The SRTC H- κ - V_P triple stacks provide an estimate of the crustal thickness (H), V_P/V_S (κ) and crustal V_P beneath each station (**Figure 4.6**). The velocity model used to calculate the CCP stacks is then updated to include the new crustal parameters. The new velocity model should help constrain the correct depths to layers in the CCP stacks.

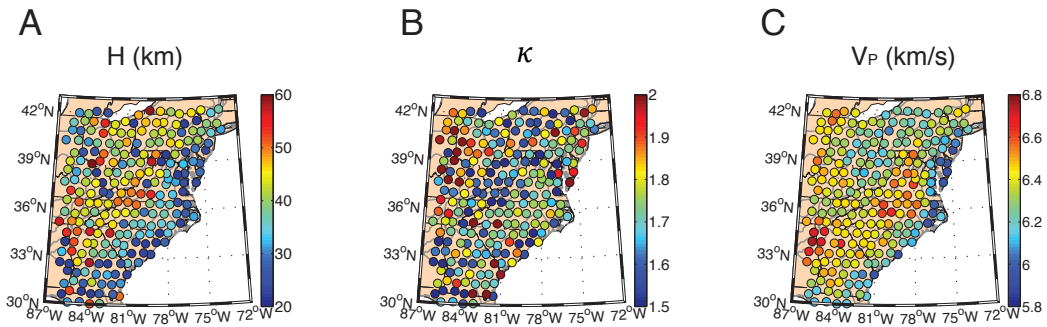


Figure 4.5- Values of crustal H , κ , and V_P for each station in our study area obtained from H - κ - V_P stacking method (described in text). These parameters are used to calculate a velocity model for the migration of RFs from time to depth in the CCP stack

4.4.3 Sediment Removed PRF CCP stacks and SRF CCP stacks

We calculate SR PRF CCP stacks for the SEUS using the velocity model produced using our H - V_P stacking approach. CCP stacks should help mitigate the effects of sediment reverberations, as the near vertical reverberations are not expected to constructively stack at Moho depths when individual RFs are migrated along ray path and backazimuths. However, near the edge points of a seismic array, too few RFs from different source and receiver paths may cause reverberations to become visible. In addition, if sediment reverberations directly overprint the P-to-s wave arrival from the Moho, CCP stacking will not be able to constrain crustal and lithospheric structure and sediment reverberations may still be visible in the stack (**Figure 4.7A**).

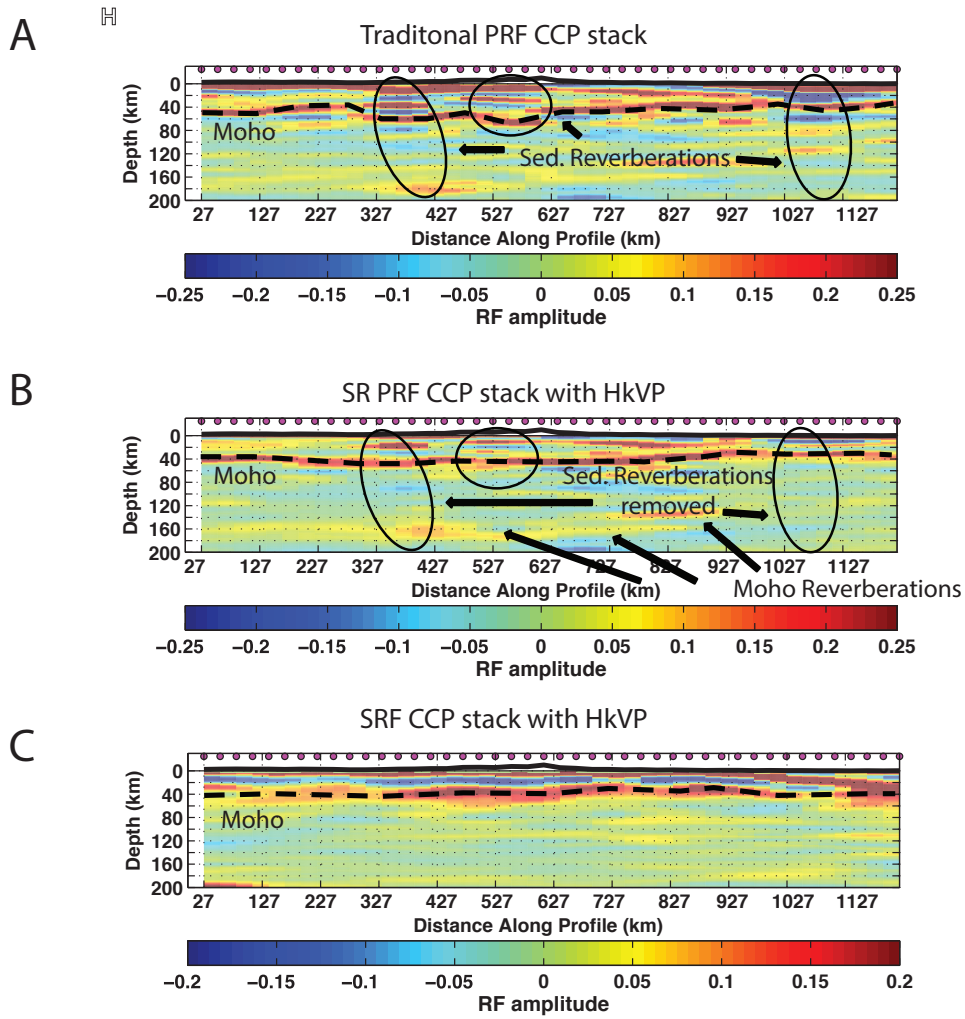
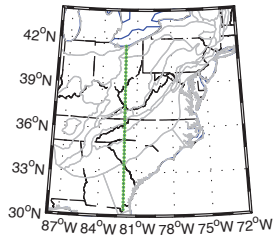


Figure 4.6- Results of CCP stacking for cross-section H (location shown in top panel of figure). Red indicates positive RF amplitude associated with a velocity increase with depth while blue indicates negative RF amplitude associated with a velocity decrease with depth. A. In traditional PRF CCP stacking we

see large amplitude sediment reverberations that create a Moho step at about 327 km along the profile B. Sediment removed (SR) PRF CCP stacks remove much of the sediment reverberation contamination in the regions highlighted and show a flat Moho at 327 km along the profile. C. SRF CCP stacks show a similar Moho profile to SR PRF CCP stacks, but have lower resolution.

To improve upon traditional CCP stacking techniques, we use sediment removed (SR) PRFs calculated in section 4.2. Before the resonance removal filter is applied, the mean PRF at two example stations on ACP sediment show large amplitude oscillatory signal (Gray line – **Figure 4.8**). After the resonance removal is applied, a small positive amplitude peak emerges between 4-5 seconds, which is likely to be the $P_{m,s}$ arrival from the Moho. When the SR PRFs are used in CCP stacking, the oscillatory pattern seen on the edges of the stack and beneath the ACP sediments is reduced (**Figure 4.7B**). Although the $P_{m,s}$ phase amplitude appears small and weak on the individual RFs, when migrated to depth, the $P_{m,s}$ phases coherently stack together producing a strong Moho signal.

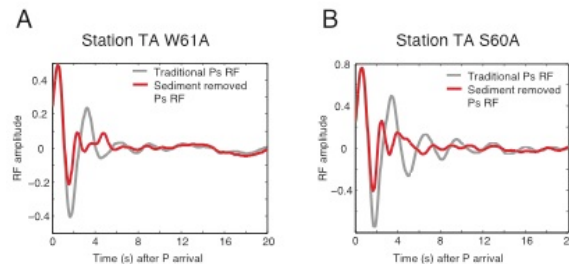


Figure 4.7- Examples of the resonance filter applied to PRFs. Gray is the mean of the PRFs before the resonance removal filter is applied, red line shows the mean of the PRFs after the sediment is removed. A. Station W61A in New Bern, NC. Before the sediment is removed, no clear Moho phase arrival ($P_{m,s}$) exists in the RF. After the sediment is removed, a small amplitude peak appears at ~5s which is likely the Moho arrival. B. Station S60A in Water view, VA. Again, before the sediment is removed, no clear Moho phase arrival ($P_{m,s}$)

exists in the RF. After the sediment is removed, a evidence of a Moho arrival appears between 4-5 s.

Additionally, below the Moho on the SR PRF CCP stacks, additional positive and negative phases appear that are not seen in the traditional PRF CCP stacks. These phases are not in fact lithospheric structure, but instead are the Moho-related multiples. Therefore, we restrict our interpretation to depths shallower than the PpPs Moho phase

At greater depths, we look to SRF CCP stacks to constrain the lithospheric structure since Moho reverberations do not contaminate SRFs (*Figure 4.7C*). SRF CCP stack shows a broad crust in at the same depths as the SR PRF CCP stacks. The broad structure is due to the lower frequency content of S-waves, which explains the decrease in vertical resolution. No strong negative amplitude in the lithosphere is visible on the SRF CCP stacks, which means that the lithosphere asthenosphere boundary in the SEUS either extends much deeper than previous seismic studies suggest, or that the boundary between the lithosphere and asthenosphere in beneath the SEUS is not a sharp impedance contrast, but rather a gradational boundary.

4.5 Results and Observations

Using the sediment removed PRF and SRF common conversion point stacks, we map the vertical and lateral variations in lithospheric structure beneath the Southeastern United States. Specifically, we investigate evidence of past collisional events and inherited structures and look for correlations between deeper structure and seismicity in the SEUS. In this section, we present selected cross-sections required for

discussion; however, cross-sections through the total CCP stacking volume for the entire SEUS are shown in **Appendix**. Letters starting with A in the west and V in the east note the location of north to south (N-S) cross-sections. Numbers starting with 1 in the south and 23 in the north note the locations of east to west (E-W) cross-sections.

4.5.1 Crustal Thickness

When the CCP stacks are plotted in cross-section, the most notable feature is the large amplitude positive phase between 30-60 km depth (*e.g. Figure 4.9*). A positive phase implies a velocity increase with depth. The positive phase seen on our CCP stacks is correlated with the overlying topography (shown on cross-sections with 10x vertical exaggeration), where high topographic regions parallel increases in the depth of the positive phase. Based on the depth, amplitude and depth correlation with expectations from isostasy, we interpret the positive phase between 20-60 km to be the boundary between the crust and the mantle (Moho).

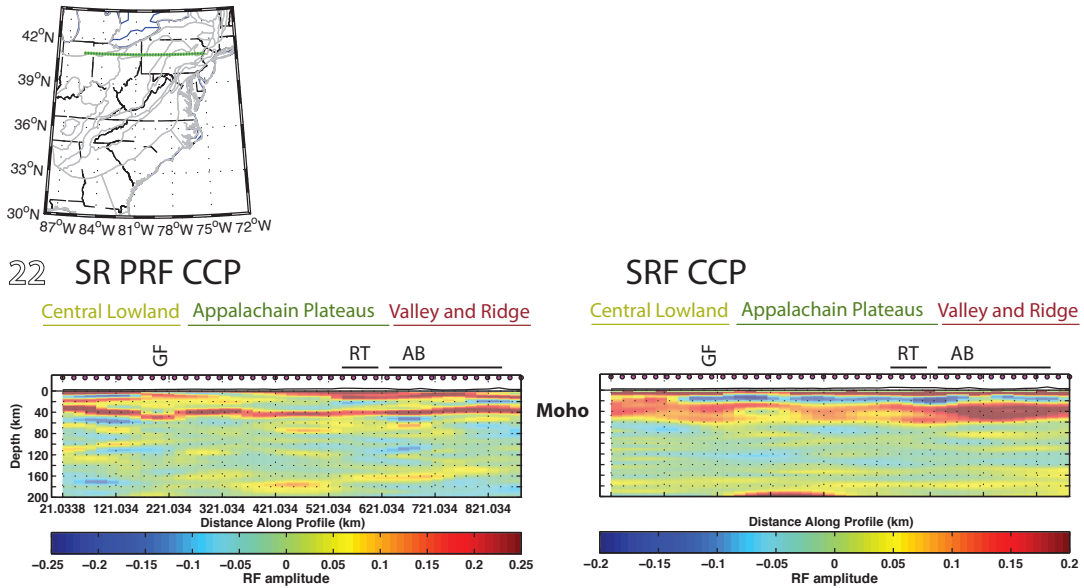


Figure 4.8 - Figure 9- W-E Cross-section 22 showing a strong positive (red) arrival between 35 and 45 km depth. Right is the sediment removed (SR) PRF CCP stack and left is the SRF CCP stack. Stacks below show the variance of the RF amplitude at each point in the CCP stack. We interpret this positive Labels in black are features from Figure 1 that the cross sections pass through. RT= Rome trough, GF= Grenville front, SGR = South Georgia rift, ETSZ = eastern Tennessee seismic zone, BFZ = Brevard fault zone, CPS= central Piedmont suture, NCSQ = North Carolina seismic quiescence, AB = Appalachian basin, SCSZ = South Carolina seismic zone, SSZ = Suwanee suture zone, CVSZ = central Virginia seismic zone. Colored labels above each cross section denote the physiographic province that the cross sections pass through. CL = Central Lowland; AP = Appalachian Plateau, V&R = Valley and Ridge, BR = Blue Ridge, ACP = Atlantic Coastal Plain, LP = Interior Lower Plateau.

The Moho depth is picked beneath each CCP cross-section, (both N-S and E-W). This allows for a birds eye view of the Moho depth (**Figure 4.10**). We find regions of very thick crust beneath the valley and ridge, Blue Ridge, and Appalachian Plateau physiographic provinces (*Fenneman, 1928*) with thinner crust closer to the Atlantic

Coast. The sharp crustal thickness change on the western portion of our map seems to follow a similar trend as the predicted Grenville Front (GF). When compared to our previous estimates of crustal thickness from H-k-V, triple stacks (*Figure 4.6*), the crustal thickness from CCP stacking is smoother and deeper. The crustal thickness from CCP stacks is smoother due to the lateral smoothing that arises from stacking the SR PRFs along their ray paths and backazimuths. We find the thickest crust beneath the Eastern Tennessee Seismic Zone (ETSZ) of around 63 km. While a 63 km crust is reasonable in active continent-continent orogenic regions such as Himalaya (*Vera Schulte Pelkum et al., 2005*) it is an unusually thick estimate for crustal thickness in the SEUS.

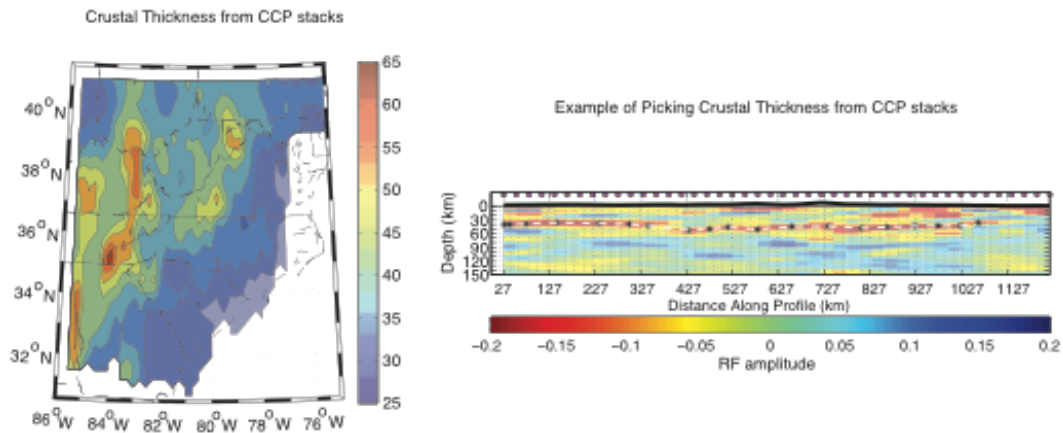
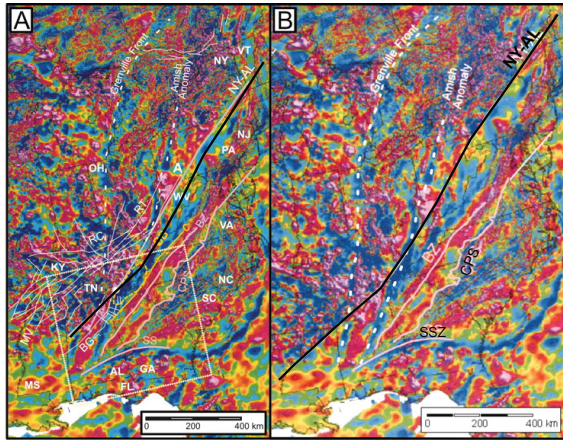


Figure 4.9- Left: Crustal thickness/Moho depth from SR PRF CCP stacks. Contour figure of Moho depths shows a deep (~65km) Moho beneath the Blue Ridge and Appalachian Plateaus (~60 km) that shallows towards the coast (~25km). Right: Moho depth from CCP stacks are picked in each horizontal and vertical direction cross section, where Moho depth is interpolated at each CCP stacking point (white dotted line) in-between user picks (black stars). These interpolated values are averaged from both N-S and E-W cross sections to create the crustal thickness map from CCP stacks.

When compared to the aeromagnetic data and gravity anomaly data (**Figure 4.11**), We find that the sharp change in crust thickness between the Piedmont and Blue Ridge seems to agree well with the observed sharp change in gravitational anomaly feature “A” while the two thicker crust in southern Ohio and northeastern Tennessee may agree with gravitational features “B” and “C” in **Figure 4.11B** (*Knucks , 1999; Stein et al., 2014; black line*). When compared to the magnetic data of the region, we find that the NY-AL magnetic lineament (*Steltenpohl et al., 2010 black line— Figure 4.11A*) is mirrors the predicted edge of the Grenville Front (GF) in the northwest portion of our study, although, we do not find evidence of the GF further south along the New York- Alabama (NY-AL) magnetic lineament.

A.



B.

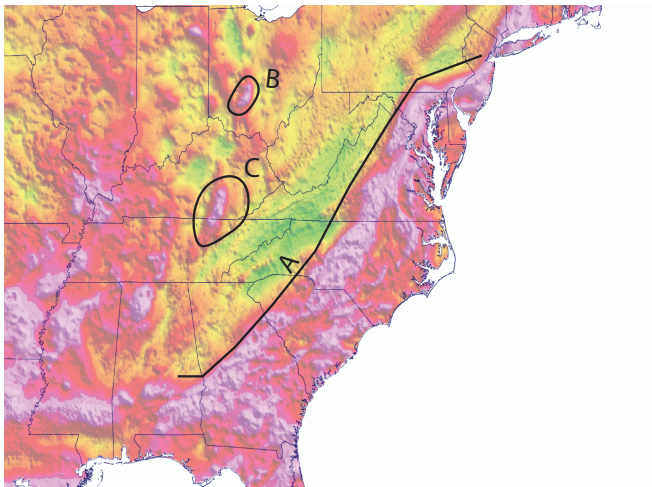


Figure 4.10- **A.** Aeromagnetic maps, where reds are aeromagnetic highs and blues are aeromagnetics lows. The black line is the NY-AL lineament which is likely due to a buried strike slip fault (figure modified from *Steltenpohl et al., 2010*) **B.** Bouguer gravitational anomalies in the Southeastern US. Figure created from USGS gravity anomaly map of the conterminous United States (*Knucks, 1999*). Features “A” correspond to a sharp change in crustal thickness, Features “B” and “C” seems to agree with increased crustal thickness measurements from CCP stacks in this study.

We investigate the anomalously thick crust in a W-E cross-section near the maximum crustal thickness estimate (*Figure 4.12*). Beneath the Blue Ridge (BR) and the ETSZ, multiple positive phase arrivals are seen between 40-60 km. Following the dominant positive phase in the east of the stack at about 37 km (beneath the ACP), it appears to begin dipping westward beneath the BR and continues to dip to about 60 km beneath the ETSZ and the Brevard fault zone (BFZ). The crustal thickness of ~60 km agrees well with the positive phase in the SRF CCP stacks, providing some confidence that the Moho phase is not a result of constructive interference of uncorrected reverberations in the SR PRF CCP stacks. Similarly, a mid-crustal positive phase at about 20 km (too shallow to be the crust in this region) remains flat beneath the ACP and then appears to dip westward beneath the BR, reaching about 40-45 km – near expected Moho depths in this region. The “double-Moho” structure explains the discrepancy between H-k-V_p stacking and CCP stacking and accounts for the very thick crust observed in this region. Interestingly, a W-E cross section through Maryland (near the northern edge of our CCP stacking volume) shows an intra-crustal layer dipping eastward beneath the Valley and Ridge (V&R) and BR (*Figure 4.13*). This shallow eastward dipping structure is more characteristic of the intra-crustal layering we would expect to arise from inherited structures accreting on top of the Laurentian basement with current subduction directions (*Rivers, 2014*).

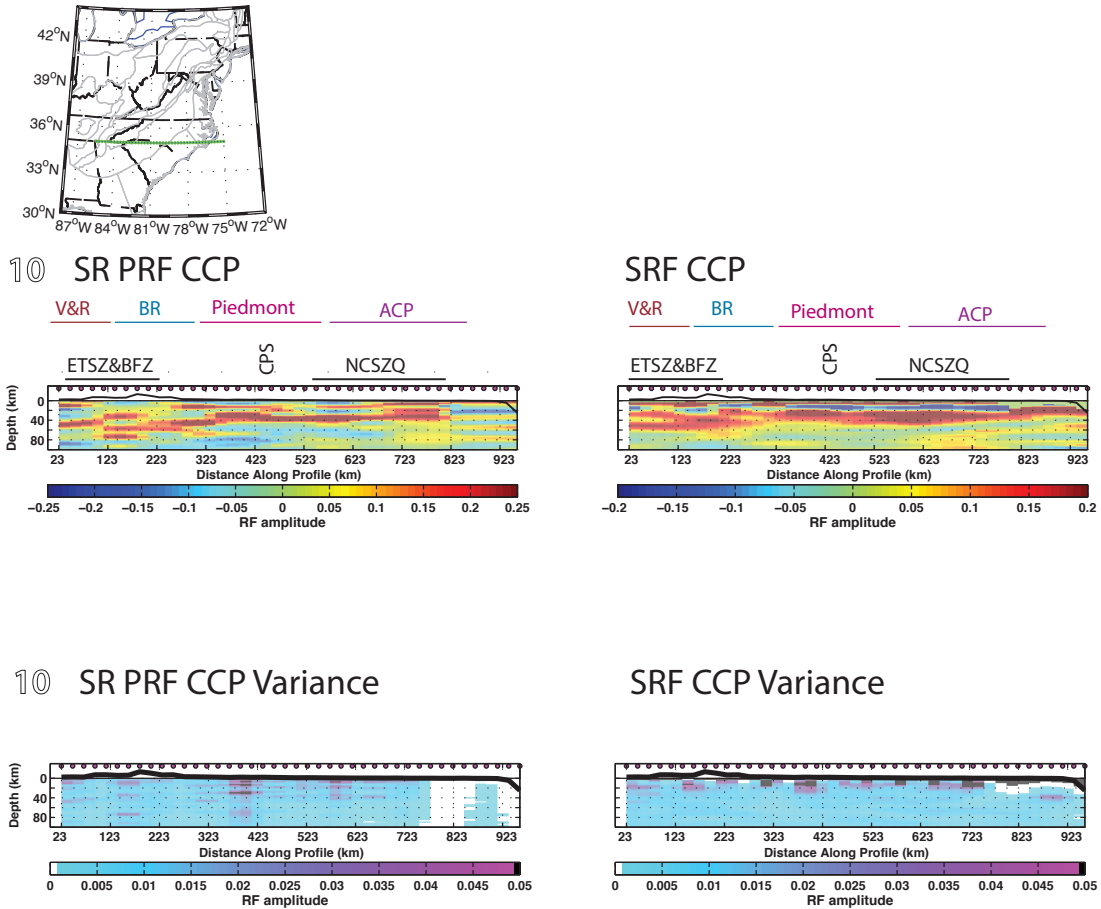


Figure 4.11- W-E Cross-section 10, which passes through the maximum crustal thickness estimate in the Blue Ridge. Evidence of multiple crustal layers dipping sharply westward can be seen beneath the ETSZ and BFZ. The intra-crustal layer is at ~10 km beneath the CPS and deepens to ~40 km beneath the ETSZ, while the Moho phase in the same region begins at ~40km depth beneath the CPS and dips to ~60 km beneath the ETSZ and BFZ. The SRF CCP stacks also show a deep ~60 km Moho beneath the ETSZ and BFZ. A flat intra-crustal layer can also be seen beneath the NCSQ at about 15 km depth. Stacks below show the variance of the RF amplitude at each point in the CCP stack. See caption in Figure 9 for description of labels and abbreviations.

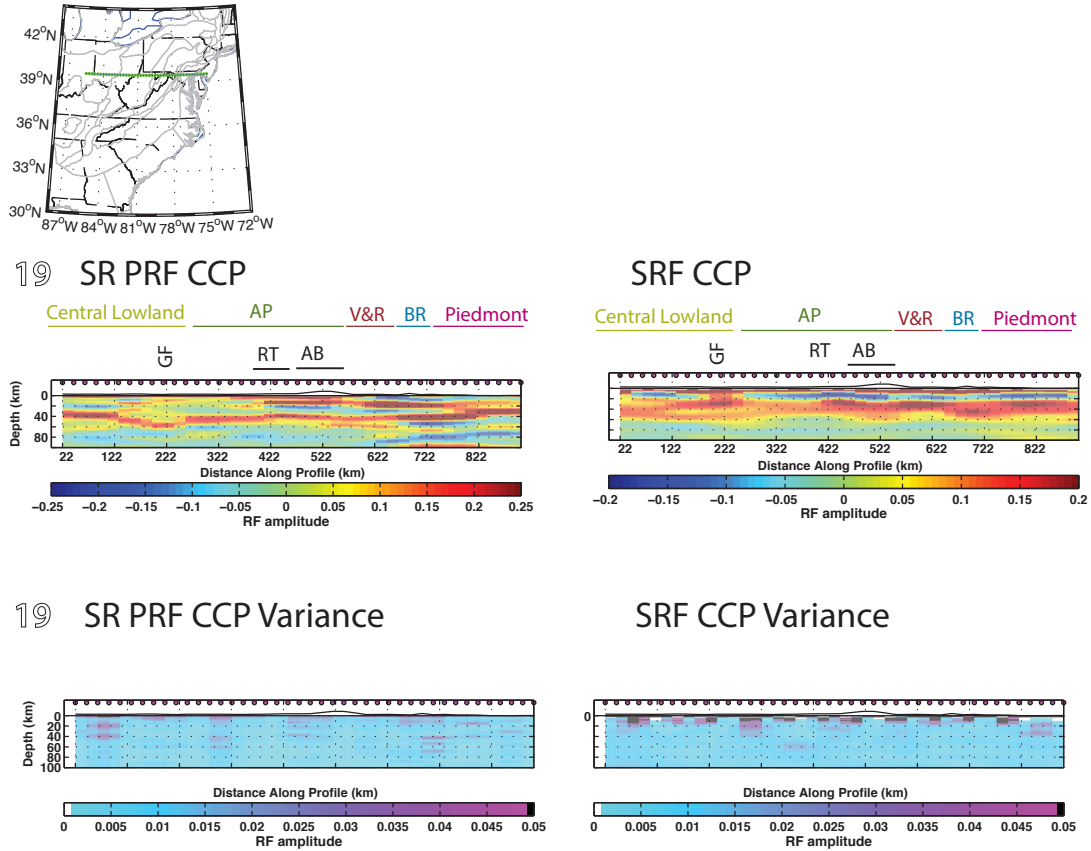


Figure 4.12- W-E Cross section 19 that shows an eastward dipping intra-crustal layer beneath the V&R and BR provinces in the SR PRF CCP stack. This intra-crustal layer appears at ~15 km beneath the Appalachian basin and dips eastward to ~20 km beneath the Piedmont. Stacks below show the variance of the RF amplitude at each point in the CCP stack. See caption in Figure 9 for description of labels and abbreviations.

To better resolve the extent and dip direction of intra-crustal layering, we map all locations where intra-crustal layering appears and note the direction of dip as west, flat, or east (**Figure 4.14**). We find that at the eastern/ northeastern edge of our study region, a shallowly dipping interface across which velocity increases with depth seems to coincide with the location of the Grenville Front (GF) and where crustal thickness sharply increases. In the southern edge of our study region, a flat to

shallowly eastward-dipping intra-crustal layer is present. The current mapped location of the SSZ is just about 50 km south of this region,, and therefore we interpret the intra-crustal layering in this region to be evidence of the location SSZ.

We see one additional east-dipping intra-crustal layer in the northeast portion of our study that is not readily explained. We see two zones of sharp westward dipping intra-crustal layering: In the south, the change from flat to sharp agrees well with the locations of the ETSZ and the Brevard fault zone (BFZ), but in the north, the westward dipping seems to coincide with the central Virginia seismic zone (CVSZ). However, we see no evidence for intra-crustal layering beneath the South Carolina seismic zone (SCSZ).

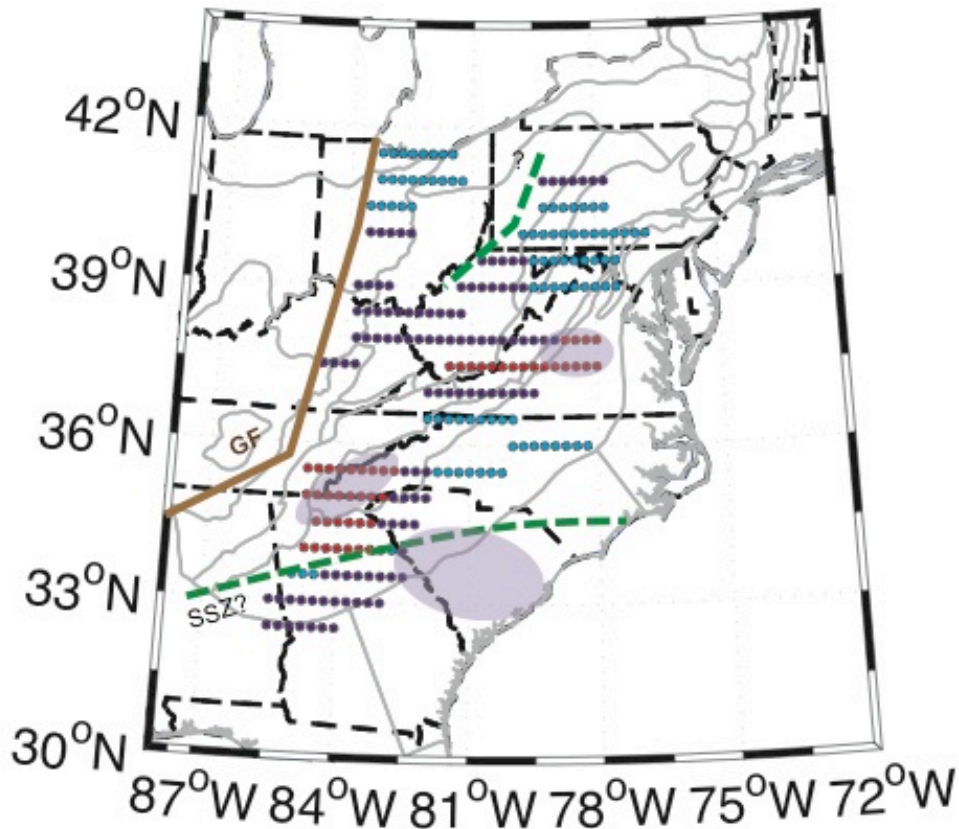


Figure 4.13- Dip direction of intra-crustal layering at each CCP stacking latitude and longitude. Points indicate locations in the CCP stacking grid that show intra-crustal layering. Red points indicate locations where a westward dipping intra-crustal layer is seen, purple points indicate the locations where a flat intra-crustal layer is seen, and light blue indicates the locations where an eastward dipping intra-crustal layer is identified. Lavender shaded regions note the location of seismic zones in the SEUS. The brown line in the western portion of the study notes the predicted location of the Grenville Front (GF), and the green dotted lines indicate possible locations of suture zones based on interpretations of intra-crustal layering (see text). In the south, the green line is interpreted as the Suwannee suture zone (SSZ) where in the north the green dotted line indicates a suture of unknown origin, but may be the suture between the Laurentian and Amazonian crust.

4.5.2 Relationship between Structure and Seismicity

The apparent correlation of westward dipping intra-crustal layering in two of the three seismic zones is surprising. Here we investigate the underlying structure in cross section view in order to shed light on what other crustal and lithospheric processes might explain the location of seismicity in the SEUS.

The N-S trending cross section (D) in **Figure 4.15** crosses through the main portion of the ETSZ. Starting beneath the Central Piedmont Suture (CPS), the Suwannee Suture Zone, and the Piedmont physiographic province, a strong mid-crustal discontinuity can be seen at ~10-20 km depth with an underlying Moho 40 km deeper. The mid-crustal discontinuity dips northward beneath the ETSZ to ~40 km thick while the deeper Moho layer dips northward to ~65 km thick. The Suwannee suture zone (SSZ) is also visible in this cross section. In the SP CCP stack, there is a southward-dipping strong intra-crustal phase. While a similar positive phase is visible the SR PRF CCP stack, it is not resolvable. What is clear is that beneath the SSZ the signal from the Moho changes and becomes weaker in both SR PRF and SP CCP

stacks. We see no coherent negative phase in the lithosphere, implying that there is no MLD and that the LAB signal is weak or deeper than our CCP stacks.

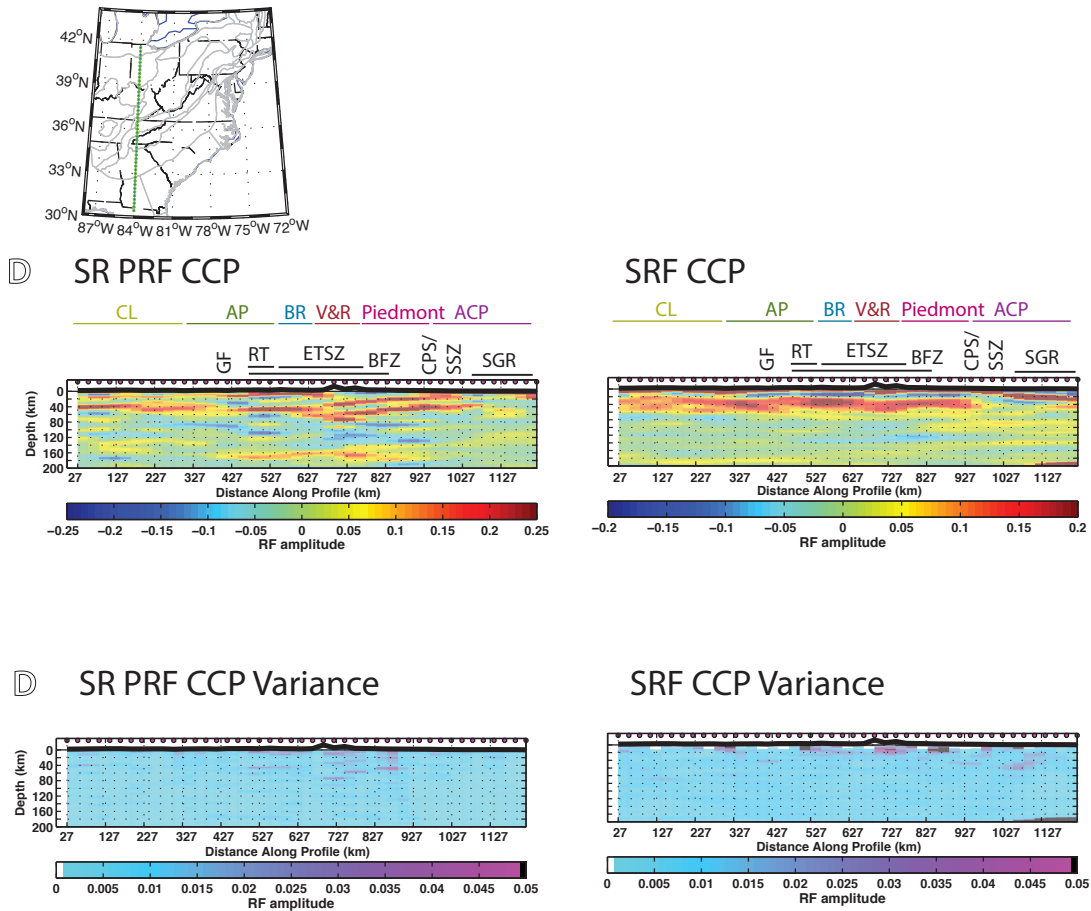


Figure 4.14- N-S cross section D which crosses through the main seismicity in the ETSZ. Here a strong mid-crustal discontinuity is seen dipping northward from ~10 km beneath the CPS/SSZ to ~20 km beneath the ETSZ and BFZ. In the same region, there is a sharp change in the crustal thickness from ~40 km to ~60 km beneath the BFZ/ETSZ. Stacks below show the variance of the RF amplitude at each point in the CCP stack. See caption in Figure 9 for description of labels and abbreviations.

A shallower and weaker westward-dipping intra-crustal layer is also seen beneath the Piedmont and the Central Virginia Seismic Zone (CVSZ-*Figure 15*). Here the W-E cross section (16) shows an intra-crustal layer that starts at around 15 km beneath the ACP and only deepens to 22-23 km beneath the BR. The more obvious change beneath the CVSZ is in the Moho depth itself. Beneath the ACP to the east, the Moho depth is not well resolved, but is likely around 25 km; directly below the Piedmont and the CVSZ, the Moho appears to deepen abruptly to around 45 km. The change in crustal thickness happens over a short lateral distance of about 100 km. As in the previous cross-section, there is no obvious evidence of a negative phase indicating the presence of a seismically resolvable MLD or LAB.

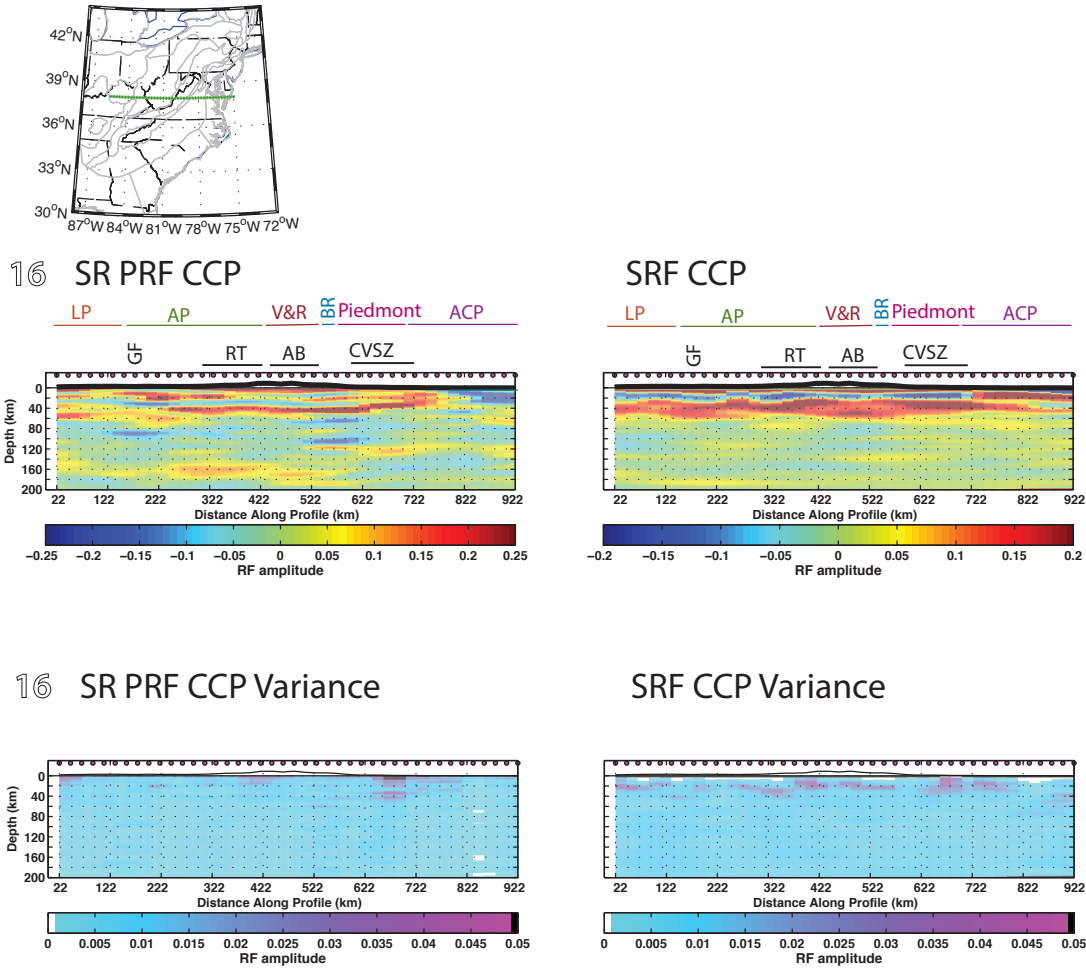


Figure 4.15- W-E cross-section 16 through the CVSZ. Beneath the CVSZ we see an intra-crustal layer dipping slightly westward from around 15 km beneath the ACP and only deepens to 22-23 km beneath the BR. Directly below the CVSZ there is a change in crustal thickness from ~25 km to ~45 km over a later distance of about 100 km. Stacks below show the variance of the RF amplitude at each point in the CCP stack. See caption in Figure 9 for description of labels and abbreviations

Unlike the two other seismogenic zones in the SEUS, There is no westward dipping mid-crustal layer present beneath the South Carolina seismic zone (SCSZ- **Figure 17**). Instead we see a shallow slightly southeastward dipping or flat layer beneath the CPS and which continues beneath the SCSZ (see also **Appendix**: cross-section 6). There is, however, a fairly sharp change in the crustal thickness beneath the SCSZ

seen in the N-S cross section (H) where the Moho shallows from near 40 km to about 25 km directly beneath the SCSZ and over a horizontal distance of approximately 50 km.

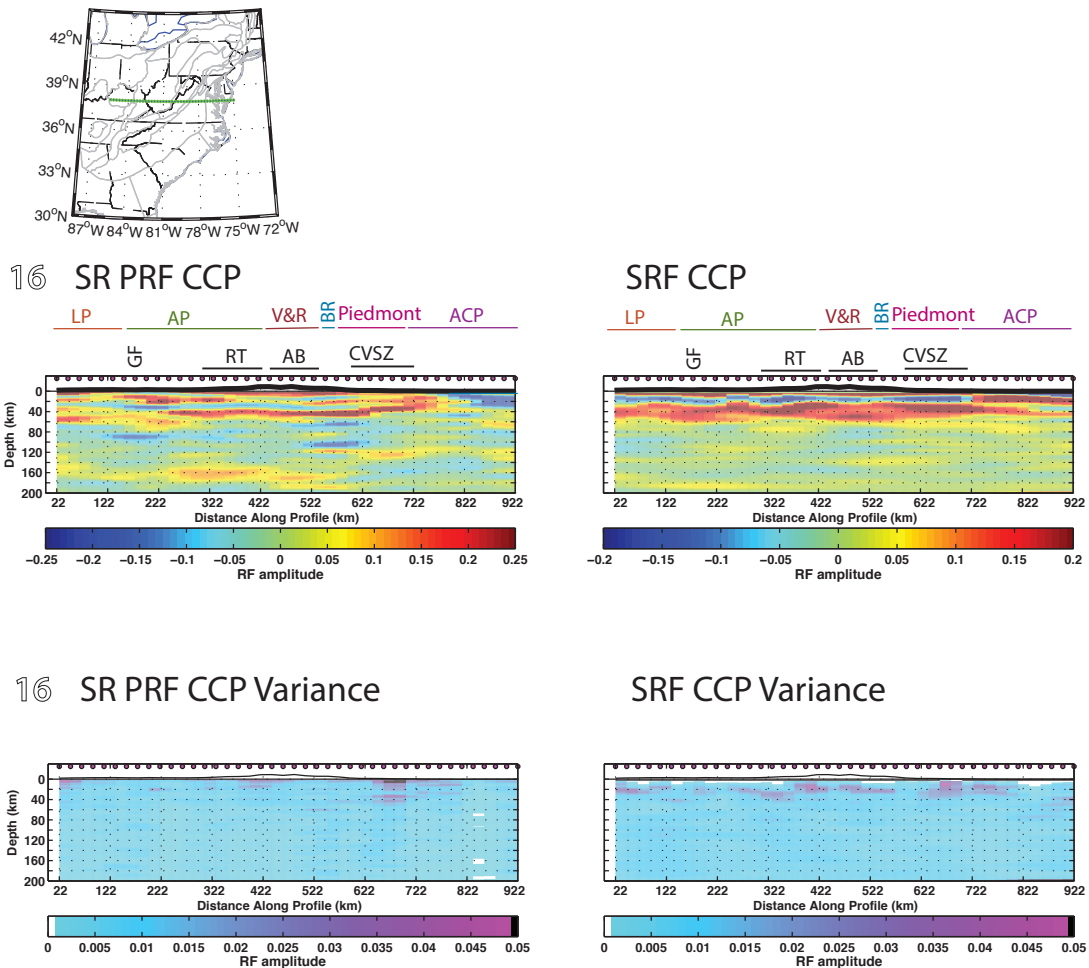


Figure 4.16- N-S cross section H through the SCSZ. In this cross section the Moho appears fairly flat beneath the CL, AB, BR, and V&R. The only large change in the Moho depth occurs almost directly below the SCSZ in the Piedmont. Here the Moho changes from ~42 km to 30 km. Unlike Figures 15 & 16, no westward dipping intra-crustal layering is seen. Stacks below show the variance of the RF amplitude at each point in the CCP stack. See caption in Figure 9 for description of labels and abbreviations

Biryol et al. (2016) describe the region with little seismicity in North Carolina as the North Carolina seismic quiescence (NCSQ – *Figure 18*). The W-E cross-section (10) shows the structure beneath the ETSZ as well as the NCSZ, allowing for direct comparison. Again, at the edge of the W-E cross-section, we see the double Moho feature near the ETSZ with a westward dip. However, beneath the region of NCSQ the Moho remains remarkably flat remaining at a constant depth of 40km from the CPS to the edge of the NCSQ.

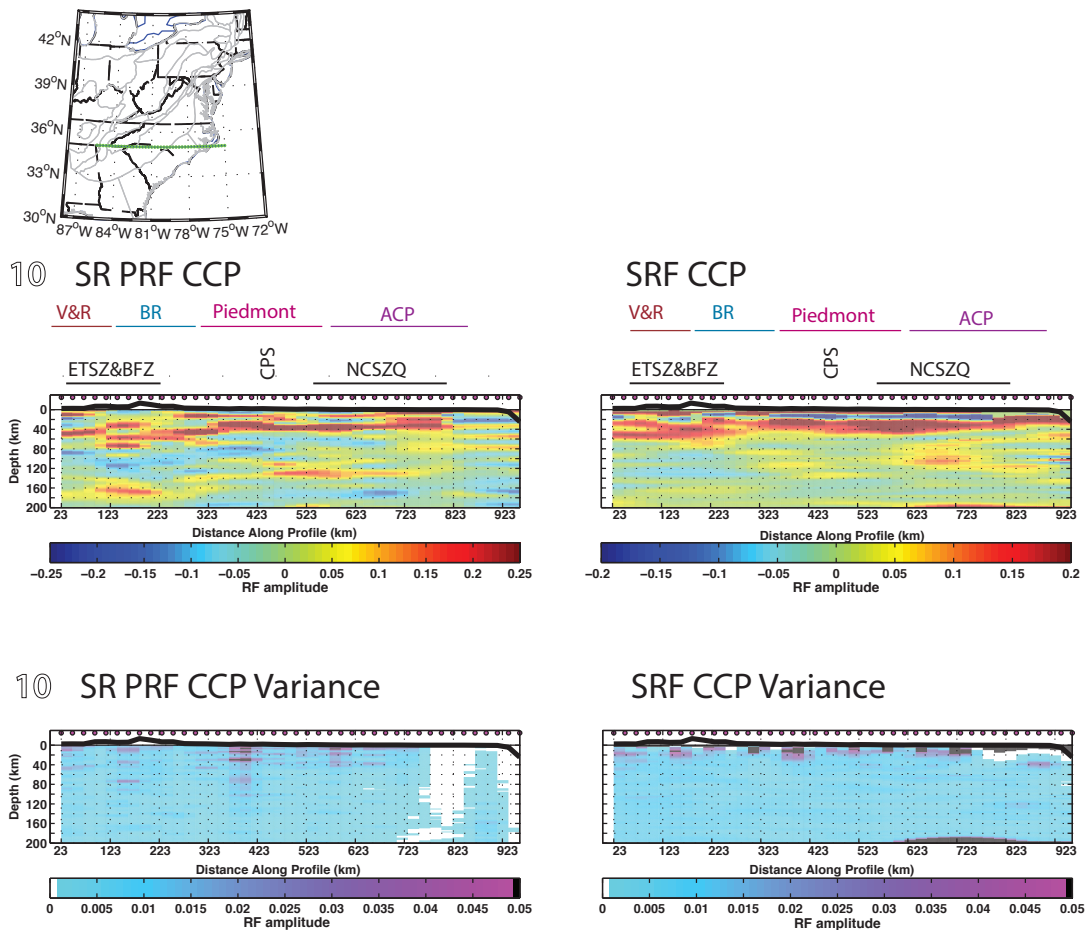


Figure 4.17- W-E Cross-section 10 that passes through the NCSQ. Beneath the NCSQ in the ACP we see both a flat Moho at 40km and no strong evidence for intra-crustal layering. Stacks below show the variance of the RF amplitude

at each point in the CCP stack. See caption in Figure 9 for description of labels and abbreviations

4.6 Discussion

4.6.1 The Extent of the Grenville Front in the SEUS

Recently, it has been debated whether the edge of deformation associated with the Grenville orogeny could be seen in the United States (*Stein et al., 2018*). The deformation edge of the Grenville orogeny, called the Grenville front (GF), marks the extent of continental collision that made up the supercontinent Rodinia. Although the location of the GF has been associated in southern Canada with an eastward-dipping reflector through the GLIMPCE and LITHOPROBE projects (*White et al., 2000*), its location in the United States has remained much more elusive. While some studies suggest that what is interpreted as the GF actually corresponds to the edge of the magnetic anomaly beneath the mid-continent rift through Minnesota and Wisconsin (*Stein et al. 2018*); others associate the boundary to a dipping negative velocity discontinuity consisting of shear zones through the center of Ohio (*Long et al., 2019*).

In this study, we find evidence for low angle eastward mid-crustal layering in Western Ohio and Northern Kentucky that flattens out at ~15 km beneath the Appalachian Plateau. We interpret the western edge of the eastern mid-crustal dipping structure to be evidence of crustal decollements created during the collision of Laurentia to create the supercontinent Rodinia. This north-west edge of the Grenville Front that we constrain agrees with the COCORP project and MAGIC deployment,

which image a 50km dipping zone to 25-30 km depth (*Culotta et al. 1990; Long et al., 2019*). The vergence direction of subduction during the Grenville orogeny is still debated (*Rivers, 1997; Hynes and Rivers, 2010; Boyce et al. 2016*); however, if the subduction is N-NW, then the eastward dipping layering we see near the edge of the predicted GF may be evidence of subsequent crustal shortening during the formation of Pangea instead of crustal emplacement during crustal accretion during the formation of Rodinia.

We do not find evidence of southernmost extent of the GF past Kentucky, which may suggest that our study region does not extend far enough westward to capture the edge of the deformation in the south. Because receiver functions image present-day structure, they cannot constrain the timing of layering; we cannot say for sure that the intra-crustal structure we see is the GF. Indeed, it is possible that the mid-crustal layering is a remnant feature inherited from one or more of the other continental collisions that make up the formation of the SEUS. However, the dipping layer we associate with the GF seems to disappear beneath the Rome Trough. Between 1.3-1 Bya, the Grenville province experienced major granitoid intrusions, which would underlie the RT at the time of its failed rifting between 0.72-0.68 Bya (*Whitmeyer and Karlstrom 2007*) and likely alter the mid-crust, preventing imaging of mid-crustal layering prior to 1.3 Bya. Therefore, we may be able to infer that the western intra-crustal layering must be related to a suture that occurred before 1.3-1 Gya.

We do find another example of eastward dipping intra-crustal structure a few hundred kilometers away to the east, at the eastern edge of the Rome Trough (RT **Appendix**

cross-sections 18-22). While this eastward dipping crustal structure extend to a similar depth and share a eastward dip direction, it appears distinct from the western Ohio GF. The location of the dipping intra-crustal layer observed begins at the eastward extent of the RT and Grenville province and at the edge of the rift boundary that marks the location of the breakup of Rodinia. Therefore, the crustal layering we observe east of the RT is likely evidence of a different suture zone, perhaps between Laurentian and Amazonian crust (*Rivers 2014*), Taconian arcs, or Avalon accreted terranes (*Hatcher, 2010*). The presence of these multiple mid-crustal layers is consistent with the interpretation that the tectonics of crustal emplacement that we observe today in other locations around the world, were operating in the SEUS in the past. (*Long et al., 2019; Hopper et al., 2017*)

4.6.2 Evidence of the Suwanee Suture

In addition to the GF, we also image crustal layering in the SEUS similar to that found by Hopper et al. (2017). Hopper et al. (2017) discuss the likelihood of shallowly-eastward-dipping layer as being the Suwanee Suture Zone. The Suwanee Suture zone marks the boundary between Laurentian and Gondwanan rocks during the formation of the supercontinent Pangea. Here, we map the extent of the southeastward dipping feature from our CCP stacks (**Figure 14**), and find that it agrees well with predicted locations of the suture within ~50km. In the SRFs, the dipping structure associated with the Suwanee Suture Zone continues into the South Georgia Rift, but this feature is not seen on the SR PRF CCP stacks. One possible explanation for this is that the PRFs might not be able to capture the impedance

contrast if it occurs gradually over tens of kilometers, while the lower frequency SRFs can see it clearly.

4.6.3 Westward dipping “double Moho”

Beneath the Blue Ridge and Piedmont in southeastern Tennessee and northern Georgia, we find evidence for a westward dipping intra-crustal layer that produces strong signatures in the SR PRF CCP stacks. This intra-crustal layer starts at ~10 km beneath the Piedmont near the CPS and dips down to ~45 km beneath the eastern Tennessee seismic zone 400 km to the west. The underlying Moho starts between 43-40 km and dips downward to nearly 65 km in the same region. The COCORP line imaged a west-dipping layer in northernmost Alabama where the expectation was to image the edge of the southeastward-dipping Grenville Front (*Culotta et al., 1990*). If we assume that the subduction direction during the Grenville Orogeny is S-SE, the explanation for the westward dipping intra-crustal proposed in the CORCORP study is that the subduction polarity switched beneath this area with the accretion of a colliding arc terrane. Arc passive margin collision events can account for crustal growth and a subduction polarity reversal (*Clift et al., 2003*). However, this active source study did not image a deeper crustal boundary below.

Wagner et al. (2012) identified an intra-crustal layer and deeper Moho with the same characteristics we observe at the border of South Carolina, North Carolina, and Tennessee, where they interpret this feature to be a “double-Moho”. A “double-Moho” could be caused by lithospheric downwelling (*Zandt et al., 2004*), partial

eclogitization of the lower crust (*Schulte-Pelkum et al. 2005*), and/or wedge tectonics (*Hansen and Dueker, 2009*). It has been suggested that the only reliable seismic observable criterion for lower crustal eclogites is a double Moho observed near a Moho uplift that would be unrealistic if the Moho is interpreted as the base of a crust (*Mjelde et al., 2013*). While we observe the shallow layer extending up, too shallow to be interpreted as the Moho, the fact that it extends to ~10 km depth means that this cannot be explained by a boundary between a partially eclogitized lower crust alone. Wagner et al. (2012) interpret that an indenter (either the Carolina terrane or from crustal shortening) is thrust into the Laurentian crust, pushing some of it down where it could become partially eclogized, which is consistent with the isostasy in the region. However, in that study, they observe a Moho-hole, a region where only the deeper Moho exists, which is not what we observe in the CCP stacks.

A deep >60 km Moho is observed beneath the Himalaya, overlain by a shallow interface that has been interpreted as a double-Moho (*Schulte-Peklum et al. 2005*). In the modern Himalayan continent-continent collision, the interpretation of Schulte-Peklum et al. (2005) of the double Moho is that the shallow feature at ~15-20 km is occurring due to a strongly anisotropic layer at the decollement between the Indian and the Himalaya plates. At depths of 45-55 km, the shallower feature is interpreted as the boundary of partial eclogitization of the lower crust. If this interpretation were relevant to the SUES, it too, like the COCORP interpretation, would require a subduction polarity change.

A subduction polarity change can occur with the accretion of an island arc, such as a

central gneiss island arc accretion during the Precambrian, as proposed in Culotta et al. (1990). The double Moho we observe is consistent with a shear zone near the surface and partial eclogization of the lower crust observed in modern continental collisions. Given the extent of the sharply westward dipping feature we observe in the southern portion of **Figure 14, Appendix C**, we interpret that at shallow depths, the shallow intra-crustal layer is likely a remnant top of the shear zone created during subduction of an accreted island arc, while at deeper depths, it represents partial eclogization of the lower crust. Further study could provide insight into the anisotropic characteristics of the top layer, and determine whether it is likely to be related to shear at shallow depths.

4.6.4 Correlation of Structure to SEUS Seismicity

While two of the three seismic zones show correlations to westward-dipping intra-crustal layers, we find all three show a relationship between sharp changes in crustal thickness and seismicity in contrast to the flat crust beneath the region of NCSQ. This observation agrees with that of Soto-Cordero et al. (2017), who argue that sharp crustal thickness changes can focus strain and control the location of seismicity in the Mid-Atlantic.

This does not mean that changes in the underlying lithospheric structure beneath regions of seismicity does not also play a role in controlling the location of seismicity or that the model proposed by Biryol et al (2016) is incorrect. With CCP stacking, we only image the upper 200 km of the lithosphere. The lithospheric drip observed in the

Biryol et al. (2016) study between 200-400 km. Unlike lithospheric drip, if MLDs were related to seismicity in the SEUS, we would expect to find evidence supporting their existence, at least in the SRF CCP stacks. The lack of evidence supporting the relationship between mid-lithospheric discontinuities and seismicity on the east coast is telling in-and-of itself. We should be able to see MLDs if they exist, at least on the SP CCP stacks. The fact that we see no relationship between MLDs and seismicity (and no evidence of pervasive MLDs in general), leads us to conclude that MLDs are not related to intraplate seismicity on the east coast.

4.6.5 On the lack of a lithosphere asthenosphere boundary or intra-lithospheric layering

The boundary between the lithosphere and asthenosphere should be associated with a negative phase that would imply a velocity decrease with depth. Unlike the strong positive Moho phase, no strong and coherent negative phase is visible in our CCP stacks. The lack of visible LAB beneath the SEUS using SR PRF and SRF CCP stacks implies that either the LAB across the SEUS occurs at depths greater than 200 km, in agreement with magnetotelluric studies, or that the velocity decrease at the base of the lithosphere occurs over 40 km in depth, and therefore is too gradual to be imaged even by low frequency SRFs (Ford et al., 2010). Both a deep LAB and a diffuse LAB boundary would be consistent with old continental lithosphere and shear wave observations beneath the SEUS (Wagner et al. 2018). Therefore, this is our preferred interpretation of lack of clear LAB-related signatures in our CCP stacks.

4.7 Conclusions

Using sediment removed PRFs and SRFs, we constrain complex features in the lithosphere and attempt to place them in the context of the tectonic evolution of the SEUS. We find that the crustal thickness in the SEUS ranges from 25 km near the Atlantic coast to about 65 km beneath the Blue Ridge. The 65 km crust we interpret is surprisingly deep, but reflects the more complex structure we see in intra-crustal layering.

We find evidence for both eastward and westward dipping intra crustal layering through the SEUS. We interpret the eastward dipping intra crustal layers as evidence of crustal emplacement marking the suture zone of past accretionary events. In the south, we map the Suwannee suture zone, where the Gondwanan crust is emplaced on Laurentian basement. In the northwest, we interpret the dipping intra-crustal layer to mark the Grenville Front, and in the northeast, that it marks a separate suture zone along the rift of Rodinia of unknown origin.

We interpret the westward dipping intra-crustal layering beneath the ETSZ and BFZ in Tennessee to reflect a suture of arc accretion that changes the polarity of subduction to a westward dipping regime. The “double Moho” feature likely reflects similar processes observed in the Himalaya today, where the top boundary represents a shear zone at the detachment boundary which transitions to a partially ecologic lower crust at depth.

We find a correlation between sharp changes in crustal structure and seismogenic zones in the SEUS and no correlation between seismogenic zones and lithospheric structure. This finding is in agreement with Soto-Cordero et al. (2018), which suggests that crustal structure and topography play a large role in dictating the locations of intraplate earthquakes.

Finally, we find no evidence of a sharp lithosphere-asthenosphere boundary or evidence for mid-lithospheric discontinuities beneath the SEUS, which we interpret to suggest that the lithosphere-asthenosphere transition beneath the SEUS is diffuse, occurring over at least 40 km in depth.

Currently, this study relies only on the USArray TA deployment; however, there are smaller-scale dense deployments in the SEUS that may help add higher resolution to some interesting areas. In addition, developments in receiver function migration techniques beyond the relatively simple CCP stacking used in this study should allow for better imaging of sharp lateral discontinuities. Constraining sharp lateral discontinuities of the Moho beneath seismic zones may further illuminate what crustal conditions control the locations of intraplate seismicity.

Summary

The goal of this project was to understand underlying structure of the Southeastern United States and its relationship to seismic hazards posed by ongoing intra-plate seismicity. Since the recent damaging 2011 Mw = 5.5 Mineral, VA earthquake, many studies have sought to understand the relationship between passive margin earthquakes and the underlying mechanisms that control them. Thanks to the large-scale deployment of the EarthScope USArray Transportable Array and focused MAGIC and SESAME seismic deployments, seismologists have been able to image the subsurface of this region with significantly higher resolution than ever before.

Despite the numerous recent studies of the SEUS, constraining the basic structure of the lithosphere has proven difficult. Receiver functions are perhaps the most useful seismic tool to image discontinuities beneath a seismic station such as the depth to basement, Moho, lithosphere-asthenosphere boundary, and any intra-lithospheric layering. However, while SRFs can yield interpretable images of these structures, their low frequency content results in relatively low resolution. On the other hand, interpreting deeper structure with high-frequency PRFs is challenging as signal from deeper structures can become overprinted by multiples and reverberations from the sedimentary basins. This problem is significant as over 50% of this region is overlain by sediment including the Appalachian basin, Mississippi embayment, and Atlantic coastal plain.

To tackle this challenge and enable high-resolution PRF imaging of lithospheric structure across the SEUS, we develop a method to suppress sediment reverberations

in PRFs using a resonance removal filter. We also leverage complimentary SRFs and SsPmp RFs that are not so affected by sedimentary reverberations, and use them to construct H-k-VP triple stacks. This method enables use to constrain the crustal thickness, V_p/V_s ratio, and average crustal P-wave velocity in regions where sediment reverberations can lead to incorrect interpretations of the crustal properties (**Chapter 2**).

We find that the parameters used to remove sediment reverberations are also useful to constrain important parameters of ground motion during an earthquake for seismic hazard analysis. Because earthquakes on the East Coast are generally smaller in magnitude and occur more infrequently, fewer studies have been done that constrain the basin structure. By using measurements of basin phase arrivals on high frequency PRFs, we are able to constrain both the site fundamental frequency and average velocity profiles of the SEUS. The fundamental frequency is important for understanding how large building and structures will be affected by ground shaking as matching resonant frequencies between structures and basin can be particularly damaging. We validate our method by comparing against more traditional methods of estimating basin fundamental frequency. In addition we provide equations of V_p and V_s profiles to 2.5 km depth for the Atlantic Coastal Plain (**Chapter 3**).

Finally, we apply the methodology developed in Chapter 2 to the SEUS to better understand its history of inherited structures and relationship to intraplate seismicity. By constructing common conversion point stacks of both RR PRFs and SRFs, we map the lithospheric structure across the SEUS. We find no evidence of a strong LAB

or intra-lithospheric layering to 200 km. We do find evidence for multiple intra-crustal layers that are likely related to inherited structures from past continental collision events, but that have no correlation with regions of seismicity. We do, however, note that directly beneath the eastern Tennessee seismic zone, central Virginia seismic zone, and South Carolina seismic zone a sharp change in Moho depth occurs. In contrast, beneath the region of North Carolina seismic quiescence the Moho depth remains remarkably flat and consistent (**Chapter 4**).

The obvious avenues of future work for this research would be to apply the new methods of RR H-k- V_p stacking and fundamental frequency from high frequency PRFs methods to other regions where sediment reverberations limit study of lithospheric structure. Specific regions of interest could include other areas with intraplate seismicity, such as the New Madrid seismic zone in southern Illinois and Missouri to investigate if a sharp crustal thickness exists beneath.

Below the crust in the CCP stacks calculated for the SEUS, we see evidence of Moho multiples coincident with expect MLD/LAB arrivals. Using the timing of these reverberations can help improve constraints on crustal structure in CCP stacks, since the arrival depths (and times) of Moho multiples in the CCP stacks depend on crustal thickness and also crustal V_p and V_s , ray parameter and back azimuth (*e.g. Jenkins et al. 2018*).

Calculating P-to-s receiver functions from Ocean Bottom Seismometers (OBS) has proven to be even more challenging as water-wave reverberations overprint P-to-s

arrivals and noise on the horizontal components can introduce artifacts into the receiver functions (*Bostock and Trehu 2012, Janiszewski and Abers 2015*). New techniques for removing OBS noise can reduce these undesirable effects, though typically only at long periods (*Ruan et al 2014, Bell et al 2015*). Additionally, ocean margin settings contain thick low velocity sedimentary layers along the Cascadia subduction zone (1-2 km) and on the offshore Eastern North American Margin (ENAM 5-10 km). This low velocity sediment may be responsible for significant reverberations that obscure interpretations made from P-to-s receiver functions and overprint crustal and lithospheric arrivals. Extending methodologies developed above, one could develop a systematic method of calculating sediment-removed P-to-s receiver functions for otherwise challenging OBS stations to answer outstanding questions about the sediment and lithospheric structure on both the Cascadia subduction zone and ENAM.

In addition, this research motivates future investigations using high frequency receiver functions to understand the very near surface. Previously, it has been suggested that constraining the S-wave velocity structure in the sediment could be done using body wave polarization analysis and the frequency-dependence of apparent incidence angle of teleseismic P waves. However, when sediment reverberations contaminate the high frequency RF signal, the apparent incidence angle method fails to provide useful constraints on the sediment structure, instead producing velocities that consistently over and underestimate the actual velocity structure. If the SR removal filter successfully removes the reverberations whilst

preserving the direct sediment conversions, then it is possible the apparent incidence method would be useful. Producing a site-specific velocity structure using SR and the apparent incidence angle method would provide a more detailed model of the sediment velocity structure for hazard analysis.

Appendices

Appendix A: Table A.1

All station measurements of stations used in **Chapter 3** that have been determined to lie on the ACP (according to Fenneman physiographic provinces of the US, 1947) including: Depth to basement, two-way S-wave travel time in the basement T_{SS} , and amplitude r_0 , travel time of the PP_{bs} phase T_{PPbs} , and amplitude (PP_{bs}), and the basin fundamental frequency F_0 at each station.

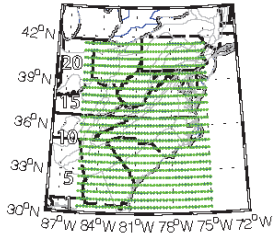
Station name	Depth to basement (km)	T_{SS} (s)	r_0	T_{PPbs} (s)	PP_{bs}	F_0
153A	0	0.47	0.58	0.2	0.93	1.06
154A	0.157	1.28	0.39	0.55	1.17	0.39
155A	0.278	1.3	0.5	0.6	1.13	0.38
156A	0.395	1.69	0.37	0.75	0.64	0.3
157A	0.464	1.62	0.48	0.9	0.56	0.31
158A	0.701	1.79	0.53	0.96	0.58	0.28
251A	0.061	1.32	0.41	0.66	1.51	0.38
252A	0.233	1.65	0.51	0.75	0.99	0.3
253A	0.279	1.62	0.52	0.85	0.65	0.31
254A	0.766	2.36	0.45	1.05	0.58	0.21
255A	0.796	1.95	0.51	0.85	0.52	0.26
256A	0.758	2.15	0.52	0.97	0.29	0.23
257A	0.877	1.9	0.41	0.8	0.75	0.26
351A	1.667	2.48	0.34	1.2	0.31	0.2
352A	1.275	2.27	0.36	1.15	0.82	0.22
353A	1.606	2.5	0.4	1.36	0.43	0.2
355A	1.358	1.88	0.3	0.85	0.65	0.27
356A	1.172	2.09	0.38	1.09	0.38	0.24
357A	1.168	2.09	0.48	0.9	0.3	0.24
452A	2.19	2.82	0.32	1.35	0.39	0.18
453A	2.112	3.1	0.14	0.9	0.18	0.16
454A	2.484	1.35	0.39	0.75	0.17	0.37
455A	2.27	2.38	0.12	0.65	0.16	0.21
456A	1.519	1.37	0.17	0.9	0.26	0.36
457A	1.592	2.06	0.26	0.34	0.07	0.24
553A	3.237	1.65	0.36	0.8	0.18	0.3
554A	4.378	1.32	0.41	0.65	0.16	0.38

555A	3.958	1.09	0.41	0.5	0.15	0.46
CBN	0.334	0.63	0.69	0.15	1.52	0.79
CNNC	0.059	0.52	0.68	0.1	1.31	0.96
GWDE	1.521	1.92	0.37	0.91	0.6	0.26
N62A	0.257	0.5	0.63	0.1	1.08	1.01
NHSC	0.451	1.42	0.5	0.7	0.8	0.35
O61A	0.567	0.77	0.66	0.25	1.27	0.65
P61A	1.309	1.88	0.54	0.69	0.41	0.27
Q59A	0.524	1.23	0.51	0.55	0.82	0.41
Q60A	1.07	1.88	0.55	0.8	0.64	0.27
Q61A	1.875	2.11	0.48	1.05	0.45	0.24
R59A	0.461	1.12	0.41	0.5	0.83	0.45
R60A	0.718	2.11	0.47	0.85	0.56	0.24
R61A	2.134	2.68	0.2	0.91	0.11	0.19
S59A	0.371	0.52	0.67	0.2	1.06	0.96
S60A	0.595	1.53	0.52	0.65	1.05	0.33
S61A	1.795	2.59	0.34	0.8	0.19	0.19
T60A	0.494	1.19	0.56	0.55	0.8	0.42
TIGA	1.427	2.36	0.37	1.2	0.37	0.21
U60A	0.137	0.7	0.72	0.2	1.29	0.71
U61A	0.751	2.41	0.49	0.85	0.59	0.21
V60A	0.174	0.84	0.73	0.25	1.01	0.59
V61A	0.657	2.18	0.51	0.75	0.46	0.23
V62A	1.496	2.59	0.45	0.61	0.36	0.19
W60A	0.13	0.79	0.73	0.3	0.94	0.63
W61A	0.471	1.6	0.38	0.5	0.87	0.31
X59A	0.082	0.68	0.78	0.1	1.23	0.74
X60A	0.151	0.82	0.62	0.35	1.08	0.61
Y57A	0.007	0.5	0.71	0.1	0.68	1.01
Y58A	0.151	0.98	0.64	0.45	0.88	0.51
Y59A	0.213	1.03	0.53	0.4	1.02	0.49
Y60A	0.288	1.03	0.55	0.45	0.88	0.49
Z55A	0	0.66	0.64	0.15	1.46	0.76
Z56A	0.081	0.86	0.69	0.35	1.15	0.58
Z57A	0.226	1.23	0.48	0.5	0.89	0.41
Z58A	0.412	1.35	0.54	0.65	0.62	0.37
Z59A	0.522	1.3	0.52	0.55	1.04	0.38

Appendix B: CCP Figures for Chapter 4

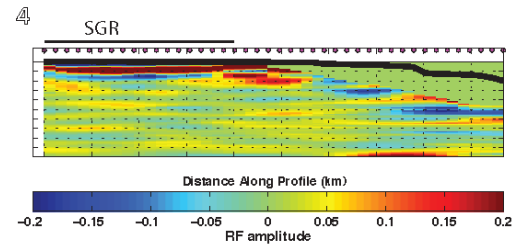
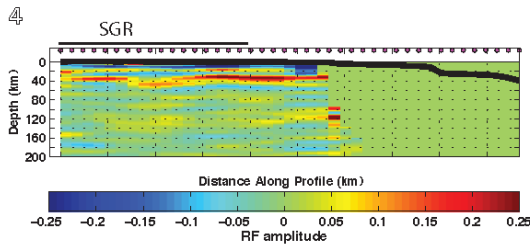
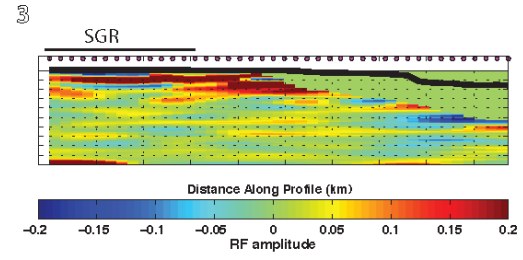
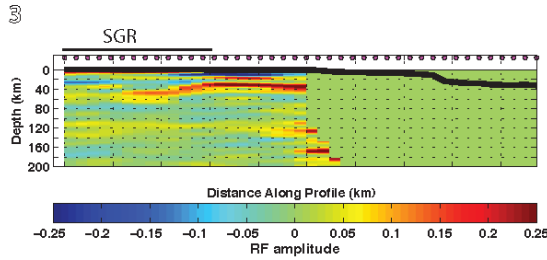
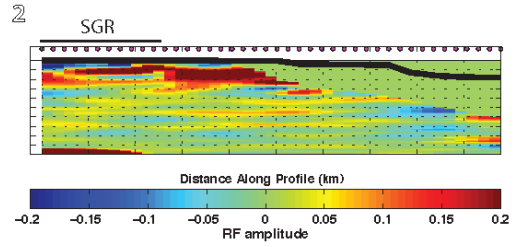
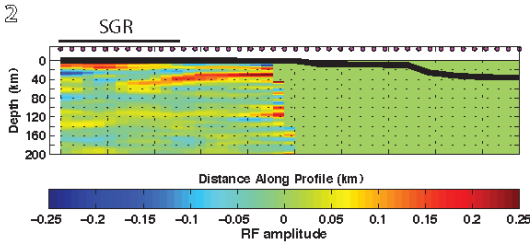
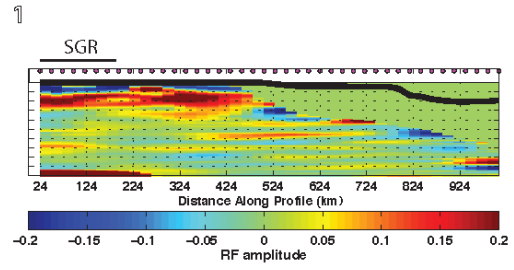
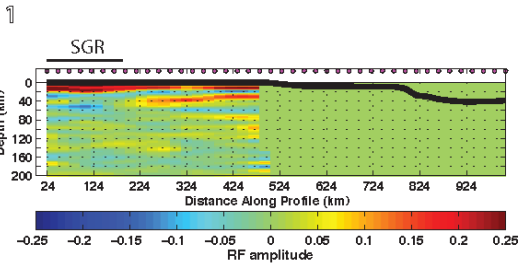
Appendix B contains all additional SR PRF and SPRF CCP stacking cross-sections for Chapter 4. Cross Sections are either W-E trending and are given numbers that correspond to their S-N location or are N-S trending and are given letters that correspond to their W-E location. Each set of 4 cross sections contains a map (top left corner) with cross section locations and directions for reference.

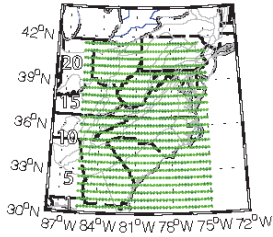
Key for figures: labels in black are features which the cross sections pass through, and locations can be found in Figure 4.1 in Chapter 4. Lines below labels indicate the distance on the cross section that each cross-section passes through. RT= Rome trough, GF= Grenville front, SGR = South Georgia rift, ETSZ = Eastern Tennessee seismic zone, BFZ = Brevard fault zone, CPS= central Piedmont suture, NCSQ = North Carolina seismic quiescence, AB = Appalachian basin, SCSZ = South Carolina seismic zone, SSZ = Suwanee suture zone, CVSZ = central Virginia seismic zone



SR PRF CCP

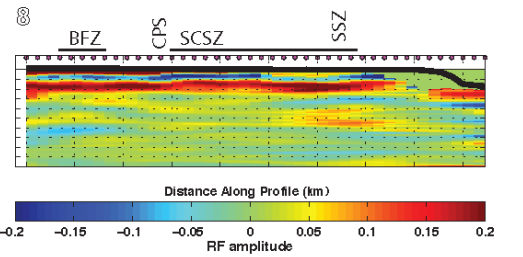
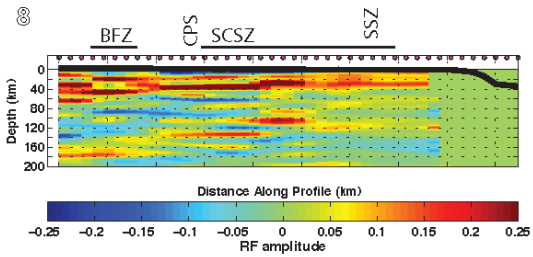
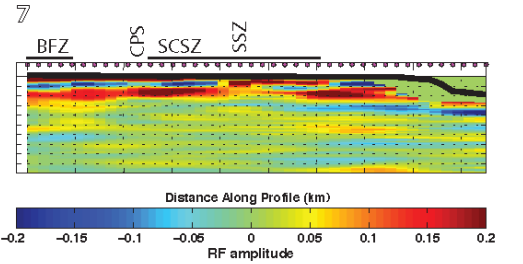
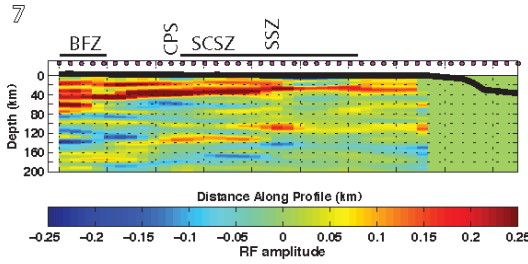
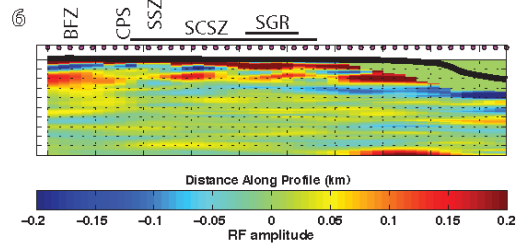
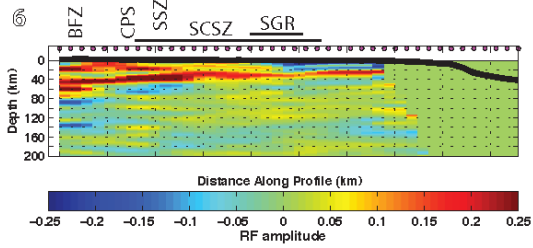
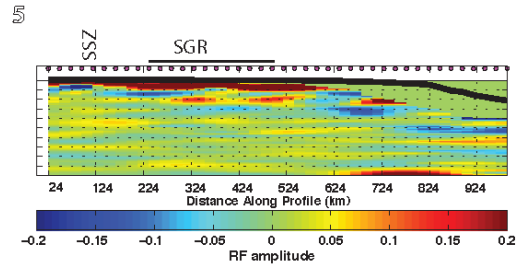
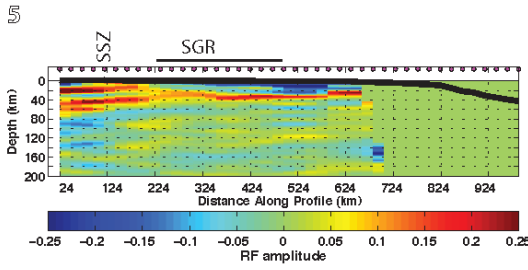
SRF CCP

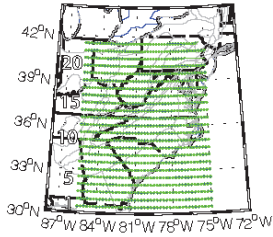




SR PRF CCP

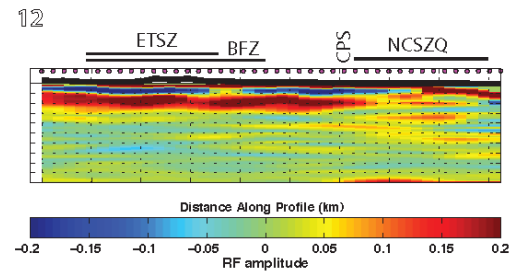
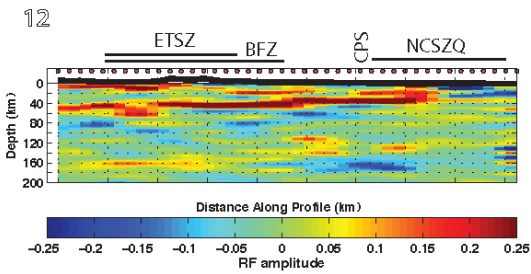
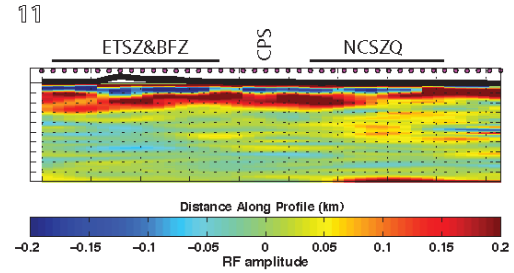
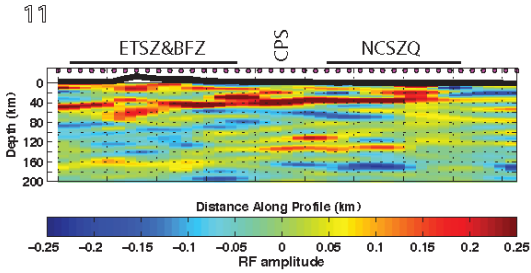
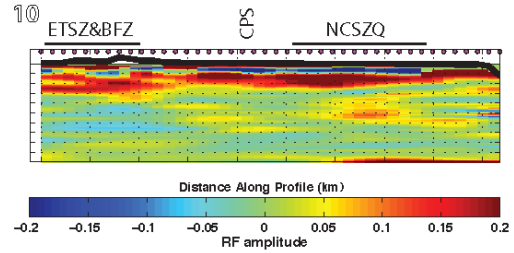
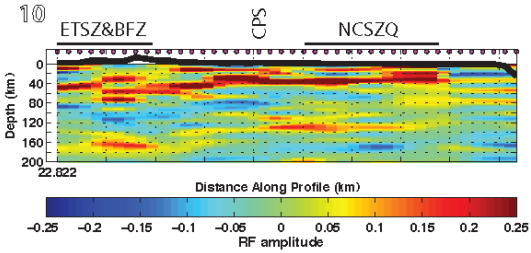
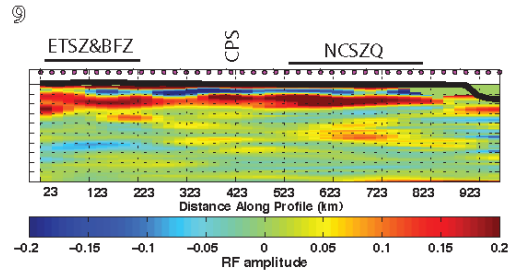
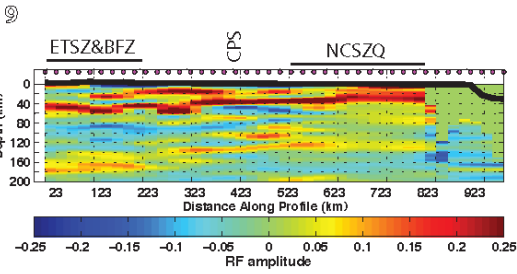
SRF CCP

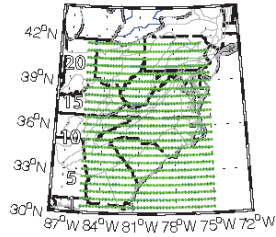




SR PRF CCP

SRF CCP



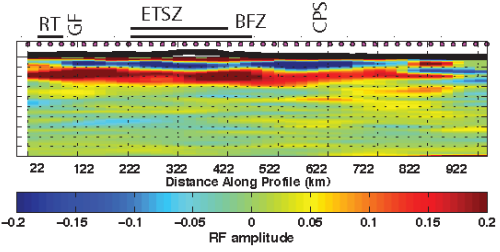
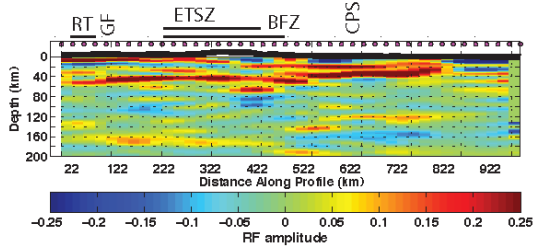


SR PRF CCP

SRF CCP

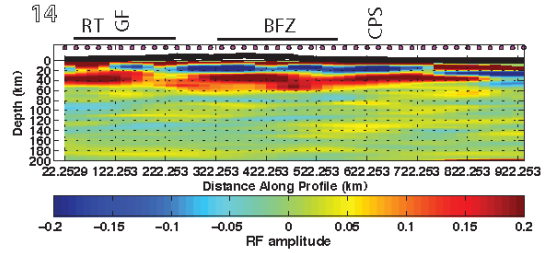
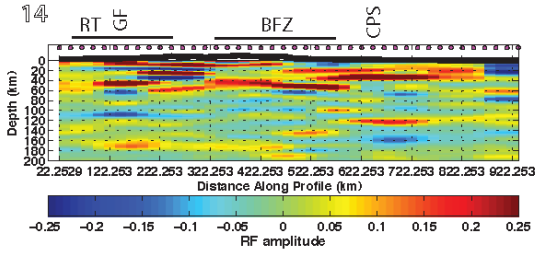
13

13



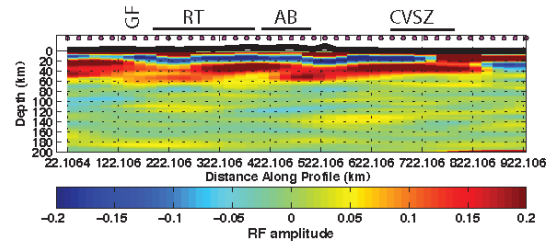
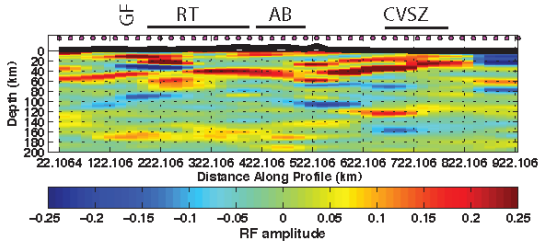
14

14



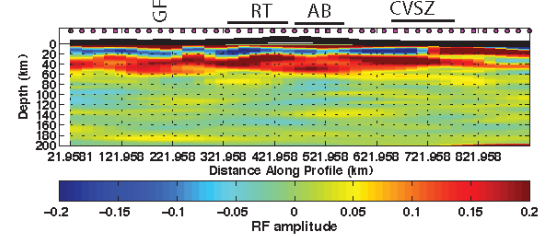
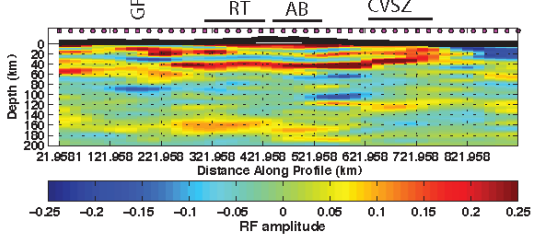
15

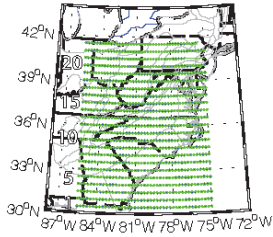
15



16

16



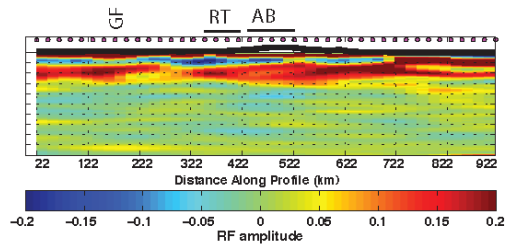
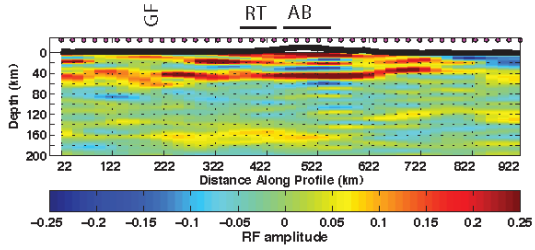


SR PRF CCP

SRF CCP

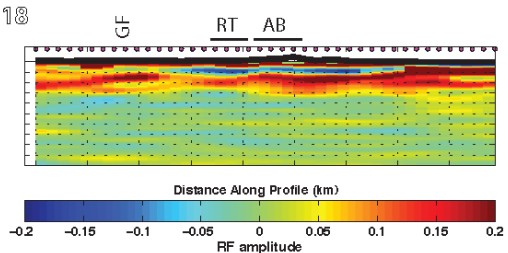
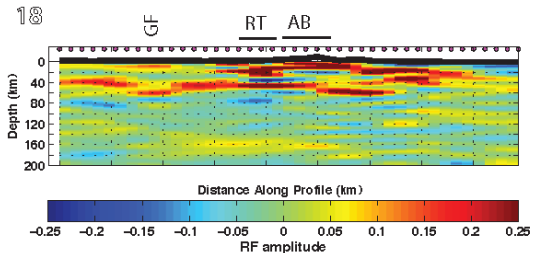
17

17



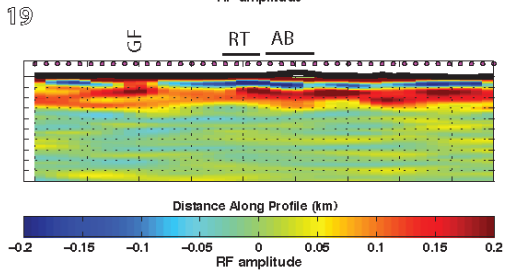
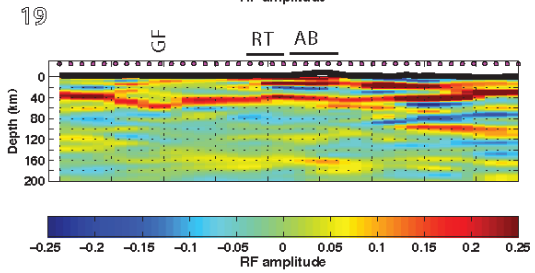
18

18



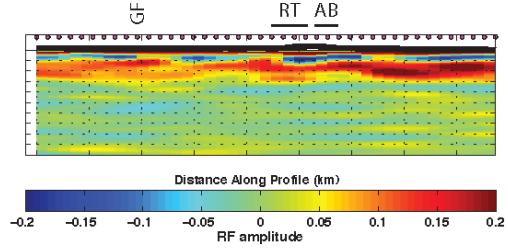
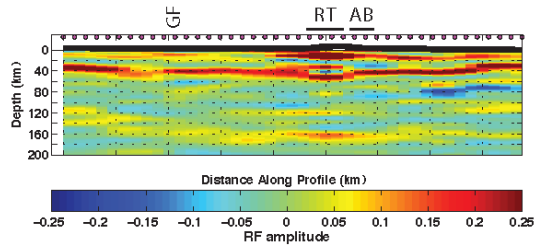
19

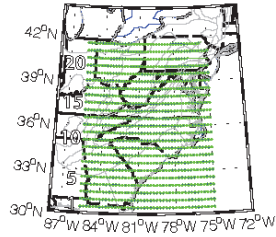
19



20

20



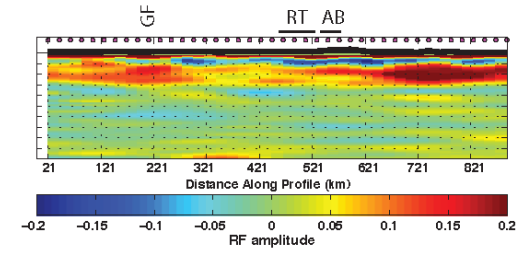
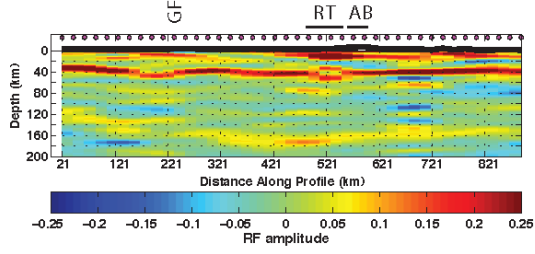


SR PRF CCP

SRF CCP

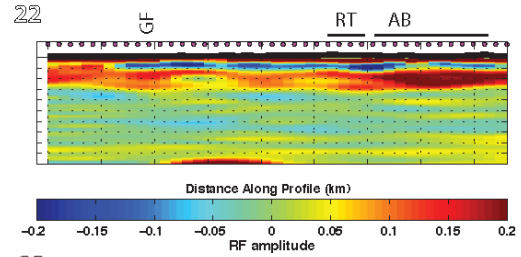
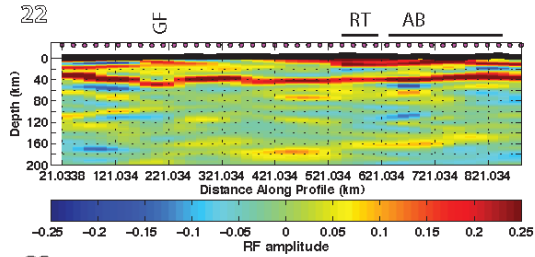
21

21



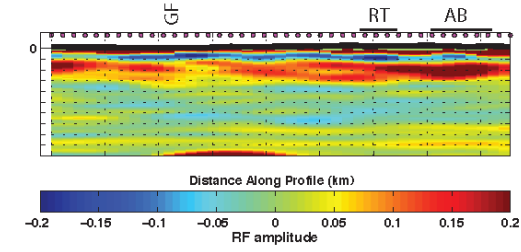
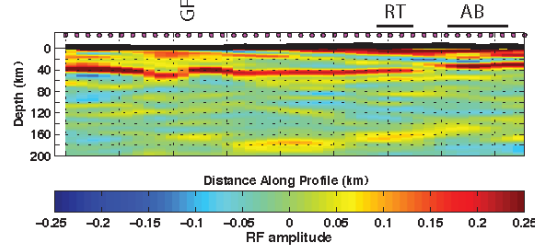
22

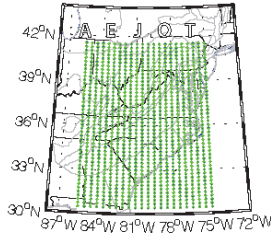
22



23

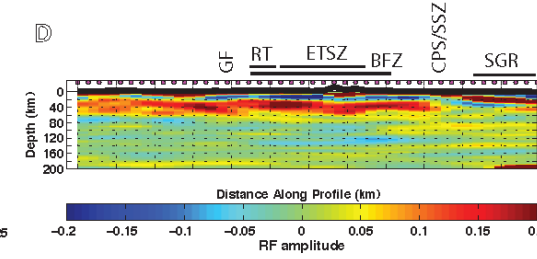
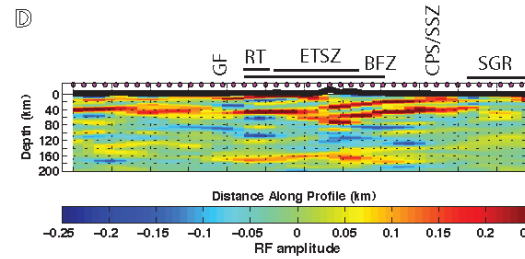
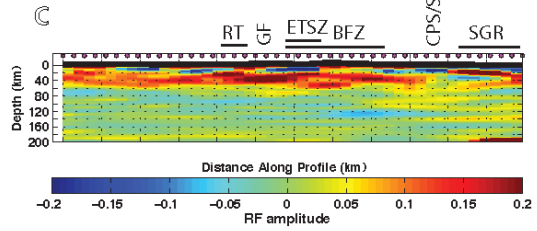
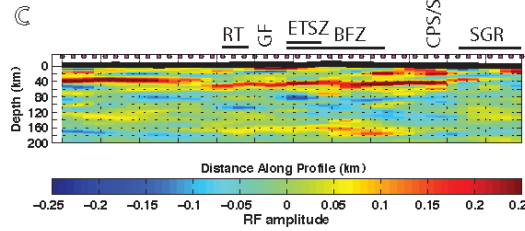
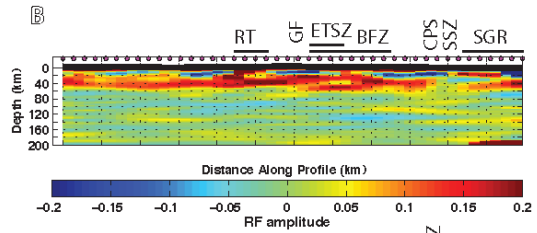
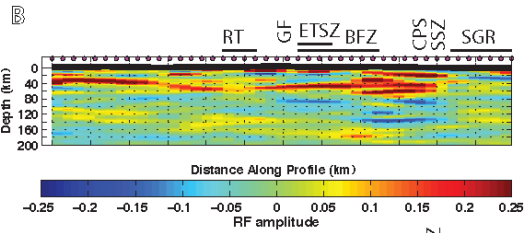
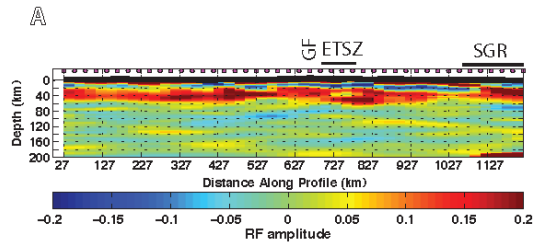
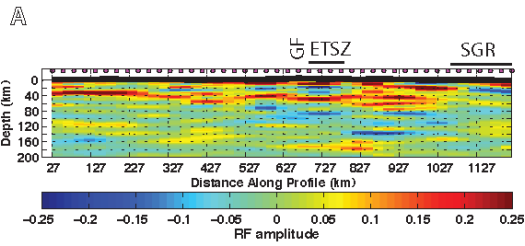
23

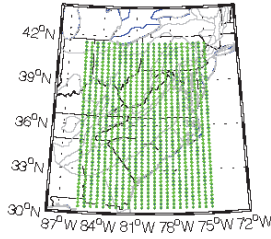




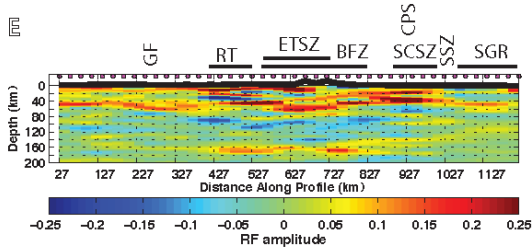
SR PRF CCP

SRF CCP

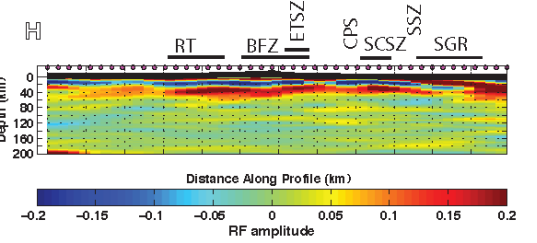
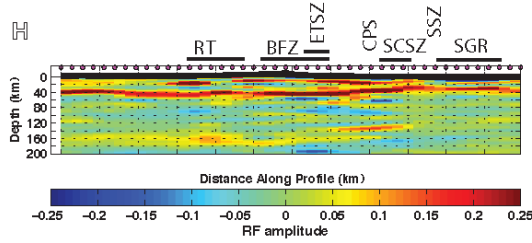
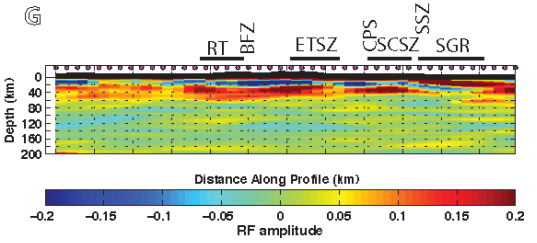
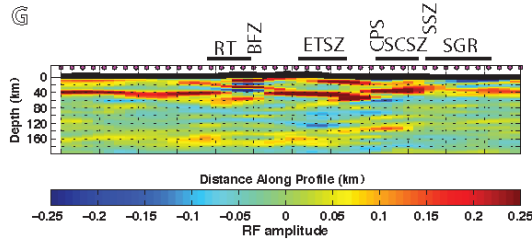
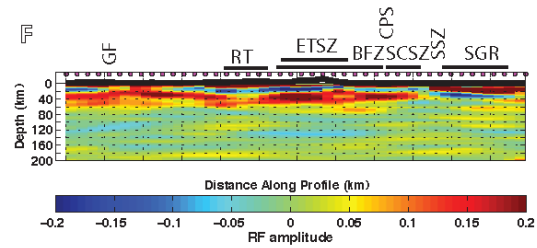
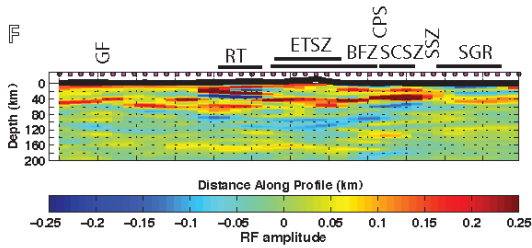
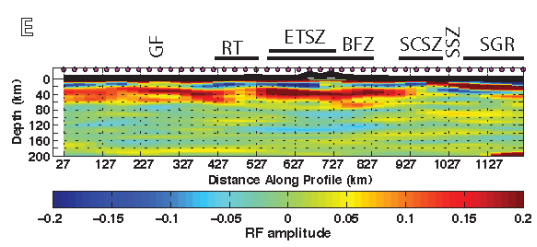


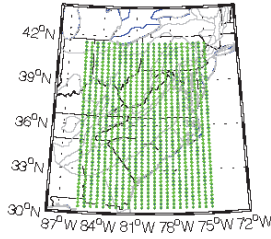


SR PRF CCP

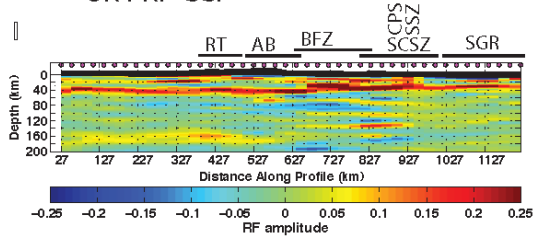


SRF CCP

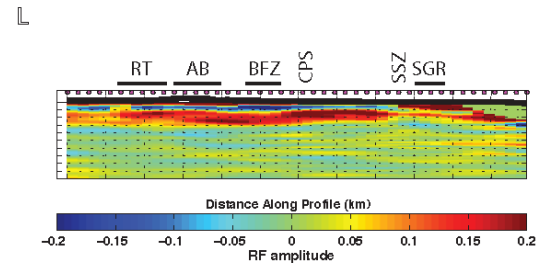
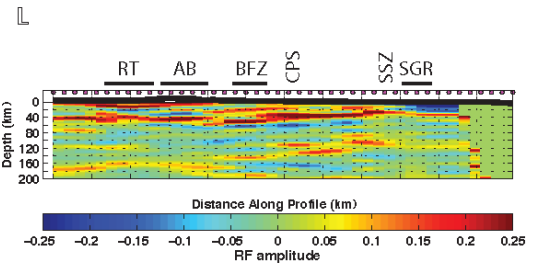
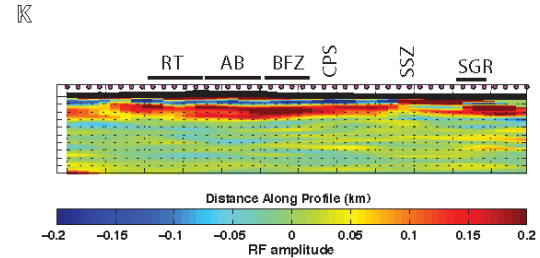
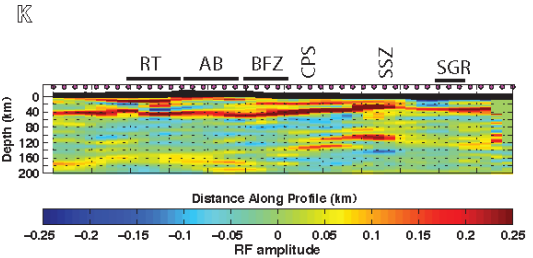
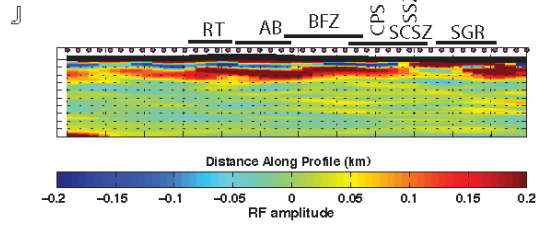
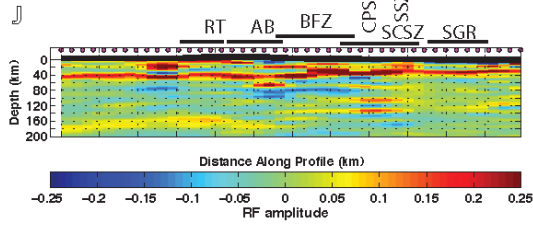
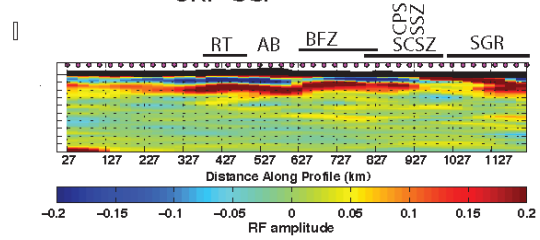


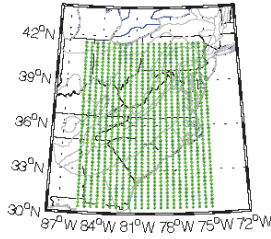


SR PRF CCP



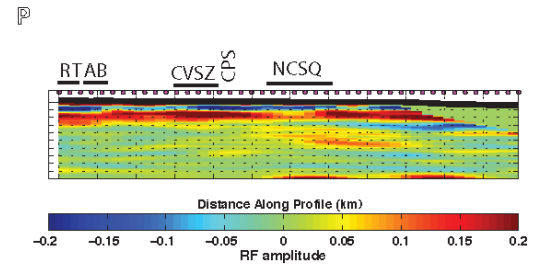
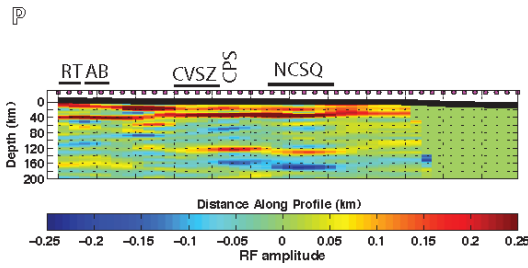
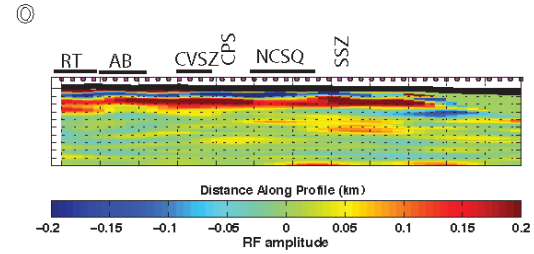
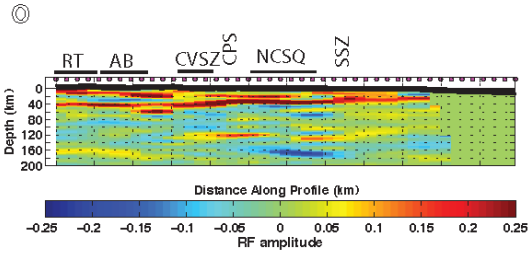
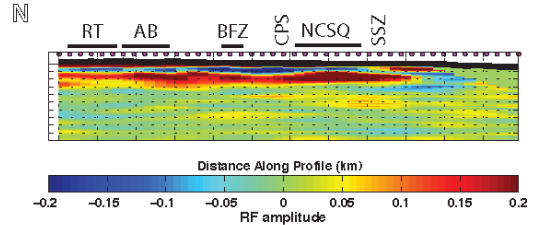
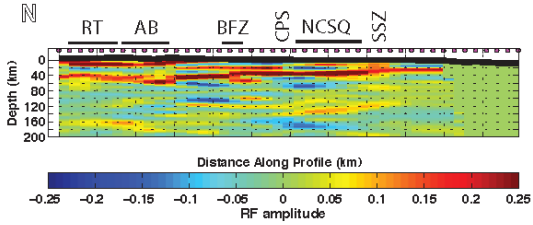
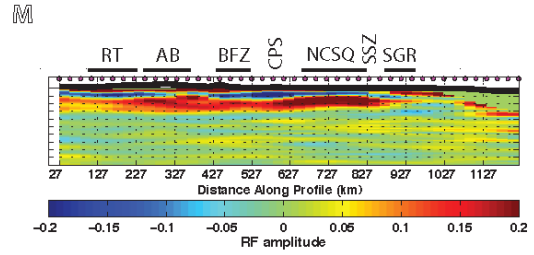
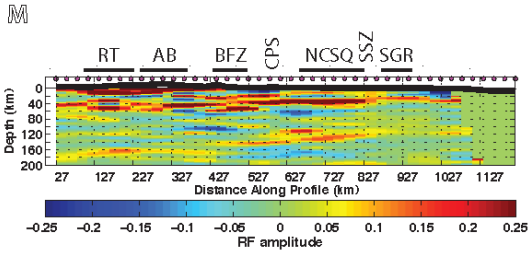
SRF CCP

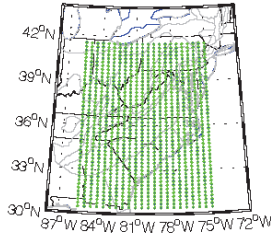




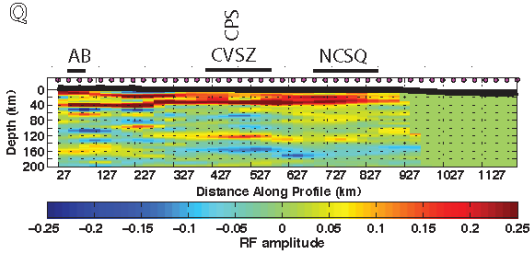
SR PRF CCP

SRF CCP

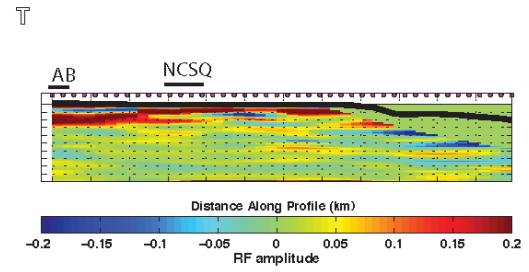
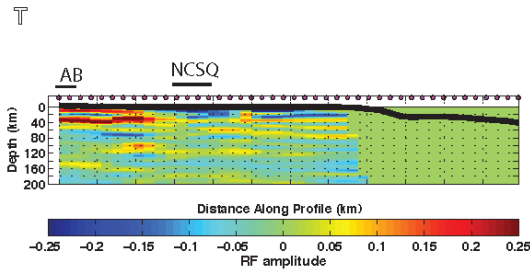
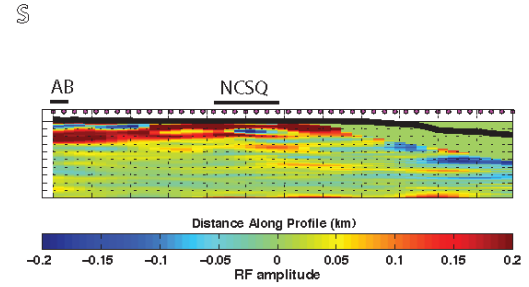
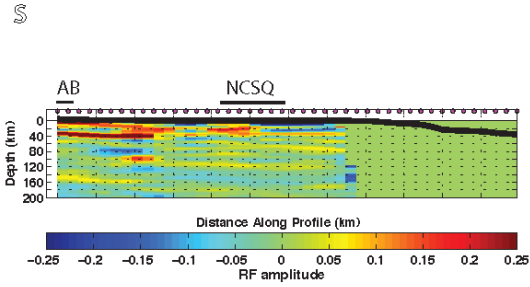
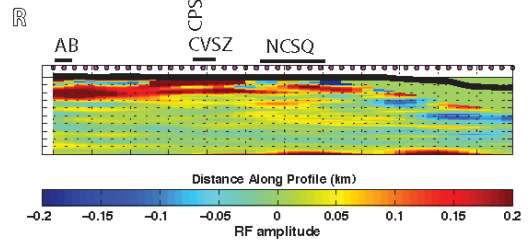
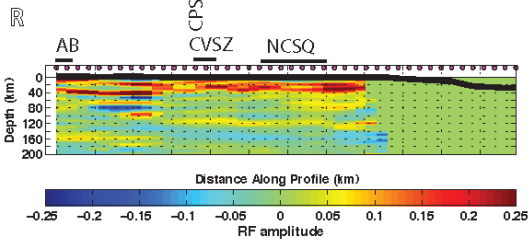
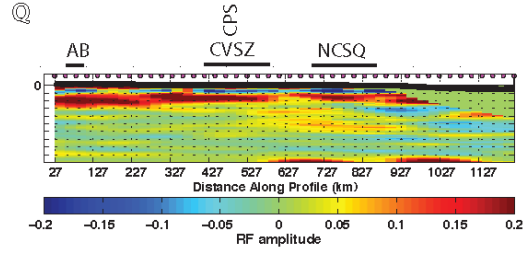


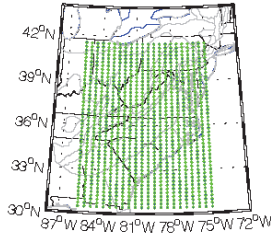


SR PRF CCP



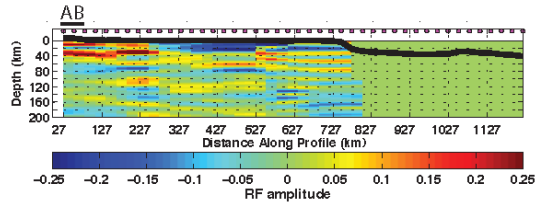
SRF CCP





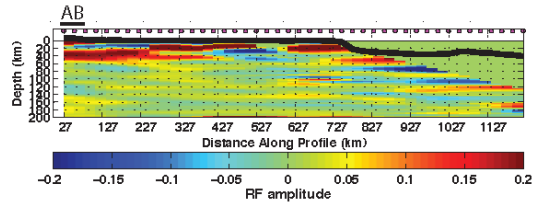
SR PRF CCP

U

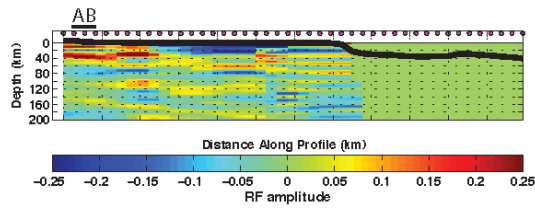


SRF CCP

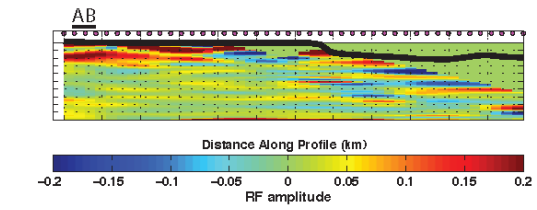
U



V



V



Bibliography

- Abrahamson, N., Silva, W., 2008. Summary of the Abrahamson & Silva NGA Ground-Motion Relations. *Earthq. Spectra* 24, 67–97.
<https://doi.org/10.1193/1.2924360>
- Aki, K., Richards, P.G., 1980. *Quantitative Seismology*, second ed. ed. University Science Books.
- Allmendinger, R.W., Serpa, L., Smith, R.B., n.d. Cenozoic and Mesozoic structure of the eastern Basin and Range province, Utah, from COCORP seismic-reflection data. [https://doi.org/10.1130/0091-7613\(1983\)11<532:CAMSOT>2.0.CO;2](https://doi.org/10.1130/0091-7613(1983)11<532:CAMSOT>2.0.CO;2)
- American Association of Petroleum Geologists, 1967. Basement map of North America between latitudes 24° and 60° N. Basement Rock Proj. Committee, U.S Geol. Surv. map67001271.
- Audet, P., Bostock, M.G., Christensen, N.I., Peacock, S.M., 2009. Seismic evidence for overpressured subducted oceanic crust and megathrust fault sealing. *Nature* 457, 76–78. <https://doi.org/10.1038/nature07650>
- B. Herrmann, R., 1979. Surface wave focal mechanisms for eastern North American earthquakes with tectonic implications. *J. Geophys. Res.* 84, 3543–3552.
<https://doi.org/10.1029/JB084iB07p03543>
- Baise, L.G., Kaklamanos, J., Berry, B.M., Thompson, E.M., 2016. Soil amplification with a strong impedance contrast: Boston, Massachusetts. *Eng. Geol.* 202, 1–13.
<https://doi.org/10.1016/J.ENGCEO.2015.12.016>
- Bassin, C., Laske, G., Mastern, G., 2000. The Current limits of Resolution for Surface Wave Tomography in North America, in: *EOS Trans AGU*.
- Biryol, C.B., Lee, S.J., Lees, J.M., Shore, M.J., 2018. Lithospheric structure of an incipient rift basin: Results from receiver function analysis of Bransfield Strait, NW Antarctic Peninsula. *Polar Sci.* 0–1.
<https://doi.org/10.1016/j.polar.2018.02.003>
- Biryol, C.B., Wagner, L.S., Fischer, K.M., Hawman, R.B., 2016. Relationship between observed upper mantle structures and recent tectonic activity across the Southeastern United States. *J. Geophys. Res. Solid Earth* 121, 3393–3414.
<https://doi.org/10.1002/2015JB012698>

- Bodin, P., Smith, K., Horton, S., Hwang, H., 2001. Microtremor observations of deep sediment resonance in metropolitan Memphis, Tennessee. *Eng. Geol.* 62, 159–168. [https://doi.org/10.1016/S0013-7952\(01\)00058-8](https://doi.org/10.1016/S0013-7952(01)00058-8)
- Borcherdt, R., 1970. Effects of Local Geology on Ground Motion Near San Francisco Bay. *Bull. Seismol. Soc. Am.* 60, 29–61. <https://doi.org/10.2307/1779766>
- Bostock, M.G., 1998. Mantle stratigraphy and evolution of the Slave province. *J. Geophys. Res.* 103, 21183. <https://doi.org/10.1029/98JB01069>
- Bostock, M.G., 1996. Ps conversions from the upper mantle transition zone beneath the Canadian landmass. *J. Geophys. Res. Earth* 101, 8393–8402.
- Bostock, M.G., Kumar, M.R., 2010. Bias in seismic estimates of crustal properties. *Geophys. J. Int.* 182, 403–407. <https://doi.org/10.1111/j.1365-246X.2010.04623.x>
- Bracewell, R., 1968. *The Fourier Transform and Its Applications*, 2nd editio. ed, Integers. McGraw-Hill, New York. <https://doi.org/10.1119/1.1973431>
- Brocher, T.M., 2005. Empirical relations between elastic wavespeeds and density in the Earth's crust. *Bull. Seismol. Soc. Am.* 95, 2081–2092. <https://doi.org/10.1785/0120050077>
- Chai, C., Ammon, C.J., Maceira, M., Herrmann, R.B., 2015. Inverting interpolated receiver functions with surface wave dispersion and gravity: Application to the western U.S. and adjacent Canada and Mexico. *Geophys. Res. Lett.* 42, 4359–4366. <https://doi.org/10.1002/2015GL063733>
- Chapman, C.H., 2003. Yet another elastic plane-wave, layer-matrix algorithm. *Geophys. J. Int.* 154, 212–223. <https://doi.org/10.1046/j.1365-246X.2003.01958.x>
- Chapman, D.M.F., Godin, O.A., 2001. Dispersion of interface waves in sediments with power-law shear speed profiles. II. Experimental observations and seismo-acoustic inversions. *J. Acoust. Soc. Am.* 110, 1908–1916. <https://doi.org/10.1121/1.1401739>
- Chen, K.-C., Chiu, J.-M., Yang, Y.-T., 1996. Shear-wave velocity of the sedimentary basin in the upper Mississippi embayment using S-to-P converted waves. *Bull. Seismol. Soc. Am.* 86, 848–856.
- Christensen, N.I., 1996. Poisson's ratio and crustal seismology. *J. Geophys. Res. Solid Earth* 101, 3139–3156. <https://doi.org/10.1029/95JB03446>

- Chulick, G.S., Mooney, W.D., 2002. Seismic structure of the crust and uppermost mantle of north America and adjacent oceanic basins: A synthesis. *Bull. Seismol. Soc. Am.* 92, 2478–2492. <https://doi.org/10.1785/0120010188>
- Clark, S.H.B., n.d. Location of the Southern Appalachians Birth of the Mountains
The Geologic Story of the Southern Appalachian Mountains.
- Clayton, R.W., Wiggins, R.A., 1976. Source shape estimation and devoncolution of teleseismic body waves. *Geophys. J. R. Astron. Soc.* 151–177.
<https://doi.org/https://doi.org/10.1111/j.1365-246X.1976.tb01267.x>
- Clowes, R.M., Brandon, M.T., Green, A.G., Yorath, C.J., Sutherland Brown, A., Kanasewich, E.R., Spencer, C., 1987. LITHOPROBE-southern Vancouver Island: Cainozoic subduction complex image by deep seismic reflections. *Can. J. Earth Sci.* 24, 31–51. <https://doi.org/10.1139/e87-004>
- COOK, F.A., 1988. Proterozoic thin-skinned thrust and fold belt beneath the Interior Platform in northwest Canada. *Geol. Soc. Am. Bull.* 100, 877–890.
[https://doi.org/10.1130/0016-7606\(1988\)100<0877:PTSTAF>2.3.CO;2](https://doi.org/10.1130/0016-7606(1988)100<0877:PTSTAF>2.3.CO;2)
- Cook, F.A., Brown, L.D., Kaufman, S., Oliver, J.E., Petersen, T.A., 1981. COCORP seismic profiling of the Appalachian orogen beneath the coastal plain of Georgia. *Geol. Soc. Am. Bull.* 92, 738–748. [https://doi.org/10.1130/0016-7606\(1981\)92<738:CSPOTA>2.0.CO;2](https://doi.org/10.1130/0016-7606(1981)92<738:CSPOTA>2.0.CO;2)
- Crotwell, H. Philip and Owens, T.J. (Department of G.S.U. of S.C., 2005. Automated Receiver Function Processing [WWW Document]. *Seismol. Res. Lett.*
<https://doi.org/10.17611/DP/EARS.1>
- Culotta, R.C., Pratt, T., Oliver, J., 1990. A tale of two sutures: COCORP’s deep seismic surveys of the Grenville province in the eastern U.S. midcontinent. *Geology* 18, 646. [https://doi.org/10.1130/0091-7613\(1990\)018<0646:ATOTSC>2.3.CO;2](https://doi.org/10.1130/0091-7613(1990)018<0646:ATOTSC>2.3.CO;2)
- Delgado, J., López Casado, C., Giner, J., Estévez, A., Cuenca, A., Molina, S., 2000. Microtremors as a Geophysical Exploration Tool: Applications and Limitations. *Pure Appl. Geophys.* 157, 1445–1462. <https://doi.org/10.1007/PL00001128>
- DiPietro, J.A., n.d. Geology and landscape evolution : general principles applied to the United States.
- Dreiling, J., Isken, M.P., Mooney, W.D., Park, M., Chapman, M.C., Godbee, R.W., 2014. PACIFIC EARTHQUAKE ENGINEERING NGA-East Regionalization Report : Comparison of Four Crustal Regions within Central and Eastern North America using Waveform Acceleration Response Virginia Polytechnic Institute and State University.

- Dueker, K.G., Sheehan, A.F., 1997. Mantle discontinuity structure from midpoint stacks of converted P to S waves across the Yellowstone hotspot track. *J. Geophys. Res. Solid Earth* 102, 8313–8327. <https://doi.org/10.1029/96JB03857>
- Earle, P.S., Shearer, P.M., 1994. Characterization of global seismograms using an automatic-picking algorithm. *Bull. Seismol. Soc. Am.* 84, 366–376.
- Eaton, D.W., Dineva, S., Mereu, R., 2006. Crustal thickness and VP/VS variations in the Grenville orogen (Ontario, Canada) from analysis of teleseismic receiver functions. *Tectonophysics* 420, 223–238. <https://doi.org/10.1016/j.tecto.2006.01.023>
- Fairbanks, C.D., Andrus, R.D., Camp, W.M., Wright, W.B., 2008. Dynamic Periods and Building Damage at Charleston, South Carolina During the 1886 Earthquake. *Earthq. Spectra* 24, 867–888. <https://doi.org/10.1193/1.2980346>
- Farra, V., Vinnik, L., 2000. Upper mantle stratification by P and S receiver functions. *Geophys. J. Int.* 141, 699–712. <https://doi.org/10.1046/j.1365-246x.2000.00118.x>
- Fenneman, N.M., Johnson, D.W., 1946. Physiographic divisions of the conterminous U.S.
- Fischer, K.M., Ford, H.A., Abt, D.L., Rychert, C.A., 2010. The Lithosphere-Asthenosphere Boundary. *Annu. Rev. Earth Planet. Sci.* 38, 551–575. <https://doi.org/10.1146/annurev-earth-040809-152438>
- Fischer, K.M., Salvati, L.A., Hough, S.E., Gonzalez, E., Nelsen, C.E., Roth, E.G., 2009. Bulletin of the Seismological Society of America . *J. Geol.* 21, 288–288. <https://doi.org/10.1086/622062>
- Flores, J., Novaro, O., Seligman, T.H., 1987. Possible resonance effect in the distribution of earthquake damage in Mexico City. *Nature* 326, 783–785. <https://doi.org/10.1038/326783a0>
- Frankel, A.D., Carver, D.L., Williams, R.A., 2002. Nonlinear and Linear Site Response and Basin Effects in Seattle for the M 6.8 Nisqually, Washington, Earthquake. *Bull. Seismol. Soc. Am.* 92, 2090–2109. <https://doi.org/10.1785/0120010254>
- Frassetto, A., Zandt, G., Gilbert, H., Owens, T.J., Jones, C.H., 2010. Improved imaging with phase-weighted common conversion point stacks of receiver functions. *Geophys. J. Int.* 182, no–no. <https://doi.org/10.1111/j.1365-246X.2010.04617.x>

- French, S.W., Fischer, K.M., Syracuse, E.M., Wysession, M.E., 2009. Crustal structure beneath the Florida-to-Edmonton broadband seismometer array. *Geophys. Res. Lett.* 36, L08309. <https://doi.org/10.1029/2008GL036331>
- Hansen, S., Dueker, K., n.d. P-and S-Wave Receiver Function Images of Crustal Imbrication beneath the Cheyenne Belt in Southeast Wyoming. <https://doi.org/10.1785/0120080168>
- Hatcher, R.D., 2010. The Appalachian orogen: A brief Summary. *Geol. Soc. Am. Memoir* 206. [https://doi.org/10.1130/2010.1206\(01\)](https://doi.org/10.1130/2010.1206(01))
- Hopper, E., Fischer, K.M., Wagner, L.S., Hawman, R.B., 2017. Reconstructing the end of the Appalachian orogeny. *Geology* 45, 15–18. <https://doi.org/10.1130/G38453.1>
- Joyner, W.B., Warrick, R.E., Fumal, T.E., 1981. The effect of quaternary alluvium on strong ground motion in the Coyote Lake, California, earthquake of 1979. *Bull. Seismol. Soc. Am.* 71, 1333–1349.
- Julià, J., Ammon, C.J., Herrmann, R.B., Correig, A.M., 2000. Joint inversion of receiver function and surface wave dispersion observations. *Geophys. J. Int.* 143, 99–112. <https://doi.org/10.1046/j.1365-246X.2000.00217.x>
- Kang, D., Yu, C., Ning, J., Chen, W., 2016. Simultaneous Determination of Crustal Thickness and P Wavespeed by Virtual Deep Seismic Sounding (VDSS). *Seismol. Res. Lett.* 87, 1104–1111. <https://doi.org/10.1785/0220160056>
- Kawakatsu, H., Kumar, P., Takei, Y., Shinohara, M., Kanazawa, T., Araki, E., Suyehiro, K., 2009. Seismic evidence for sharp lithosphere-asthenosphere boundaries of oceanic plates. *Science* 324, 499–502. <https://doi.org/10.1126/science.1169499>
- Kennett, B.L.N., 1991. The Removal of Free Surface Interactions From Three-Component Seismograms. *Geophys. J. Int.* 104, 153–154. <https://doi.org/10.1111/j.1365-246X.1991.tb02501.x>
- Kennett, B.L.N., Engdahl, E.R., Buland, R., 1995. Constraints on seismic velocities in the Earth from traveltimes. *Geophys. J. Int.* 122, 108–124. <https://doi.org/10.1111/j.1365-246X.1995.tb03540.x>
- KIKUCHI, M., KANAMORI, H., 1982. Inversion of complex body waves. *Bull. Seismol. Soc. Am.* 72, 491–506.
- Kolb, J.M., Leki, V., 2014. Receiver function deconvolution using transdimensional hierarchical Bayesian inference. *Geophys. J. Int.* 197, 1719–1735. <https://doi.org/10.1093/gji/ggu079>

- Koper, K.D., Burlacu, R., 2015. The fine structure of double-frequency microseisms recorded by seismometers in North America. *J. Geophys. Res. Solid Earth* 120, 1677–1691. <https://doi.org/10.1002/2014JB011820>
- Kumar, M.R., Bostock, M.G., 2008. Extraction of absolute P velocity from receiver functions. *Geophys. J. Int.* 175, 515–519. <https://doi.org/10.1111/j.1365-246X.2008.03963.x>
- Kumar, M.R., Saul, J., Sarkar, D., Kind, R., Shukla, A.K., 2001. Crustal structure of the Indian shield: New constraints from teleseismic receiver functions. *Geophys. Res. Lett.* 28, 1339–1342. <https://doi.org/10.1029/2000GL012310>
- Lachet, C., Hatzfeld, D., Bard, P.-Y., Theodulidis, N., Papaioannou, C., Savvaidis, A., 1996. Site Effects and Microzonation in the City of Thessaloniki (Greece) Comparison of Different Approaches, *Bulletin of the Seismological Society of America*.
- Langston, C.A., 1979. Structure under Mount Rainier, Washington, inferred from teleseismic body waves. *J. Geophys. Res.* 84, 4749. <https://doi.org/10.1029/JB084iB09p04749>
- Langston, C.A., Horton, S.P., 2014. Three-dimensional seismic-velocity model for the unconsolidated mississippi embayment sediments from H/V ambient noise measurements. *Bull. Seismol. Soc. Am.* 104, 2349–2358. <https://doi.org/10.1785/0120140026>
- Laske, G., Mastern, G., Ma, Z., Pasyanos, M., 2013. CRUST 1.0: An Updated Global Model of Earth's Crust.
- Lawrence, D.P., Hoffman, C.W., 1993. *Geology of Basement Rocks Beneath the North Carolina Coastal Plain*.
- Lawrence, J.F., Shearer, P.M., 2006. Constraining seismic velocity and density for the mantle transition zone with reflected and transmitted waveforms. *Geochemistry, Geophys. Geosystems* 7. <https://doi.org/10.1029/2006GC001339>
- Lawrence, J.F., Wiens, D.A., 2004. Combined receiver-function and surface wave phase-velocity inversion using a niching genetic algorithm: Application to Patagonia. *Bull. Seismol. Soc. Am.* 94, 977–987. <https://doi.org/10.1785/0120030172>
- Leahy, G.M., Saltzer, R.L., Schmedes, J., 2012. Imaging the shallow crust with teleseismic receiver functions. *Geophys. J. Int.* 191, 627–636. <https://doi.org/10.1111/j.1365-246X.2012.05615.x>

- Lekić, V., Fischer, K.M., 2017. Interpreting spatially stacked Sp receiver functions. *Geophys. J. Int.* 210, 874–886. <https://doi.org/10.1093/gji/ggx206>
- Lermo, J., Chavez-Garcia, F., 1994. Are Microtremors useful in site response evaluation? *Bull. Seismol. Soc. Am.* 84, 1350–1364.
- Levander, A., Miller, M.S., 2012. Evolutionary aspects of lithosphere discontinuity structure in the Western U.S. *Geochemistry, Geophys. Geosystems* 13, n/a–n/a. <https://doi.org/10.1029/2012GC004056>
- Levin, V., Park, J., 1997. *P-SH* conversions in a flat-layered medium with anisotropy of arbitrary orientation. *Geophys. J. Int.* 131, 253–266. <https://doi.org/10.1111/j.1365-246X.1997.tb01220.x>
- Li, A., 2002. Crust and upper mantle discontinuity structure beneath eastern North America. *J. Geophys. Res.* 107, 2100. <https://doi.org/10.1029/2001JB000190>
- Ligorria, J.P., Ammon, C.J., 1999. Iterative deconvolution and receiver-function estimation. *Bull. Seismol. Soc. Am.* 89, 1395–1400.
- Liu, G., Persaud, P., Clayton, R.W., n.d. Structure of the Northern Los Angeles Basins Revealed in Teleseismic Receiver Functions from Short-Term Nodal Seismic Arrays. <https://doi.org/10.1785/0220180071>
- Liu, H.-P., Hu, Y., Dorman, J., Chang, T.-S., Chiu, J.-M., 1997. Upper Mississippi embayment shallow seismic velocities measured in situ. *Eng. Geol.* 46, 313–330. [https://doi.org/10.1016/S0013-7952\(97\)00009-4](https://doi.org/10.1016/S0013-7952(97)00009-4)
- Liu, L., Gao, S.S., 2018. Lithospheric layering beneath the contiguous United States constrained by S-to-P receiver functions. *Earth Planet. Sci. Lett.* 495, 79–86. <https://doi.org/10.1016/J.EPSL.2018.05.012>
- Long, M.D., Benoit, M.H., Aragon, J.C., King, S.D., 2019. Seismic imaging of mid-crustal structure beneath central and eastern North America: Possibly the elusive Grenville deformation? *Geology* 47, 371–374. <https://doi.org/10.1130/G46077.1>
- Long, M.D., Ford, H.A., Abrahams, L., Wirth, E.A., 2017. The seismic signature of lithospheric deformation beneath eastern North America due to Grenville and Appalachian orogenesis. *Lithosphere* 9, 987–1001. <https://doi.org/10.1130/L660.1>
- Luzi, L., Puglia, R., Pacor, F., Gallipoli, M.R., Bindi, D., Mucciarelli, M., 2011. Proposal for a soil classification based on parameters alternative or complementary to V_s . *Bull. Earthq. Eng.* 9, 1877–1898. <https://doi.org/10.1007/s10518-011-9274-2>

- Lynner, C., Porritt, R.W., 2017. Crustal structure across the eastern North American margin from ambient noise tomography. *Geophys. Res. Lett.* 44, 6651–6657. <https://doi.org/10.1002/2017GL073500>
- Mendecki, M.J., Bieta, B., Mycka, M., 2014. Determination of the resonance frequency – thickness relation based on the ambient seismic noise records from Upper Silesia Coal Basin. *Contemp.Trends.Geosci* 3, 41–51. <https://doi.org/10.2478/ctg-2014-0011>
- Mooney, W.D., Andrews, M.C., Ginzburg, A., Peters, D.A., Hamilton, R.M., 1983. Crustal structure of the northern mississippi embayment and a comparison with other continental rift zones. *Dev. Geotecton.* 19, 327–348. <https://doi.org/10.1016/B978-0-444-42198-2.50025-0>
- Murphy, B.S., Egbert, G.D., 2017. Electrical conductivity structure of southeastern North America: Implications for lithospheric architecture and Appalachian topographic rejuvenation. *Earth Planet. Sci. Lett.* 462, 66–75. <https://doi.org/10.1016/J.EPSL.2017.01.009>
- Musacchio, G., Mooney, W.D., Luetgert, J.H., Christensen, N.I., 1997. Composition of the crust in the Grenville and Appalachian Provinces of North America inferred from V_p/V_s ratios. *J. Geophys. Res. Solid Earth* 102, 15225–15241. <https://doi.org/10.1029/96JB03737>
- Nakamura, Y., 2000. CLEAR IDENTIFICATION OF FUNDAMENTAL IDEA OF NAKAMURA'S TECHNIQUE AND ITS APPLICATIONS. 12WCEE.
- Nakamura, Y., 1989. A Method for Dynamic Characteristics Estimation of Subsurface using Microtremor on the Ground Surface. *Q. Rep. Railw. Tech. Res. Insitute* 30.
- Narayan, J.P., Kumar, R., n.d. Spatial spectral amplification of basin-transduced Rayleigh waves 3D Kinematic strong ground motion simulation View project Spatial spectral amplification of basin-transduced Rayleigh waves. <https://doi.org/10.1007/s11069-013-0917-2>
- Olugboji, T.M., Park, J., 2016. Crustal anisotropy beneath Pacific Ocean-Islands from harmonic decomposition of receiver functions. *Geochemistry, Geophys. Geosystems* 17, 810–832. <https://doi.org/10.1002/2015GC006166>
- Owens, T.J., Zandt, G., 1997. Implications of crustal property variations for models of Tibetan plateau evolution. *Nature* 387, 37–43. <https://doi.org/10.1038/387037a0>
- Owens, T.J., Zandt, G., Taylor, S.R., 1984. Seismic evidence for an ancient rift beneath the Cumberland Plateau, Tennessee: A detailed analysis of broadband

- teleseismic P waveforms. *J. Geophys. Res.* 89, 7783–7795.
<https://doi.org/https://doi.org/10.1029/JB089iB09p07783>
- Parker, E.H., Hawman, R.B., Fischer, K.M., Wagner, L.S., 2016. Estimating crustal thickness using SsPmp in regions covered by low-velocity sediments: Imaging the Moho beneath the Southeastern Suture of the Appalachian Margin Experiment (SESAME) array, SE Atlantic Coastal Plain. *Geophys. Res. Lett.* 43, 9627–9635. <https://doi.org/10.1002/2016GL070103>
- Parker, E.H., Hawman, R.B., Fischer, K.M., Wagner, L.S., 2013. Crustal evolution across the southern Appalachians: Initial results from the SESAME broadband array. *Geophys. Res. Lett.* 40, 3853–3857. <https://doi.org/10.1002/grl.50761>
- Parolai, S., Picozzi, M., Richwalski, S.M., Milkereit, C., 2005. Joint inversion of phase velocity dispersion and H/V ratio curves from seismic noise recordings using a genetic algorithm, considering higher modes.
<https://doi.org/10.1029/2004GL021115>
- Perron, V., Gélis, C., Froment, B., Hollender, F., Bard, P.-Y., Cultrera, G., Cushing, E.M., 2018. Can broad-band earthquake site responses be predicted by the ambient noise spectral ratio? Insight from observations at two sedimentary basins. *Geophys. J. Int.* 215, 1442–1454. <https://doi.org/10.1093/gji/ggy355>
- Pesce, K.A., 2010. Comparison of Receiver Function Deconvolution Techniques. Massachusetts Institute of Technology.
- Petersen, T.A., Brown, L.D., Cook, F.A., Kaufman, S., Oliver, J.E., 1984. Structure of the Riddleville Basin from COCORP Seismic Data and Implications for Reactivation Tectonics. *J. Geol.* 92, 261–271. <https://doi.org/10.1086/628859>
- Pitilakis, K., Riga, E., Anastasiadis, A., 2013. New code site classification, amplification factors and normalized response spectra based on a worldwide ground-motion database. *Bull. Earthq. Eng.* 11, 925–966.
<https://doi.org/10.1007/s10518-013-9429-4>
- Pratt, T.-L., Brocher, T.-M., Weaver, C.-S., Miller, K.-C., Trhu, A.-M., Creager, K.-C., Crosson, R.-S., Snelson, C.-M., 2003. Amplification of seismic waves by the Seattle basin, northwestern U.S. *Bull. Seism. Soc. Am.* 93, 533–545.
- Pratt, T.L., 2018. Characterizing and Imaging Sedimentary Strata Using Depth-Converted Spectral Ratios: An Example from the Atlantic Coastal Plain of the Eastern United States. *Bull. Seismol. Soc. Am.* 108, 2801–2815.
<https://doi.org/10.1785/0120180046>
- Pratt, T.L., Wright Horton Jr, J., Muñoz, J., Hough, S.E., Chapman, M.C., Guney Olgun, C., n.d. Amplification of Earthquake Ground Motions in Washington,

- DC, and Implications for Hazard Assessments in Central and Eastern North America. <https://doi.org/10.1002/2017GL075517>
- Ramesh, D.S., Kind, R., Yuan, X., 2002. Receiver function analysis of the North American crust and upper mantle. *Geophys. J. Int.* 150, 91–108. <https://doi.org/10.1046/j.1365-246X.2002.01697.x>
- Reeves, Z., Lekić, V., Schmerr, N., Kohler, M., Weeraratne, D., 2015. Lithospheric structure across the California Continental Borderland from receiver functions. *Geochemistry, Geophys. Geosystems* 16, 246–266. <https://doi.org/10.1002/2014GC005617>
- Rivers, T., 2014. Tectonic Setting and Evolution of the Grenville Orogen: An Assessment of Progress over the last 40 years. *Geosci. Canada* 42, 77–124.
- Ross, Gerald, M., Milkereit, B., Eaton, D., White, D., Kanasewich, E.R., Burianyk, M., n.d. Paleoproterozoic collisional orogen beneath the Western Canada Sedimentary Basin imaged by Lithoprobe crustal seismic-reflection data Electrical conduction View project Simulating hydraulic fracturing using Finite-Discrete Element Methods FDEM View projec. [https://doi.org/10.1130/0091-7613\(1995\)023<0195:PCOBTW>2.3.CO;2](https://doi.org/10.1130/0091-7613(1995)023<0195:PCOBTW>2.3.CO;2)
- Rychert, C.A., Harmon, N., 2016. Stacked P-to-S and S-to-P receiver functions determination of crustal thickness, V_p , and V_s : The H-V stacking method. *Geophys. Res. Lett.* 43, 1487–1494. <https://doi.org/10.1002/2015GL067010>
- Rychert, C.A., Rondenay, S., Fischer, K.M., 2007. P-to-S and S-to-P imaging of a sharp lithosphere-asthenosphere boundary beneath eastern North America. *J. Geophys. Res. Solid Earth* 112, 1–21. <https://doi.org/10.1029/2006JB004619>
- Schimmel, M., Paulssen, H., 1997. Noise reduction and detection of weak, coherent signals through phase-weighted stacks. *Geophys. J. Int.* 130, 497–505. <https://doi.org/10.1111/j.1365-246X.1997.tb05664.x>
- Schulte-Pelkum, V., Mahan, K.H., Shen, W., Stachnik, J.C., 2017. The distribution and composition of high-velocity lower crust across the continental U.S.: Comparison of seismic and xenolith data and implications for lithospheric dynamics and history. *Tectonics* 36, 1455–1496. <https://doi.org/10.1002/2017TC004480>
- Schulte-Pelkum, V., Monsalve, G., Sheehan, A., Pandey, M.R., Sapkota, S., Bilham, R., Wu, F., 2005. Imaging the Indian subcontinent beneath the Himalaya. *Nature* 435, 1222–1225. <https://doi.org/10.1038/nature03678>

- Seismological Society of America., C.A., 1911. Bulletin of the Seismological Society of America., Bulletin of the Seismological Society of America. Seismological Society of America.
- Seismological Society of America., E.H., Hough, S.E., Jacob, K.H., 1911. Bulletin of the Seismological Society of America., Bulletin of the Seismological Society of America. Seismological Society of America.
- Shearer, P.M., 2009. Introduction to Seismology, 2nd edition. ed. Cambridge University Press, Cambridge.
- Shearer, P.M., Orcutt, J.A., 1987. Surface and near-surface effects on seismic waves—theory and borehole seismometer results. *Bull. Seismol. Soc. Am.* 77, 1168–1196.
- Sheehan, A.F., Abers, G.A., Jones, C.H., Lerner-Lam, A.L., 1995. Crustal thickness variations across the Colorado Rocky Mountains from teleseismic receiver functions. *J. Geophys. Res.* 100, 20391. <https://doi.org/10.1029/95JB01966>
- Sheehan, A.F., Dueker, K., Gilbert, H.J., Sheehan, A.F., Dueker, K.G., Molnar, P., Gilbert, H.J., Dueker, K.G., Molnar, P., 2003. Receiver functions in the western United States, with implications for upper mantle structure and dynamics Tsunami Data Assimilation Without a Dense Observation Network View project Integrated Geological and Geophysical Studies of the Western U.S. and adjacent Mexico and Canada View project Receiver functions in the western United States, with implications for upper mantle structure and dynamics. *Artic. J. Geophys. Res. Atmos.* 108, 2229. <https://doi.org/10.1029/2001JB001194>
- Shen, W., Ritzwoller, M.H., Schulte-Pelkum, V., 2013. A 3-D model of the crust and uppermost mantle beneath the Central and Western US by joint inversion of receiver functions and surface wave dispersion. *J. Geophys. Res. Solid Earth* 118, 262–276. <https://doi.org/10.1029/2012JB009602>
- Soto-Cordero, L., Meltzer, A., Stachnik, J.C., 2018. Crustal Structure, Intraplate Seismicity, and Seismic Hazard in the Mid-Atlantic United States. *Seismol. Res. Lett.* 89, 241–252. <https://doi.org/10.1785/0220170084>
- Stein, C.A., Stein, S., Elling, R., Keller, G.R., Kley, J., 2018. Is the “Grenville Front” in the central United States really the Midcontinent Rift? *GSA Today* 4–10. <https://doi.org/10.1130/GSATG357A.1>
- Stephenson, W.J., Asten, M.W., Odum, J.K., Frankel, A.D., 2019. Shear-Wave Velocity in the Seattle Basin to 2 km Depth Characterized with the krSPAC Microtremor Array Method: Insights for Urban Basin-Scale Imaging. *Seismol. Res. Lett.* <https://doi.org/10.1785/0220180194>

- Thybo, H., Perchucé, E., Zhou, S., 2000. Intraplate earthquakes and a seismically defined lateral transition in the upper mantle. *Geophys. Res. Lett.* 27, 3953–3956. <https://doi.org/10.1029/2000GL011636>
- Tian, X., Chen, Y., Tseng, T.L., Klemperer, S.L., Thybo, H., Liu, Z., Xu, T., Liang, X., Bai, Z., Zhang, X., Si, S., Sun, C., Lan, H., Wang, E., Teng, J., 2015. Weakly coupled lithospheric extension in southern Tibet. *Earth Planet. Sci. Lett.* 430, 171–177. <https://doi.org/10.1016/j.epsl.2015.08.025>
- Tsai, V.C., 2009. On establishing the accuracy of noise tomography travel-time measurements in a realistic medium. *Geophys. J. Int.* 178, 1555–1564. <https://doi.org/10.1111/j.1365-246X.2009.04239.x>
- Tsai, V.C., Atiganyanun, S., 2014. Green's functions for surface waves in a generic velocity structure. *Bull. Seismol. Soc. Am.* 104, 2573–2578. <https://doi.org/10.1785/0120140121>
- van Der Baan, M., 2009. The origin of SH-wave resonance frequencies in sedimentary layers, in: *Geophysical Journal International*. Wiley/Blackwell (10.1111), pp. 1587–1596. <https://doi.org/10.1111/j.1365-246X.2009.04245.x>
- Vinnik, L.P., 1977. Detection of waves converted from P to SV in the mantle. *Phys. Earth Planet. Inter.* 15, 39–45. [https://doi.org/10.1016/0031-9201\(77\)90008-5](https://doi.org/10.1016/0031-9201(77)90008-5)
- Wagner, L.S., Fischer, K.M., Hawman, R., Hopper, E., Howell, D., 2018. The relative roles of inheritance and long-term passive margin lithospheric evolution on the modern structure and tectonic activity in the southeastern United States. *Geosphere* 14, 1385–1410. <https://doi.org/10.1130/GES01593.1>
- Wagner, L.S., Stewart, K., Metcalf, K., 2012. Crustal-scale shortening structures beneath the Blue Ridge Mountains, North Carolina, USA. *Lithosphere* 4, 242–256. <https://doi.org/10.1130/L184.1>
- Ward, K.M., Lin, F.-C., n.d. On the Viability of Using Autonomous Three-Component Nodal Geophones to Calculate Teleseismic Ps Receiver Functions with an Application to Old Faithful, Yellowstone. <https://doi.org/10.1785/0220170051>
- Warren, D.H., Healy, J.H., Jackson, W.H., 1966. Crustal seismic measurements in southern Mississippi. *J. Geophys. Res.* 71, 3437–3458. <https://doi.org/10.1029/JZ071i014p03437>
- Wells, D., Egan, J.A., Murphy, D.G., Paret, T., 2015. Ground shaking and structural response of the Washington Monument during the 2011 Mineral, Virginia, earthquake. pp. 199–233. [https://doi.org/10.1130/2015.2509\(12\)](https://doi.org/10.1130/2015.2509(12))

- White, D.J., Lucas, S.B., Hajnal, Z., Green, A.G., Lewry, J.F., Weber, W., Bailes, A.H., Syme, E.C., Ashton, K., n.d. Paleo-Proterozoic thick-skinned tectonics: Lithoprobe seismic reflection results from the eastern Trans-Hudson Orogen.
- Wiener, N., 1964. Extrapolation, interpolation, and smoothing of stationary time series with engineering applications. Technology Press of the Massachusetts Institute of Technology.
- Wilson, D.C., Angus, D.A., Ni, J.F., Grand, S.P., 2006. Constraints on the interpretation of S-to- P receiver functions. *Geophys. J. Int.* 165, 969–980. <https://doi.org/10.1111/j.1365-246X.2006.02981.x>
- Wölbern, I., Rümpker, G., 2017. Limitations of H- κ stacking: ambiguous results caused by crustal layering. *J. Seismol.* 21, 221–235. <https://doi.org/10.1007/s10950-016-9599-z>
- Yantis, B.R., Costain, J.K., Ackerman, H.D., 1983. A reflection seismic study near Charleston, South Carolina. U.S. Geol. Surv. Professional Pap. 1313-G.
- Yao, H., Campman, X., de Hoop, M. V., van der Hilst, R.D., 2009. Estimation of surface wave Green's functions from correlation of direct waves, coda waves, and ambient noise in SE Tibet. *Phys. Earth Planet. Inter.* 177, 1–11. <https://doi.org/10.1016/J.PEPI.2009.07.002>
- Yassminh, R., Gallegos, A., Sandvol, E., Ni, J., 2019. Investigation of the Regional Site Response in the Central and Eastern United States. *Bull. Seismol. Soc. Am.* <https://doi.org/10.1785/0120180230>
- Yeck, W.L., Sheehan, A.F., Schulte-Pelkum, V., 2013. Sequential H- Stacking to Obtain Accurate Crustal Thicknesses beneath Sedimentary Basins. *Bull. Seismol. Soc. Am.* 103, 2142–2150. <https://doi.org/10.1785/0120120290>
- Yilar, E., Baise, L.G., Ebel, J.E., 2017. Using H/V measurements to determine depth to bedrock and Vs30 in Boston, Massachusetts. *Eng. Geol.* 217, 12–22. <https://doi.org/10.1016/J.ENGCEO.2016.12.002>
- Yu, C.-Q., Chen, W.-P., van der Hilst, R.D., 2013. Removing source-side scattering for virtual deep seismic sounding (VDSS). *Geophys. J. Int.* 195, 1932–1941. <https://doi.org/10.1093/gji/ggt359>
- Yu, C.Q., Chen, W.P., Ning, J.Y., Tao, K., Tseng, T.L., Fang, X.D., John Chen, Y., van der Hilst, R.D., 2012. Thick crust beneath the Ordos plateau: Implications for instability of the North China craton. *Earth Planet. Sci. Lett.* 357-358, 366–375. <https://doi.org/10.1016/j.epsl.2012.09.027>

- Yu, Y., Song, J., Liu, K.H., Gao, S.S., 2015. Determining crustal structure beneath seismic stations overlying a low-velocity sedimentary layer using receiver functions. *J. Geophys. Res. Solid Earth* 120, 3208–3218. <https://doi.org/10.1002/2014JB011610>
- Yuan, H., Dueker, K., Stachnik, J., 2010. Crustal structure and thickness along the Yellowstone hot spot track: Evidence for lower crustal outflow from beneath the eastern Snake River Plain. *Geochemistry, Geophys. Geosystems* 11, 1–14. <https://doi.org/10.1029/2009GC002787>
- Zandt, G., Gilbert, H., Owens, T.J., Ducea, M., Saleeby, J., Jones, C.H., 2004. Active foundering of a continental arc root beneath the southern Sierra Nevada in California. *Nature* 431, 41–46. <https://doi.org/10.1038/nature02847>
- Zelt, B.C., Ellis, R.M., 1999. Receiver-function studies in the Trans-Hudson Orogen, Saskatchewan. *Can. J. Earth Sci.* 603, 585–603. <https://doi.org/https://doi.org/10.1139/e98-109>
- Zhao, J.X., Xu, H., 2013. A Comparison of VS 30 and Site Period as Site-Effect Parameters in Response Spectral Ground-Motion Prediction Equations. *Bull. Seismol. Soc. Am.* 103, 1–18. <https://doi.org/10.1785/0120110251>
- Zhu, L., Kanamori, H., 2000. Moho depth variation in southern California from teleseismic receiver functions. *J. Geophys. Res.* 105, 2969–2980. <https://doi.org/10.1029/1999JB900322>